

**An investigation of surface energy balance and turbulent heat
flux on mountain glaciers**

by

Noel Fitzpatrick

B.Sc., Earth Sciences, The National University of Ireland Galway, 2006

M.Sc., Applied Meteorology, The University of Reading, 2007

A THESIS SUBMITTED IN PARTIAL FULFILLMENT OF
THE REQUIREMENTS FOR THE DEGREE OF

Doctor of Philosophy

in

THE FACULTY OF GRADUATE AND POSTDOCTORAL STUDIES
(Atmospheric Science)

THE UNIVERSITY OF BRITISH COLUMBIA

(Vancouver)

December 2018

© Noel Fitzpatrick, 2018

The following individuals certify that they have read, and recommend to the Faculty of Graduate and Postdoctoral Studies for acceptance, the dissertation entitled:

An investigation of surface energy balance and turbulent heat flux on mountain glaciers

submitted by Noel Fitzpatrick in partial fulfillment of the requirements for

the degree of Doctor of Philosophy

in Atmospheric Science

Examining Committee:

Assistant Professor Valentina Radić
Supervisor

Professor Gwenn Flowers
Supervisory Committee Member

Doctor Rosie Howard
Supervisory Committee Member

Professor Roland Stull
University Examiner

Professor Dan Moore
University Examiner

Additional Supervisory Committee Members:

Professor Andreas Christen
Supervisory Committee Member

Supervisory Committee Member

Abstract

The exchange of energy between a glacier surface and its surroundings, known as its surface energy balance (SEB), is a primary control on surface ablation rates. In the modelling of glacier SEB, parameterisation rather than direct measurement is frequently used to estimate one or more of the contributing heat fluxes, with smaller fluxes often deemed negligible. The turbulent fluxes of sensible and latent heat are commonly parameterised using forms of the bulk aerodynamic method. These techniques were developed for flat, uniform surfaces, and substantial uncertainty remains in the validity of their application over sloped, inhomogeneous glacier terrain. A multi-year field campaign was performed on two glaciers in the Purcell Mountains of British Columbia, Canada, where season-long observations of the complete SEB were obtained at multiple locations. The obtained dataset was used to drive an ablation model which showed good agreement with observed rates at seasonal, daily, and sub-daily timescales, effectively closing the energy balance. Through eddy covariance measurements, the turbulent heat fluxes were observed to be important components of SEB at each location, providing 31% of seasonal melt energy, and up to 78% of melt energy on individual days, underlining the need for their accurate estimation. The rain heat flux, often assumed negligible, was a significant contributor to melt energy on daily and sub-daily timescales during heavy rainfall (up to 20% day⁻¹). An evaluation of common turbulent flux parameterisation methods found their performance to be highly sensitive to the choice of roughness length scheme and atmospheric stability function. Observed roughness length values differed from those commonly assumed for glacier surfaces, and varied substantially between locations,

highlighting the need for site-specific values. Two techniques were developed for the remote estimation of roughness using digital elevation models, and performed well when compared with *in situ* observations. The occurrence of shallow, katabatic surface layers with low-level wind maximums was frequently observed over the sloped, glacial test sites. Existing stability parameters and functions used in turbulent flux parameterisation were found to be unreliable in these conditions, as was the commonly employed assumption of constant turbulent flux and friction velocity with height through this layer.

Lay Summary

In a warming climate, the ongoing retreat of mountain glaciers contributes to sea level rise, and affects the supply of fresh water to communities and ecosystems downstream. This study examines the exchange of heat between the atmosphere and a glacier surface, known as the surface energy balance, and how this balance affects melt rates. Monitoring stations were installed on two glaciers in British Columbia over the course of three summer seasons, to simultaneously observe the weather conditions and the rate of surface melt. Turbulent heat flux, a poorly understood and rarely measured energy source on glaciers, was found to be an important driver of melt. Methods have been developed in this study to improve the accuracy of turbulent flux observation and estimation on glaciers, which will increase our understanding of current glacier melt, and assist in the prediction of their future response.

Preface

This thesis is the original work of Noel Fitzpatrick, and presents research completed with the guidance of the supervisory committee, and with the assistance of collaborators and co-authors. The role and contribution of each party to the work in each chapter is outlined below.

Chapter 2 presents the analysis of observations from a meteorological and glaciological monitoring station installed on Nordic Glacier, British Columbia, Canada, during the summer of 2014. Noel Fitzpatrick conducted the system preparation and calibration, fieldwork, model development, and data analysis for the study, and wrote the chapter. Valentina Radić proposed the original experiment, provided financial and field support, and supervised the analysis and writing presented in the chapter. Brian Menounos provided logistical and minor financial support, and provided editorial suggestions on the text. A version of this chapter has been published in the following paper:

Fitzpatrick, N., Radić, V., and Menounos, B. (2017). Surface energy balance closure and turbulent flux parameterization on a mid-latitude mountain glacier, Purcell Mountains, Canada. *Front. Earth Sci.* 5:67. doi: 10.3389/feart.2017.00067

Chapter 3 presents the analysis of a dataset obtained from a multi-year glacier field campaign, and a series of LiDAR imaging flights, in the Purcell Mountains, British Columbia, Canada, from 2014 to 2016. Noel Fitzpatrick prepared and executed the on-glacier fieldwork and observations,

conducted the data analysis, and proposed the roughness estimation methods presented in the chapter, as well as writing the text. Valentina Radić helped develop these methods and the associated sensitivity testing, supervised the analysis, and provided financial and field support. Brian Menounos instigated the LiDAR imaging flights, and provided the resulting, processed digital elevation models to the study, in addition to logistical and minor financial support to the field campaign. At the time of writing, a paper based on this chapter had been submitted to *The Cryosphere*, and was under review:

Fitzpatrick, N., Radic, V., and Menounos, B. (2018). A multi-season investigation of glacier surface roughness lengths through in situ and remote observation. *The Cryosphere Discuss.* doi: 10.5194/tc-2018-232, in review.

Chapter 4 utilises the dataset from the on-glacier field campaign mentioned above. In addition to the previously detailed field duties, Noel Fitzpatrick performed the analysis on the surface energy balance and turbulence data from the campaign, and wrote the text. Valentina Radić supervised the analysis and writing presented in the chapter, and with Brian Menounos, provided financial and logistical support. This chapter is in preparation for a planned submission for publication.

Table of Contents

Abstract.....	iii
Lay Summary	v
Preface.....	vi
Table of Contents	viii
List of Tables	xiii
List of Figures.....	xiv
Acknowledgements	xvii
Dedication	xix
Chapter 1: Introduction and Motivation.....	1
1.1 Mountain Glaciers in a Warming Climate	1
1.2 Phase Change of Ice.....	2
1.3 Glacier Surface Energy Balance	3
1.4 Radiation Fluxes	5
1.5 Ground and Rain Heat Fluxes.....	5
1.6 Turbulent Heat Fluxes.....	6
1.6.1 Turbulent Flux Parameterisation.....	8
1.6.2 Roughness Lengths	10
1.6.3 Stability Corrections	11
1.7 Research Aim and Questions	12
1.8 Thesis Outline and Key Elements.....	14

Chapter 2: Surface energy balance closure and turbulent flux parameterisation on a mid-latitude mountain glacier, Purcell Mountains, Canada	17
2.1 Summary	17
2.2 Introduction.....	18
2.3 SEB Background.....	21
2.4 Data and Methods	23
2.4.1 Station Design.....	23
2.4.2 Field Campaign.....	26
2.4.3 AWS Data Treatment.....	27
2.4.4 SEB Model.....	36
2.4.5 Bulk Method Evaluation	38
2.5 Results.....	42
2.5.1 Meteorological and Flux Observations.....	42
2.5.2 Ablation Modelling and Surface Energy Balance Partitioning.....	45
2.5.3 Roughness Length Values.....	47
2.5.4 Bulk Method Evaluation	49
2.6 Discussion.....	49
2.6.1 Energy Balance Observation and Closure	49
2.6.2 Bulk Method Evaluation.....	53
2.6.3 Effect of Parameterisation on SEB Closure.....	58
2.7 Conclusions.....	60

Chapter 3: A multi-season investigation of glacier surface roughness lengths through in situ and remote observation.....63

3.1	Summary.....	63
3.2	Introduction.....	64
3.3	Data and methods.....	68
3.3.1	Field Campaign.....	68
3.3.2	AWS.....	69
3.3.3	LiDAR.....	71
3.3.4	Data Treatment.....	72
3.3.5	In Situ Roughness Length Values.....	73
3.3.6	Remote Momentum Roughness Length Estimation	75
3.4	Results.....	85
3.4.1	EC-Derived Roughness Lengths.....	85
3.4.2	Momentum Roughness Length from LiDAR	88
3.4.3	Wind Direction and Momentum Roughness Length	95
3.5	Discussion.....	97
3.5.1	Spatial and Temporal Variability of z_{0v}	97
3.5.2	Performance of DEM-based z_{0v} Estimation.....	101
3.5.3	Scalar Roughness Relationships	105
3.6	Conclusions.....	106

Chapter 4: Constraining the role of turbulent heat flux in glacier surface energy balance and its parameterisation for katabatic surface layers	109
4.1 Summary	109
4.2 Introduction.....	110
4.3 Data and Methods	113
4.3.1 Field Campaign.....	113
4.3.2 AWS.....	114
4.3.3 Data Treatment and SEB Analysis	116
4.3.4 Katabatic flow and LLWM Detection	118
4.3.5 Turbulent Flux Parameterisation.....	119
4.3.6 Katabatic Influence on Friction Velocity and Bulk Parameterisation	121
4.4 Results.....	123
4.4.1 Turbulent Flux Importance and Variability	123
4.4.2 Glacier Winds and Friction Velocity	127
4.4.3 Parameterisation Performance	132
4.5 Discussion.....	137
4.5.1 Turbulent Flux Variability	137
4.5.2 Slope and Katabatic flow	139
4.5.3 Bulk Performance and Wind Shear.....	140
4.6 Conclusions.....	144
Chapter 5: Conclusions and outlook.....	146
5.1 Summary of Findings.....	146
5.1.1 SEB Observation and Ablation Modelling.....	146

5.1.2	Importance of Turbulent Heat Flux and its Parameterisation for Glaciers.	147
5.1.3	Roughness Length Variability and Estimation	148
5.1.4	The Role of Stability and Slope	149
5.2	Key Contributions and Future Directions	150
References	153
Appendix A	173
Appendix B	175

List of Tables

Table 2.1. Instrumentation used on Nordic Glacier.....	24
Table 2.2. Range of daily average error values.	45
Table 2.3. Performance of the tested bulk methods.....	50
Table 3.1. Locations and dates of operation of the automatic weather stations.	68
Table 3.2. Instrument list for each deployed station.....	70
Table 3.3. Dates of LiDAR flights.....	72
Table 3.4. EC-derived roughness length values.....	85
Table 3.5. Momentum roughness length values estimated using remote methods.....	91
Table 3.6. Comparison of momentum roughness length methods.....	94
Table 4.1. Performance of existing and modified parameterised methods.....	133
Table A.1. Directional remote roughness length estimates from block method.....	172
Table A.2. Directional remote roughness length estimates from profile method.....	173

List of Figures

Figure 1.1. The fluxes influencing the melt energy of a glacier surface.	4
Figure 2.1. Installed AWS on Nordic Glacier.....	25
Figure 2.2. Data preprocessing.	29
Figure 2.3. Meteorological data and surface energy fluxes on Nordic Glacier.	43
Figure 2.4. Observed and modelled surface height changes.....	46
Figure 2.5. Daily mean energy fluxes.	47
Figure 2.6. EC-derived and assumed roughness length values.....	48
Figure 2.7. Performance of the tested bulk methods	50
Figure 2.8. EC-derived scalar roughness lengths.....	55
Figure 2.9. Wind, air temperature, and stability.	56
Figure 2.10. Daily means of observed and modelled turbulent heat fluxes.....	57
Figure 2.11. Deviation from daily modelled melt energy.....	59
Figure 3.1. Location of the study glaciers and stations.....	69
Figure 3.2. DEM-based block method.....	77
Figure 3.3. DEM-based profile method.	81
Figure 3.4. DEM rotation.....	83
Figure 3.5. Microtopography and synthetic profiles.....	84
Figure 3.6. EC-derived momentum roughness values.	87
Figure 3.7. Surface renewal models.....	87
Figure 3.8. Block method steps.....	89

Figure 3.9. Flux footprint maps.	89
Figure 3.10. DEM profile method roughness estimates	92
Figure 3.11. EC-derived vs DEM momentum roughness lengths.	94
Figure 3.12. EC- derived momentum roughness length and wind direction.	96
Figure 3.13. DEM profile momentum roughness length and wind direction.	96
Figure 3.14. Snow surface roughness variations.	99
Figure 3.15. Comparison of downslope and cross-slope surface roughness.	103
Figure 3.16. DEM of coniferous forest.	104
Figure 4.1 Comparison of OPEC and CPEC fluxes.	115
Figure 4.2. Air temperature probe array.	115
Figure 4.3. Partitioning of the daily mean energy for each station.	123
Figure 4.4. Daily ratios of the turbulent heat fluxes to melt energy.	124
Figure 4.5. Mean daily cycle of turbulent heat flux contribution to melt energy.	125
Figure 4.6. Temporal variability in magnitude of the sensible heat flux.	126
Figure 4.7. Relationship wind direction, wind speed, and temperature.	128
Figure 4.8. Difference in wind speeds at two levels.	129
Figure 4.9. EC-observed friction velocity values.	129
Figure 4.10. Comparison of EC-observed and modelled friction velocity.	130
Figure 4.11. Friction velocity behaviour and katabatic conditions.	131
Figure 4.12. Turbulence parameterisation performance at each location.	132
Figure 4.13. Comparison of EC-derived and modelled stability parameters.	134
Figure 4.14. Parameterisation performance and katabatic winds	135
Figure 4.15. Wind shear and parameterisation performance.	136

Figure 4.16. Bulk method performance with adjusted friction velocity values.....	137
Figure B.1. Observed and SEB-modelled daily surface height decrease at each	175
Figure B.2. Wind speed and friction velocity.	175

Acknowledgements

I would like to begin by thanking my supervisor, Valentina Radić. I am grateful to you for the time and guidance given over the last four and a half years, and for taking me on as your first graduate student! Thank you also to my supervisory committee, Gwenn Flowers, Rosie Howard, and Andreas Christen for the direction and advice provided, and to Brian Menounos, for his collaboration on this project.

The success of the extensive field campaign undertaken in this project could not have been achieved without the help of several people. On nearly every glacier trip undertaken during my PhD, I was joined by my colleague and friend, Ben Pelto. My thanks to Ben for sharing the trials of long days and journeys, blizzards and thunderstorms, cold cooking spots, wind-borne tents, helicopter stresses, frozen and misbehaving equipment, and not to mention, many a stunning view! Joining in such adventures, has been a rotating cast of great people who have assisted me in the field, including Emilie Delaroche, Clemens Schannwell, Marzieh Morteza pour, Federico Ponce, Alex Bevington, and the crew of the ‘Melt’ documentary, Ethan Volberg, Kyler Dickey and Pierce Kinch. I am very grateful to Zoran Nestic for his advice on the design of the observation system, and on the calibration and preparation of sensors prior to fieldwork. My thanks, also, to Jörn Unger, who put shape to our design for the ‘quadpods’ on which the sensors were installed. A special thanks to Steve Conger and Tannis Dakin, who, from the beginning of this project, have generously donated their time and experience, and have always provided a much-welcome open door in

Golden after a long drive from Vancouver! Their help during my first field season, when I was getting to grips with glacier problems and helicopter logistics, was particularly appreciated!

Working in the glaciology group at the Department of Earth, Ocean and Atmospheric Sciences, I've been fortunate to get to know some great people, including Mekdes Tessema, who started with me in 2014, Arran Whiteford, Camilo Rada, Gabriela Racz, Sam Anderson, Maryam Zarrinderakht, Christen Schoof, Garry Clarke, Jennifer Walker, and many others who have passed through while I've been here. My thanks to you for your support and comradery, and to all the excellent people I've met in this department, at conferences, and in the mountains of Canada, Alaska and Svalbard! Thank you also to my colleagues at the Irish weather service, Met Éireann, for your support when I took my leave to return to university.

Leaving Ireland, my family and friends, my career, and the life I had there, to travel to the other side of the world to pursue a PhD was not an easy decision. I am very grateful for the support and understanding shown by those at home, without which, this would have been a significantly more difficult undertaking.

For my parents, Monica and Eamon Fitzpatrick.

Thank you for providing a consistent example of kindness, selflessness, and decency, and for being my first teachers. I have always been able to rely on your continuous encouragement and support, and it has kept me going forward on the journey you started for me.

Chapter 1:

Introduction and Motivation

1.1 Mountain Glaciers in a Warming Climate

The ongoing retreat of mountain glaciers is one of the key indicators of recent climate change, with current rates of ice loss estimated at 275 Gt y^{-1} (IPCC, 2013). Despite comprising less than 1% of the Earth's land-based ice (99% is contained in the Antarctic and Greenland ice sheets), the melting of mountain glaciers and ice caps is predicted to contribute approximately one third (0.1-0.2 m) of all sea level rise by 2100 (e.g. Radić and Hock, 2011; Marzeion *et al.*, 2012; Huss and Hock, 2015). On a more regional scale, mountain glaciers act as water reservoirs; storing water as snow and ice during cool, wet periods, and releasing water during warm, dry seasons through melting. This helps to regulate flow rates in rivers with glaciated basins, as well as influencing water temperatures (Stahl *et al.*, 2008). Some of the Earth's most densely populated communities depend on meltwater fed rivers, such as the Indus River of South Asia (Rasul, 2014). The change in flow of these rivers brought on by deglaciation may have a substantial impact on local freshwater supply, irrigation, hydroelectric power production, and flood frequency (Barnett *et al.*, 2005). The disruption of seasonal water temperature patterns due to changes in the timing and quantity of meltwater runoff may also affect the aquatic ecosystems dependent on these rivers, such as the migration and spawning success of Pacific salmon (Farrell *et al.*, 2008).

Future estimates of glacier mass balance up to the year 2100 indicate net losses of over 70% in some mountainous regions, including Western Canada, where few glaciers are predicted to remain in the Rockies by the end of the century (Clarke *et al.*, 2015). Considering the regional and global effects of mountain glacier retreat, it is essential that the future response of glaciers in a warming climate is accurately quantified. On shorter timescales, the management of local water resources and ecosystems in these regions requires precise modelling of melt and meltwater runoff. To achieve these goals, the processes that control the mass loss of a mountain glacier must first be understood.

1.2 Phase Change of Ice

As a glacier is predominately composed of ice and snow, mass loss relates to state changes of the water present. Surface melting is the dominant process of ablation (snow and ice loss) for land terminating glaciers (Benn and Evans, 2010). The specific heat capacity for ice (c_{p_ice}), that is, the energy required to heat 1 kg of ice by 1 K, is $2,097 \text{ J kg}^{-1} \text{ K}^{-1}$. When ice has been heated to its melting point (0°C at the standard atmospheric pressure of 1013.25 hPa), additional energy input is required for the phase shift to liquid water. This is known as the latent heat of fusion (L_f), with a value of $334,000 \text{ J kg}^{-1} \text{ K}^{-1}$ for ice. In some regions, sublimation (where snow and ice changes state directly into water vapour) can be an important ablation process. This phase change requires substantially more energy than for melting, with the latent heat of sublimation (L_s) of ice being $2,848,000 \text{ J kg}^{-1} \text{ K}^{-1}$. The capacity for sublimation is driven by the presence of strong humidity gradients between the surface and a dry atmosphere, therefore, limiting its importance to locations with cold, dry climates such as high elevation, low latitude glaciers, and the interior of the polar

ice sheets (Lewis *et al.*, 1998). The rate and mechanism of energy exchange between a glacier surface and its surroundings will determine how much energy is available for these phase changes, and hence, the potential for mass loss.

1.3 Glacier Surface Energy Balance

The study of glacier surface energy balance (SEB) examines the flow of energy in and out of a glacier surface, the pathways of this flow, and how the balance of this energy can be related to surface mass loss. As shown in Figure 1.1, there are eight main pathways or fluxes of energy that determine the energy available for melting (Q_M): the four radiation fluxes of incoming shortwave (S_i), reflected shortwave (S_r), incoming longwave (L_i), and outgoing longwave (L_o); turbulent fluxes of sensible and latent heat (Q_H and Q_L); rain heat flux (Q_R); and ground heat flux (Q_G):

$$S_i + S_r + L_i + L_o + Q_H + Q_L + Q_R + Q_G = Q_M \quad (1.1)$$

The relative contribution of each flux to a glacier's SEB, known as its energy partitioning, may vary depending on the climate type of that region, the elevation range of the glacier, and the local topographic effects on a glacier's meteorology (e.g. Arnold *et al.*, 2006; Van As, 2011; Cullen and Conway, 2015; Fausto *et al.*, 2016). Studies that implement a SEB-based approach to modelling glacial ablation endeavour to account for such spatial and temporal variability by determining the magnitude of each flux at a given location. Alternative approaches, such as temperature-index modelling, provide simpler, less data-intensive methods by using calibrated, empirical relationships between surface ablation and readily available meteorological variables, most commonly, air temperature (e.g. Carenzo *et al.*, 2009; Engelhardt *et al.*, 2013). The inherent dependency of such models on locally-derived melt factors may limit their transferability across

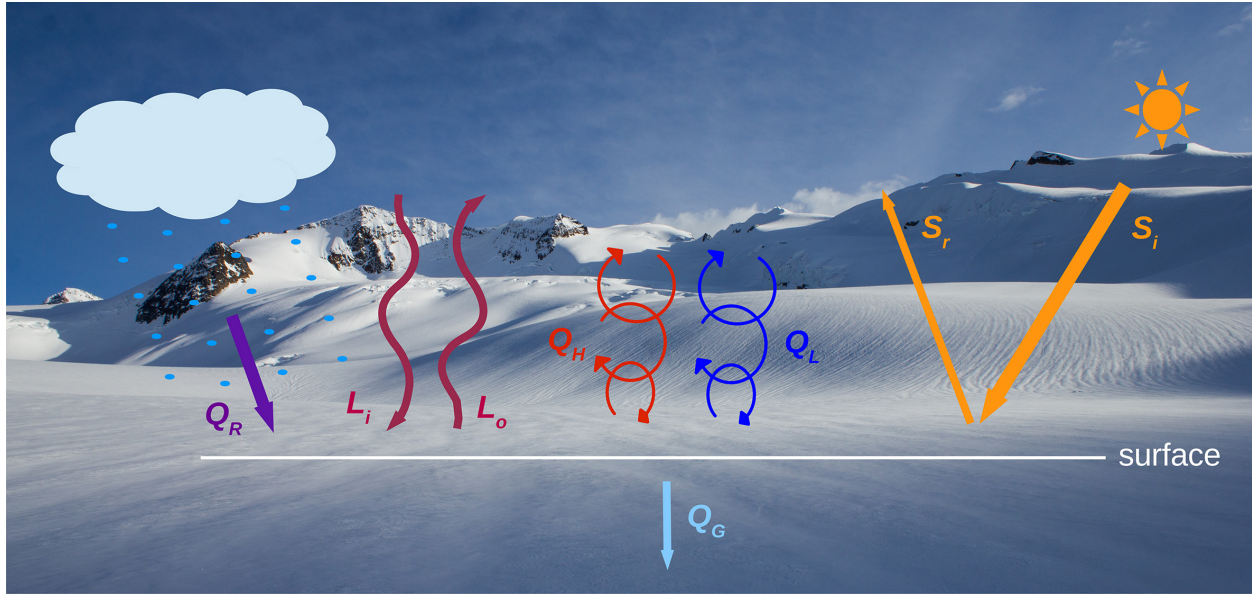


Figure 1.1. The fluxes influencing the melt energy (Q_M) of a glacier surface: incoming shortwave (S_i), reflected shortwave (S_r), incoming longwave (L_i), and outgoing longwave (L_o), sensible heat (Q_H), latent heat (Q_L), rain heat flux (Q_R), and ground heat flux (Q_G).

glaciers and regions, and add uncertainty to the temporal persistence of their performance in a changing climate where such relationships may vary with time (Huss *et al.*, 2008).

Complete datasets, containing direct observations of each of the SEB fluxes, are rare for glacier surfaces due to the extensive instrumentation required, and the difficulties in installing and operating such equipment in remote, harsh environments. Where SEB measurements do exist, they are generally limited to a reduced number of observed fluxes at individual points on the surface. Therefore, accurate, transferable methods for parameterising these fluxes are necessary for many reasons, including closing the energy budget in localised SEB studies where not all fluxes have been observed, providing spatial coverage of flux values in distributed SEB models, and for the modelling of glacier SEB and ablation on local and regional scales using data from remote sensing and climate models.

1.4 Radiation Fluxes

For mid-latitude glaciers, the radiation fluxes are generally considered to be the largest contributors to the SEB (e.g. Greuell and Smeets, 2001). While some studies have directly measured all four components (e.g. Sicart *et al.*, 2005; Giesen *et al.*, 2014), parameterisation of one or more of these fluxes is common. Reflected shortwave can be estimated by multiplying the incoming shortwave flux by a surface albedo value (e.g. Mölg and Hardy, 2004). Albedo, however, can be highly variable for a glacier surface, both spatially and temporally, and can range from 0.1 for dirty ice, to 0.9 for freshly fallen snow (Hock, 2005). The most commonly parameterised radiation component is outgoing longwave radiation (e.g. Cullen *et al.*, 2007; Mölg *et al.*, 2008). L_o can be estimated from surface temperature using the Stefan-Boltzmann law (see Section 2.4.3 in Chapter 2), with some studies assuming a constant surface temperature of 0°C, and therefore, a constant L_o flux of -316 W m^{-2} , approximately (e.g. Andreassen *et al.*, 2008). The incoming radiation fluxes have also been parameterised in previous studies, including the modelling of the direct and diffuse components of S_i using solar position and empirical transmissivity constants (e.g. Garnier and Ohmura, 1968; Hock and Holmgren, 2005), and the estimation of L_i from air temperature, humidity, and cloud amount (e.g. Plüss & Ohmura, 1997).

1.5 Ground and Rain Heat Fluxes

Temperature gradients within the snow/ice column of a glacier can result in a heat flux from warm to cold layers, known as the ground heat flux. Q_G can act as a substantial energy sink from the SEB on glaciers that contain persistent, cold sublayers (below melting point), such as those found at high latitudes and elevations, and on mid-latitude glaciers during the early melt season as the snow

and ice is being heated to melting point (Benn and Evans, 2010). For melt season studies on mid-latitude and maritime glaciers, Q_G is often assumed to be negligible, however, due to the tendency for the ice in these conditions to be temperate (uniformly at its melting point), and therefore, lack a sufficient temperature gradient (e.g. Gillett and Cullen, 2011). The rain heat flux, generated by the transfer of heat from liquid precipitation to the surface of the glacier, is also commonly assumed negligible (neither observed nor parameterised) as its potential contribution to the SEB on a seasonal scale is, generally, the smallest of the 8 fluxes (e.g. Sicart *et al.*, 2005; Andreassen *et al.*, 2008). On daily and sub-daily timescales, however, Q_R may have the potential to be a significant flux during heavy rainfall (see Section 2.6.1).

1.6 Turbulent Heat Fluxes

Air flow in the atmospheric boundary layer is often turbulent, composed of rotating air currents or ‘eddies’ of varying spatial and temporal dimensions, in addition to a mean wind flow. These eddies can be generated in a number of ways including by convection due to differential heating of the underlying surface, by wind shear due to friction with the surface, and by the flow of air around features or obstacles above ground. The portion of kinetic energy in a flow that is due to these eddies is known as the turbulence kinetic energy (TKE), and can be produced or consumed locally by the processes described above, or transported by advection with the mean wind (Stull, 1988). Turbulence can be an important mechanism in the transfer or flux of momentum, heat, and moisture in the boundary layer, particularly near the surface, where strong gradients in these quantities can exist (Pope, 2000). As air is a good insulator, the exchange of sensible heat between the atmosphere and surface is largely dependent on the bulk movement of air parcels to and from the surface by turbulent eddies. These eddies can also redistribute moisture between saturated and

unsaturated regions of the air column, enhancing phase change of water at the boundary, and driving the associated flux of latent heat.

The magnitude of the fluxes of Q_H and Q_L can be quantified by correlating high frequency observations of vertical wind speed (w) with those of potential temperature (θ) and specific humidity (q) (Stull, 1988):

$$Q_H = \overline{w'\theta'}\rho_a c_p , \quad (1.2)$$

$$Q_L = \overline{w'q'}\rho_a L_v , \quad (1.3)$$

where the prime denotes the turbulent component, the overbar denotes a mean value, ρ_a is air density, c_p is the specific heat capacity of air (1,005 J kg⁻¹ K⁻¹), and L_v is the latent heat of vapourisation (2.514 MJ kg⁻¹), substituted with L_s when surface temperature is below 0°C and sublimation may occur. The turbulent components are determined through Reynold's averaging, where the instantaneous observation is subtracted from an average value (usually over a 30-minute period) of the variable (Foken, 2008):

$$w' = \bar{w} - w , \quad (1.4)$$

$$\theta' = \bar{\theta} - \theta , \quad (1.5)$$

$$q' = \bar{q} - q . \quad (1.6)$$

In most cases, the turbulent fluxes of sensible and latent heat are the largest component of glacier SEB after radiation, and in locations with maritime climates, can be the dominant source of melt energy (e.g. Anderson *et al.*, 2010). With a strong dependence on air temperature and vapour content, they are also one of the components of SEB most sensitive to potential atmospheric adjustments driven by climate change (Van Der Avoird and Duynkerke, 1999). Despite this importance, direct measurements of Q_H and Q_L on glacier surfaces are extremely rare. While

methods used to observe the turbulent fluxes, such as eddy covariance (see Sections 2.3 and 2.4), have seen extensive use in forestry and land science research (e.g. Paul-Limoges *et al.* 2013; Li *et al.*, 2017), implementation of these methods over glaciers has been limited due to the complexity and power requirements of such systems, and the sensitivity of the instruments to correct installation and adverse weather conditions.

1.6.1 Turbulent Flux Parameterisation

To account for an absence of direct observations, the turbulent heat fluxes are parameterised in most glacier SEB studies and models (e.g. Moore, 1983; Hay and Fitzharris, 1988; Arnold *et al.*, 2006; Anderson *et al.*, 2010; Van As, 2011). The correlation terms (e.g. $\overline{w'\theta'}$) in the flux equations (Equations 1.2 and 1.3) are parameterised using a local first order closure method known as the gradient transport or ‘K’ theory, where the turbulent flux is related to the vertical gradient in the mean variable of interest (Stull, 1988):

$$\overline{w'\theta'} = -K_H \frac{\partial \bar{\theta}}{\partial z}, \quad (1.7)$$

$$\overline{w'q'} = -K_E \frac{\partial \bar{q}}{\partial z}, \quad (1.8)$$

where $K_{H/E}$ is the eddy diffusivity for heat/moisture. This approach allows for the estimation of the fluxes from mean values of standard meteorological variables (e.g. wind speed, air temperature, humidity), following the assumptions of Monin-Obukhov similarity theory (Monin and Obukhov, 1954). Two common versions of this parameterisation are the profile and bulk aerodynamic methods. In the profile method, the gradient terms in Equations 1.7 and 1.8 are determined from measurements of the above mean variables at two or more heights above the surface (e.g. de La Casinière, 1974; Berkowicz and Prahm, 1982; Brock *et al.*, 2006). Such observations require mast-

based instrumentation, which can be difficult to install and maintain on a melting ice surface. Furthermore, the profile method has been shown to be highly sensitive to measurement errors and the accurate establishment of the measurement heights (e.g. Bintanja and Van den Broeke, 1995; Denby and Greuell, 2000; Hock, 2005). The most frequently used parameterisation in recent SEB studies is the bulk aerodynamic method (see Section 2.3), due to its capacity to estimate the fluxes from observations at a single measurement height and the surface. With the surface conditions of a melting glacier often assumed (wind speed at 0 ms^{-1} , air saturated at 0°C), the number of required measurements and sensors is greatly reduced. In the bulk method, the K theory equations are integrated between the surface (s) and a single measurement height (z), assuming constant values for wind shear and turbulent flux, to estimate surface fluxes from finite differences in wind speed, air temperature (T), and humidity (Denby and Greuell, 2000; Radić *et al.*, 2017):

$$Q_H = \rho_a c_p C \bar{u} (\bar{T}_z - \bar{T}_s) , \quad (1.9)$$

$$Q_L = \rho_a L_v C \bar{u} (\bar{q}_z - \bar{q}_s) . \quad (1.10)$$

The bulk transfer coefficient (C) represents the eddy diffusivity for T or q through the surface layer. Considering the previously mentioned reliance of turbulence generation on convection and wind shear, the bulk transfer coefficient introduces the influence of atmospheric stability and surface roughness into the flux parameterisation (Foken, 2008). Several methods have been employed to determine C in previous SEB studies (see Sections 2.4.5 and 4.3.5). However, substantial uncertainty exists in the validity of these methods over glacier surfaces, compounded by a lack of observed data with which to evaluate their performance.

1.6.2 Roughness Lengths

The influence of surface roughness on the turbulent heat fluxes is represented in the bulk parameterisation by the roughness lengths for momentum (z_{0v}), temperature (z_{0t}), and water vapour (z_{0q}). They represent the lower limits of the vertical profile over which the bulk-gradient expressions are integrated (see Section 2.3), and can be thought of as the height above the surface at which wind speed, temperature, and water vapour, extrapolated downwards along an assumed logarithmic profile, will reach their surface value (Stull, 1988). z_{0v} accounts for the effects of form drag on the near-surface wind profile due to the interaction of airflow with features on the surface. The majority of glacier SEB studies use z_{0v} values obtained from previous research on surfaces deemed to be similar, rather than obtain site-specific values, with the utilised values often assumed constant with time (e.g. Giesen *et al.*, 2014). Comparing studies where measurements have been obtained, however, indicates a large range of z_{0v} values (several orders of magnitude) between different glaciers and regions of the same glacier (Brock *et al.*, 2010). Furthermore, the methods used to measure roughness lengths in the above studies are usually spatially limited, providing point values, only. Implementing a uniform, constant value for z_{0v} over an entire glacier or several glaciers will not account for the extensive spatial and temporal variability that can exist in surface roughness (as discussed in Chapter 3). An increase in z_{0v} of one order of magnitude can double the value of the turbulent flux estimated through the bulk method, highlighting the importance of accurately constraining z_{0v} for a given location.

Molecular diffusion controls the rate of scalar transfer with a surface, and having a smaller spatial scale than the form drag processes driving momentum transfer, it is likely that the roughness lengths for temperature and water vapour would be smaller than that for momentum (Beljaars and Holtslag, 1991). z_{0t} and z_{0q} , however, are commonly assumed in glacier SEB studies and climate

models to be equal to z_{0v} (e.g. Sicart *et al.*, 2005), while other studies assume fixed ratios between the scalar and momentum roughness lengths (e.g. Hock and Holmgren, 2005). The validity and persistence of such ratios over time and space is uncertain, however.

1.6.3 Stability Corrections

Over flat surfaces, atmospheric stability can influence turbulent transfer in the boundary layer, with buoyant suppression of turbulence during stable conditions, and enhancement through convection during unstable conditions. To estimate the turbulent fluxes from measurements of wind speed, temperature and humidity from a single level, the bulk method assumes logarithmic or log-linear profiles of these variables between their height of measurement and the surface. Such profiles are valid only in a neutral atmosphere, and a series of stability functions have been developed to correct for non-neutral conditions (see Section 2.4.5). With a surface temperature limited to a maximum of 0°C, the boundary layer over a glacier is frequently stable, necessitating application of such a correction. Glacier surfaces are rarely flat, however. The aforementioned stable stratification, combined with a sloped surface, can lead to the development of density-driven, downslope airflow, known as katabatic wind (Denby, 1999). In such a regime, the near-surface profiles of these variables, and of the turbulent fluxes, can differ substantially from those over the flat terrain for which the stability corrections were developed (as discussed in Chapter 4). Despite this, glacier SEB studies routinely employ these functions when estimating the turbulent fluxes, with few attempts to evaluate their performance with observed data (e.g. Conway and Cullen, 2013).

1.7 Research Aim and Questions

The need for accurate determination of glacier surface energy balance, and its associated effects on mass loss, has been highlighted in this chapter. Limiting factors in realising this have also been identified, including the scarcity of direct observations, and the uncertainties in commonly used parameterisation methods. The overarching aim of this study was to obtain a comprehensive SEB and meteorology dataset with which to investigate the processes at the atmosphere-glacier boundary affecting melt. A focus was to be given to the turbulent heat fluxes, and to an evaluation of common assumptions made in their estimation. Achieving this would allow future studies to make more informed choices regarding observation and parameterisation methods, and help quantify the uncertainty in their findings. Where possible, it was also hoped to develop or refine methods that would help reduce this uncertainty and facilitate the widespread application of SEB analysis to glaciers. More specifically, a series of questions have been posed in this thesis, grouped below into four main categories: (i) SEB observation and ablation modelling; (ii) Importance of turbulent heat flux and its parameterisation for glacier surfaces; (iii) Roughness length variability and estimation; (iv) The role of stability and slope.

SEB observation and ablation modelling

- Can closure of the surface energy balance and accurate ablation modelling be obtained through direct observation of the heat fluxes on a glacier surface?
- What are the main sources of uncertainty in such observations?
- What is the partitioning of the SEB at the test locations, and is it valid to assume that the contribution of certain fluxes to melt energy is negligible?

Importance of turbulent heat flux and its parameterisation for glacier surfaces

- What is the importance of the turbulent heat fluxes to glacier SEB, and how does this importance vary between different locations and over different timescales?
- How well do current parameterisation techniques perform in estimating the turbulent heat fluxes for glacier surfaces, and to what is this performance most sensitive?

Roughness length variability and estimation

- Do commonly assumed values and ratios for roughness lengths over glaciers compare well with observed data, and how do these assumptions impact flux parameterisation?
- How variable are the roughness lengths, and how transferable are their values in time and space?
- Can methods be developed to estimate roughness lengths over entire glacier surfaces?

The role of stability and slope

- How sensitive is turbulent flux parameterisation over a glacier to the choice of stability function?
- Do existing stability parameters and functions perform well in identifying and adjusting for periods of over- or underestimation of the parameterised fluxes on glacier surfaces?
- How might the slope of the surface and the development of katabatic conditions influence the performance of turbulent flux parameterisation on glaciers?

1.8 Thesis Outline and Key Elements

To address the questions stated above, the remaining chapters of this thesis will present the analysis performed on a new, extensive dataset, obtained in this study, for glacier SEB. The dataset resulting from this project is composed of *in situ*, high temporal resolution observations from five monitoring stations, deployed on two glaciers over three melt seasons (2014–2016). Continuous, direct observation of the surface energy fluxes and surface ablation was performed at each station, as was measurement of a suite of other meteorological and glaciological variables. The dataset includes continuous measurements of the turbulent heat fluxes at each location, obtained through eddy covariance methods.

The glaciers, Nordic and Conrad, are located in the Purcell Mountains of British Columbia (BC), Canada. Nordic (51°26' N, 117°42'W) is a small (~5 km²), north-facing glacier, ranging in elevation from 2,000 m to 2,900 m above sea level (a.s.l.), approximately. Conrad Glacier (50°49' N, 116°55'W) is located 87 km to the southeast of Nordic, with an area of ~15 km², and an elevation range of 1,800m to 3,200 m a.s.l., approximately. These glaciers are situated within the Columbia River basin, a vital water source for irrigation and hydroelectric power production in BC and the United States, and an important aquatic environment (Columbia Basin Trust, 2017). Previous studies within this basin indicate that glacier meltwater may contribute up to a third of total streamflow during summer months (Jost *et al.*, 2012). The region is currently subject to a humid continental climate, with the intermittent influence of maritime low-pressure systems. Predicted climate scenarios for the end of this century suggest a 70-95% loss of glacier mass in this region, relative to 2005, and declining flow contributions to the Columbia River after a peak in meltwater discharge around 2050 (Clarke *et al.*, 2015).

Chapter 2 of this thesis presents an analysis of the SEB of Nordic Glacier, and an evaluation of commonly used turbulent flux parameterisations. The initial development of the observation and analysis techniques used in this project are presented, along with a series of methods to quantify and address measurement uncertainties. Flux measurements are used to drive a point SEB model which shows good agreement with observed ablation at seasonal, daily, and sub-daily timescales. The turbulent heat fluxes are found to be an important contributor to melt energy at this location, and these observed values are compared with estimates from a range of bulk methods. The performances of these parameterisations are found to be highly sensitive to the choice of roughness length and stability scheme, and to have a substantial impact on the overall performance of the SEB model. The contents of this chapter have been published in Fitzpatrick *et al.* (2017).

Considering the sensitivities identified in turbulent heat flux parameterisation in Chapter 2, the spatial and temporal variability of the roughness lengths over glaciers is examined in Chapter 3. Roughness lengths observed over multiple seasons and locations are found to differ from those commonly assumed for snow and ice surfaces in SEB models, and to vary substantially between glaciers, and across the surface of a glacier, highlighting the importance of site-specific values. To address the difficulty in obtaining such values, two methods to estimate z_{0v} through remote sensing are developed here. Digital elevation models are obtained of each study site through LiDAR imaging, to which these methods are applied. The developed techniques are shown to perform well over most surfaces, differentiating between ice and snow cover, and returning momentum roughness length values that agree with *in situ* observations.

In Chapter 4, the complete dataset from all stations and seasons is analysed to investigate variation in glacier SEB, and the relative importance of the turbulent heat fluxes, across the study locations and over a range of timescales. Variation in the performance of bulk parameterisation

methods, and potential causes for such variation, are also examined. Identified in Chapter 2 as a key source of uncertainty, particular focus is given to the validity of the applied stability functions for turbulent flux parameterisation over sloped glaciers. When compared with observations, substantial variation is noted in parameterisation performance over time and between locations, for which, the employed stability functions cannot account. The development of a low-level wind maximum close to the surface during katabatic conditions is identified as a potential driver of this variability. The associated departure of the wind shear profile from the assumed constant profile of the bulk aerodynamic method is found to dominate as a source of uncertainty over assumed stability effects, and methods to detect such conditions from mean meteorological data are proposed.

Finally, Chapter 5 collates the key findings from this study, in context of the questions posed here, and identifies the main contributions to the field and potential directions for future research.

Chapter 2:

Surface energy balance closure and turbulent flux parameterisation on a mid-latitude mountain glacier, Purcell Mountains, Canada

2.1 Summary

In the majority of glacier surface energy balance studies, parameterisation rather than direct measurement is used to estimate one or more of the individual heat fluxes, with others, such as the rain and ground heat fluxes, often deemed negligible. Turbulent fluxes of sensible and latent heat are commonly parameterised using the bulk aerodynamic technique. This method was developed for horizontal, uniform surfaces rather than sloped, inhomogeneous glacier terrain, and substantial uncertainty remains regarding the selection of appropriate roughness length values, and the validity of the atmospheric stability functions employed. A customised weather station, designed to measure all relevant heat fluxes, was installed on an alpine glacier over the 2014 melt season. Eddy covariance techniques were used to observe the turbulent heat fluxes, and to calculate site-specific roughness values. The obtained dataset was used to drive a point ablation model, and to evaluate the most commonly used bulk methods and roughness length schemes in the literature. Modelled ablation showed good agreement with observed rates at seasonal, daily, and sub-daily timescales, effectively closing the surface energy balance, and giving a high level of confidence in the flux

observation method. Net radiation was the dominant contributor to melt energy over the season (65.2%), followed by the sensible heat flux (29.7%), while the rain heat flux was observed to be a significant contributor on daily timescales during periods of persistent heavy rain (up to 20% day⁻¹). Momentum roughness lengths observed for the study surface (snow: $10^{-3.8}$ m; ice: $10^{-2.2}$ m) showed general agreement with previous findings, while the scalar values (temperature: $10^{-4.6}$ m; water vapour: 10^{-6} m) differed significantly from those for momentum, disagreeing with the assumption of equal roughness lengths. Of the three bulk method stability schemes tested, the functions based on the Obukhov length returned mean daily flux values closest to those observed, but displayed poor performance on sub-daily timescales, and periods of substantial flux overestimation.

2.2 Introduction

The observed large-scale retreat of mountain glaciers is a primary indicator of current climate change, and the loss of mass from these systems may have significant future impacts on sea level rise, freshwater supply, hydroelectric power production, and aquatic habitats (IPCC, 2013). In Western Canada, glaciers are projected to lose $70 \pm 10\%$ of their volume by the end of this century, relative to 2005 (Clarke *et al.*, 2015). Enhanced understanding of the processes taking place at the ice–atmosphere boundary, and the role of these processes in glacier melt, is vital for improving both long-term predictions of glacier mass balance, and short-term modelling of meltwater runoff. Utilising a surface energy balance (SEB) model can reduce the reliance on local, empirically-derived melt relationships used in other modelling techniques (e.g. temperature index models) which can vary spatially and temporally, requiring calibration for each glacier, and limiting transferability. However, *in situ* measurements of the complete SEB are rare on glacier surfaces,

necessitating the use of parameterisation methods for one or more of the energy fluxes in the majority of studies. Following radiation, the turbulent fluxes of sensible and latent heat (Q_H and Q_L) are generally assumed to be the next largest contributors to surface melt energy, and in some cases, can dominate the budget on daily and seasonal timescales (e.g. Anderson *et al.*, 2010). Direct observations of Q_H and Q_L are scarce on glacier surfaces, however. The parameterisation methods commonly used to estimate these fluxes contain substantial uncertainties, with a lack of observed data to evaluate their performance.

A small number of glacier SEB studies have attempted to measure Q_H and Q_L directly using the eddy covariance (EC) technique (e.g. Munro, 1989; Cullen *et al.*, 2007; Litt *et al.*, 2015). The installation and power requirements of this technique, along with difficulties in fulfilling the necessary measurement assumptions (outlined in Section 2.3) have limited the use of EC systems in glacial settings, and the length of useable datasets where measurements exist. As a result of these challenges, Q_H and Q_L have been parameterised in the vast majority of SEB studies, utilising the bulk aerodynamic method (e.g. Hay and Fitzharris, 1988; Arnold *et al.*, 2006; Anderson *et al.*, 2010; Van As, 2011). One of the largest sources of uncertainty in using the bulk method arises from the selection of appropriate values for the roughness lengths of momentum (z_{0v}), temperature (z_{0t}), and water vapour (z_{0q}). Where observations of z_{0v} exist, differences of several orders of magnitude across a range of glacier surfaces have been identified (Brock *et al.* 2006). However, the majority of SEB studies do not have access to site-specific z_{0v} observations, and instead select values from existing studies on surfaces deemed to have similar characteristics to the glacier of interest (e.g. Mölg and Hardy, 2004; Gillett and Cullen, 2011; Giesen *et al.*, 2014). z_{0v} is often assumed to remain constant with time, with some studies implementing different values for when the surface is snow or ice covered. A range of methods have been used for expressing the

relationship between z_{0v} , and the scalar roughness values of z_{0t} and z_{0q} , including the assumption that the three roughness lengths are equal (e.g. Gillett and Cullen, 2011; Dadić *et al.*, 2013). It would be expected, however, that z_{0v} be different, and potentially considerably larger than z_{0t} and z_{0q} , as the surface properties governing momentum and scalar transport (form drag and molecular diffusion, respectively) have different spatial scales (Beljaars and Holtslag, 1991). To account for this, some studies implement a ratio of $z_{0v}/10$ or $z_{0v}/100$ to express z_{0t} and z_{0q} (e.g. Hock and Holmgren, 2005). The surface renewal model proposed by Andreas (1987) for determining z_{0t} and z_{0q} over snow and sea ice (from a given z_{0v} value) is also commonly implemented in glaciology studies (e.g. Giesen *et al.*, 2014).

The bulk method assumes a logarithmic wind speed profile with height; an assumption only valid in statically neutral surface layers (Stull, 1988). Some studies attempt to account for the effects of varying atmospheric stability by introducing corrections, such as those based on the bulk Richardson number Ri_b (e.g. Sicart *et al.*, 2005), and the Obukhov length L (e.g. Van den Broeke *et al.*, 2005). These empirically-derived stability functions were developed over horizontal, homogeneous terrain, often cropland or forestry, and uncertainty remains regarding the validity of these corrections over inhomogeneous, sloped glacier surfaces. In particular, the assumptions of the Monin-Obukhov similarity theory (e.g. constant flux layer, stationarity, negligible advection) may not hold during strongly stable atmospheric conditions over glaciers, when the development of density driven, downslope ‘katabatic’ winds is common. Wind speed profiles with a maximum close to the surface can exist in these conditions, resulting in steep eddy diffusivity gradients, and a suppressed constant flux layer, decoupling the fluxes calculated at measurement height from the true surface values (Denby and Greuell, 2000; Grisogono and Oerlemans, 2001).

In summary, glacier SEB models generally rely on some form of parameterisation to close the energy budget, due to an absence of observed values for fluxes of interest. This lack of direct measurement, however, particularly in the case of the turbulent heat fluxes, has limited the opportunities to evaluate the employed parameterisation techniques, and to better understand the underlying atmospheric–glacial processes. To address these issues, the initial goal of this study is to obtain an accurate, season-long dataset of the complete SEB on a sloped glacier surface. Direct observations of each flux, including those of the turbulent heat fluxes obtained through EC methods, will be used to drive a point SEB ablation model, and to assess the relative contribution of each flux to melt energy on the study glacier i.e the energy partitioning. The performance of the SEB model in simulating observed surface ablation will indicate the ability of the employed measurement and data processing techniques to successfully capture glacier SEB. With confidence achieved in the reliability of the observed data, the performance of commonly used bulk method parameterisations of the turbulent heat fluxes will be evaluated through comparison with EC observations. This will include a comparison of commonly assumed roughness length schemes with EC-derived values for the study site. The overall impact of the choice of turbulent flux parameterisation on SEB model performance will then be assessed.

2.3 SEB Background

SEB models attempt to account for all the energy terms contributing to mass changes at the glacier surface; a goal referred to as ‘closing’ the energy budget. These terms include the four radiation fluxes of incoming shortwave (S_i), reflected shortwave (S_r), incoming longwave (L_i), and outgoing longwave (L_o), the four often combined into the net radiation flux (Q_N), the turbulent fluxes of sensible and latent heat, the heat flux due to rain (Q_R), and the ground heat flux due to

temperature gradients in the ice (Q_G). SEB models utilise measurements or estimates of the above fluxes, in order to determine the energy available for melting, Q_M (e.g. Cullen *et al.*, 2007; Giesen *et al.*, 2014):

$$S_i + S_r + L_i + L_o + Q_H + Q_L + Q_R + Q_G = Q_M \quad (2.1)$$

with Q_R and Q_G often deemed negligible in studies on mid-latitude glaciers (e.g. Sicart *et al.*, 2005; Andreassen *et al.*, 2008; Gillett and Cullen, 2011). For the direct measurement of Q_H and Q_L , the EC technique correlates high frequency measurements of the turbulent components of vertical wind speed (w) with those of potential temperature (θ) and specific humidity (q), to determine the magnitude and direction of the fluxes:

$$Q_H = \overline{w'\theta'} \rho_a c_p, \quad (2.2)$$

$$Q_L = \overline{w'q'} \rho_a L_v, \quad (2.3)$$

where the prime denotes the turbulent component, the overbar denotes a mean value (generally averaged over 30 minutes), ρ_a is air density (calculated from observed atmospheric pressure), c_p is the specific heat capacity of air ($1,005 \text{ J kg}^{-1} \text{ K}^{-1}$), and L_v is the latent heat of vapourisation (2.514 MJ kg^{-1}), substituted with the latent heat of sublimation ($L_s = 2.848 \text{ MJ kg}^{-1}$) if surface temperature is below 0°C . A range of assumptions are generally required to be satisfied in order for EC measurements to be considered valid (Burba, 2013), including: i) observations are taken within the constant flux layer where fluxes are representative of the surface of interest; ii) the footprint (upwind source area for the turbulence observed at the sensor) is homogeneous and representative of the study site; iii) turbulence is fully developed and stationary with minimum flow divergence/convergence; and iv) the sensor installation itself is not disrupting air flow (Lee *et al.*, 2004; Aubinet *et al.*, 2012).

For parameterising Q_H and Q_L , the bulk aerodynamic method employs an integrated form of the gradient transport or ‘K-closure’ theory equation for turbulent flux (Stull, 1988). The unknown terms in Equations 2.2 and 2.3 i.e. $\overline{w'\theta'}$ and $\overline{w'q'}$, are described using mean values of wind speed (u), and the finite differences in mean values of air temperature (T) and specific humidity between the surface (s), and a single measurement height (z):

$$Q_H = \rho_a c_p C \bar{u} (\bar{T}_z - \bar{T}_s), \quad (2.4)$$

$$Q_L = \rho_a L_v C \bar{u} (\bar{q}_z - \bar{q}_s). \quad (2.5)$$

The bulk transfer coefficient (C) represents the eddy diffusivity for θ or q through the surface layer. It is derived from the logarithmic wind speed profile equation, and is a function of measurement height and the roughness length values for momentum (z_{0v}), temperature (z_{0t}), and water vapour (z_{0q}). As mentioned, a range of functions have been applied to C to account for the effects of atmospheric stability on the turbulent transfer of momentum and scalars (detailed in Section 2.4.5).

2.4 Data and Methods

2.4.1 Station Design

A customised automatic weather station (AWS) was developed for use in this project. The station housed a suite of meteorological sensors (Table 2.1), including a four component radiometer to measure each of the radiation fluxes, and a tipping bucket rain gauge to observe precipitation (and calculate Q_R). The temperature profile of the surface layer of ice was measured for the calculation of Q_G using two thermistor arrays drilled into an initial depth of 4 m, with thermistor spacing of

Table 2.1. Instrumentation used on Nordic Glacier.

Variable	Sensor	Manufacturer's stated accuracy
Wind speed/direction	Young 05103ap Wind Monitor	$\pm 0.3 \text{ m s}^{-1}$
Air temperature/humidity	Rotronic HC2 Probe + shield	$\pm 0.1 \text{ }^\circ\text{C} / 0.8\%$
Atmospheric Pressure	Vaisala PTB110 Barometer	$\pm 0.3 \text{ hPa}$
Precipitation	Texas Electronics Tipping Bucket Gauge	$\pm 1\%$ (up to 10 mm hr^{-1})
Radiation fluxes	Kipp & Zonen CNR4 Radiometer	<5% (pyranometer) <10% (pyrgeometer)
Turbulence:	CSI IRGASON:	
Water vapour	Open path gas analyser	$\pm 3.5 \times 10^{-3} \text{ gm}^{-3}$
3D wind (u,v,w)	Sonic Anemometer	$\pm 1 \text{ mm s}^{-1}$
Sonic temperature	Sonic Anemometer	$\pm 0.025^\circ\text{C}$
Ground heat flux	Thermistor Array (self-made)	$\pm 0.1 \text{ }^\circ\text{C}$
Surface height	CSI SR50A Sonic Ranger	$\pm 0.01 \text{ m}$
Station Tilt	Turck Inclinometer	$\pm 0.5^\circ$
Data Storage	CSI CR3000 Logger	
Site/Surface Conditions	Time Lapse Camera (self-made)	

0.25 m in the upper 1 m, and 1 m in the lower 3 m. A sonic ranger was used to observe changes in surface height due to ablation or snowfall. To directly measure the turbulent heat fluxes, the EC method was employed. A combined sensor, comprising a sonic anemometer and an open path infrared gas analyser was selected for this campaign. With this design, the anemometer and analyser components instantaneously measure the same sample volume, minimising temporal and spatial errors due to the physical separation of the sensors. The sampling frequency of the EC measurements was 20 Hz, with the values averaged over 30-minute blocks when calculating the magnitude and direction of the turbulent fluxes.

In the atmospheric surface layer, significant gradients with height of temperature, humidity, and wind speed are typical. Therefore, it is important that meteorological sensors are maintained at a constant height above the surface if comparable measurements over time are

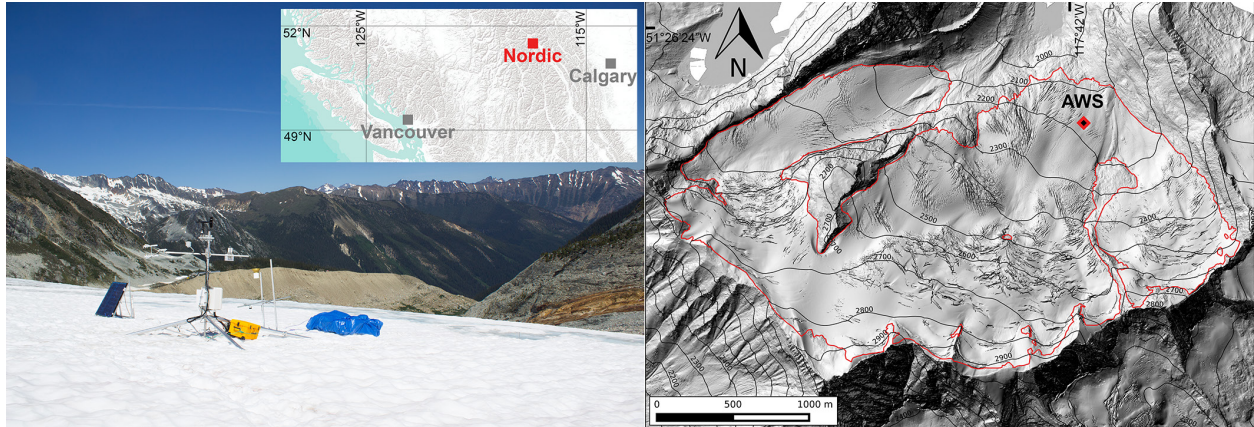


Figure 2.1. Installed AWS (as viewed by the time lapse camera), and its location on Nordic Glacier (red outline over LiDAR imagery) in the Purcell Mountains, BC, Canada, during the 2014 melt season.

required. The EC sensors are particularly sensitive to height changes, as increasing the height of the EC sensor may change the footprint from which the turbulence observed by the sensor is received (Burba, 2013). The sensor will also be at an increased risk of being positioned above the surface layer during strongly stable conditions, meaning that the sensor would no longer be observing eddies with characteristics of the glacier surface fluxes (Aubinet, 2008). To avoid these errors, the main meteorological sensors (including the EC system) were installed on a custom-built four-legged ‘quadpod’, which sits on the surface of the glacier (rather than being drilled in place), and lowers with the surface during the melt season (Figure 2.1). This ensured that the sensors maintained a constant height above the surface (wind monitor height z_u : 2.6 m, EC and temperature/humidity sensors height z : 2.0 m; radiometer height: 1.6 m). In order to monitor and correct for any tilting of the station that may occur over the season, an inclinometer was fitted to the quadpod to record its tilt angle in the x and y planes. The sonic ranger, along with the rain gauge, was mounted on a separate mast that was drilled into the ice, so that relative changes in glacier surface height could be measured. Observations were saved in one-minute averages (one-

minute totals for rainfall; 30-minute samples for ice thermistors), while the eddy covariance data was stored in raw (20 Hz) format. A time lapse camera was also installed onsite, recording eight images per day of the surface and atmospheric conditions, and the general position and order of the AWS.

2.4.2 Field Campaign

The described AWS was deployed during the summer of 2014 on Nordic Glacier (51°26'N, 117°42'W) in the Purcell Mountains in eastern British Columbia (BC), Canada. Nordic is a small (~5 km²), north-facing glacier, with an elevation range from 2000 to 2900 m a.s.l. (meters above sea level), approximately (Figure 2.1). The glacier is within the basin of the Columbia River; an important aquatic environment, and water source for irrigation and hydroelectric power production in BC, and the United States (Columbia Basin Trust, 2017). Previous studies within this basin indicate that glacier runoff may contribute up to a third of total streamflow during summer months (Jost *et al.*, 2012). The AWS was installed in the ablation zone of the glacier (2200 m a.s.l.) from July 11th to August 28th 2014, with the first and last days of measurements excluded from the study, to avoid contamination of the data due to installation activity. The study period therefore runs for 47 days from 00:00 on July 12th, day of year (DOY) 193, to 23:30 on August 27th (DOY 239). The station site was selected in the area with the lowest surface slope angle (13°), and with the most uniform upwind footprint, to help minimise the corrections required when processing the radiation and EC data. The station was orientated so that the radiometer was located on the south side of the structure, in order to avoid shadowing of the sensor. The main axis of the EC instrument was positioned to point upslope into the direction of the prevailing wind (downslope flow), to minimise flow distortion due to air flow through the station structure. The AWS performed reliably over the

study period, with the quadpod remaining stable throughout (tilting $< 2^\circ$), the power system maintaining an adequate supply, and the data from all sensors (including the camera) being consistently logged without any evident systematic errors. One of the main concerns prior to deployment, was the reliability of an unattended EC system in a harsh environment for an extended period of time. Calibration of the sensor before and after deployment showed negligible drift in its measurements over the season, while the signal strength of the gas analyser (excluding rain events) decreased from 99% to 97%, staying well above the manufacturer recommended quality cut off point of 70% (Campbell Scientific Inc., 2013).

2.4.3 AWS Data Treatment

Eddy Covariance Data

The EC data underwent a series of preprocessing steps prior to retrieving the 30-minute turbulent fluxes of sensible and latent heat. Relative to the air flow on a glacier, the sonic anemometer cannot be leveled perfectly i.e. its vertical (z) axis will not be perpendicular to the mean flow. The vertical wind component (w) as measured by the sensor will thus be contaminated by contributions from the horizontal (u and v) components. To correct for this, the sonic anemometer data must undergo coordinate rotation. For the complex, sloping terrain of a mountain glacier, where the mean vertical wind (\bar{w}) may be non-zero, the double rotation method may not be suitable, and therefore, a planar fit method has been implemented for this study (Wilczak et al., 2001). Long term measurements of u , v , and w are used to construct a hypothetical plane to which the w axis is set perpendicular. The features and slope of a glacier surface can change over a melt season, however, meaning this hypothetical plane may not be valid over an entire period. In this study, the planar fit calculations

were performed in one week blocks (seven times in total), to account for the ongoing evolution of the surface. As the gas analyser component of the open path EC system measures the molar/mass density (g m^{-3}) of water vapour in the sample space, variations in air density due to changes in temperature will cause fluctuations in the water vapour density measurements which are independent of changes in the turbulent fluxes. The widely used Webb-Pearman-Leuning correction (Webb *et al.*, 1980) has been implemented to account for these fluctuations. Additional preprocessing steps were taken to correct for potential high and low frequency flux loss using methods following Ibrom *et al.* (2007), and Moncrieff *et al.* (2004), respectively.

The open path gas analyser can be susceptible to spurious readings during precipitation events due to the build-up of droplets or snowflakes on the sensor windows, leading to inaccurate Q_L observations. The EC Q_L values from periods with observed precipitation and the following 90 minutes (309 values; 13.7%) were therefore removed from the dataset (Figure 2.2B). This period length was selected based on testing of the sensor prior to deployment, which showed approximately a 90-minute recovery period after rainfall for the windows to dry and the signal strength to normalise. Both fluxes were also subjected to a test of stationarity (Foken, 2008). Q_H and Q_L were found to be nonstationary for 15.4% and 24.5% of the observation period, respectively (Figure 2.2A-B). For assessing the performance of the bulk aerodynamic method, and for the calculation of roughness lengths, rain affected and nonstationary periods were excluded from the analysis. For the calculation of SEB and modelled ablation, rainfall and nonstationary gaps in the EC data were infilled using an optimised bulk method; the details of which are described in Section 2.4.5. While there is uncertainty regarding the validity of the bulk method during nonstationary conditions, it was selected as the best available approach in this study, and returned a more realistic range of flux values than the EC data during these conditions (Figure 2.2A-B).

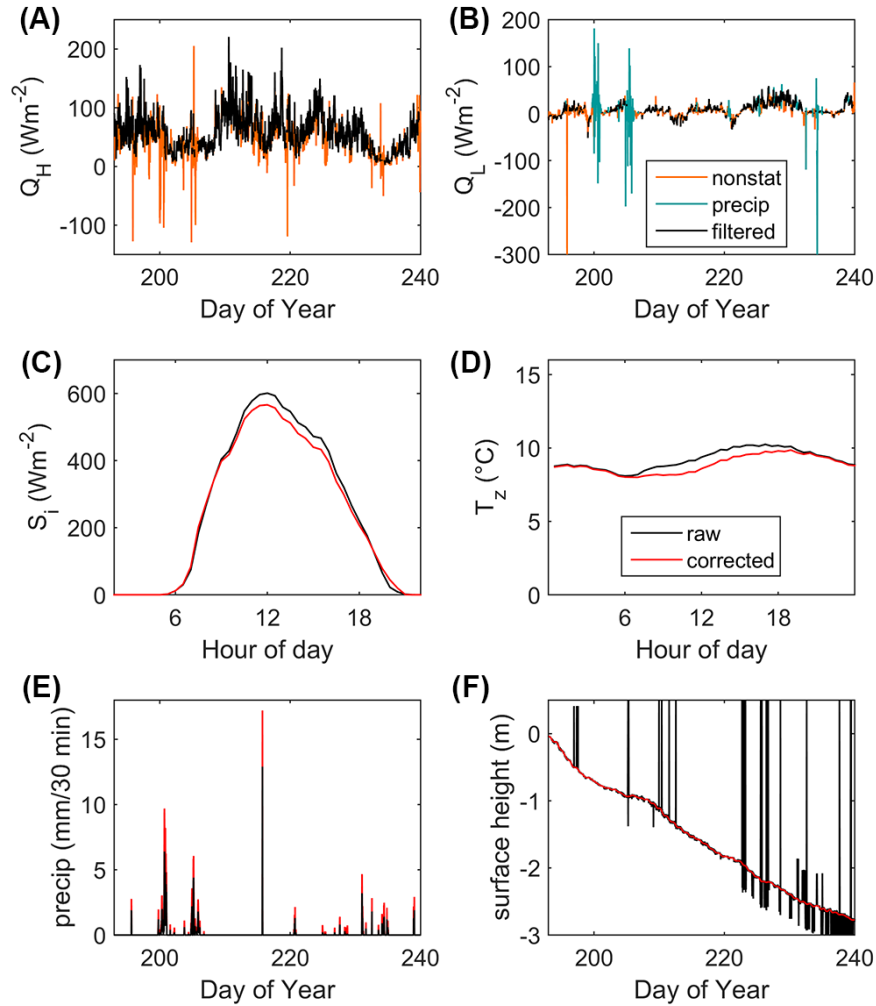


Figure 2.2. (A) Sensible and (B) latent heat fluxes with periods of nonstationary turbulence (orange) identified through the methods of Foken (2008), and periods of precipitation and the subsequent 90 minutes (teal), when the gas analyser windows may have been partially obscured. Also shown are the raw and corrected observation data for (C) the mean daily cycle (over 47 days) of incoming shortwave radiation, (D) the mean daily trend of near-surface air temperature, (E) 30-minute precipitation, and (F) 30-minute surface height.

Radiation Measurements

Observations of S_i are susceptible to errors at high solar zenith angles (Z_s) near sunrise and sunset, due to the poor cosine response of the sensor, particularly if the instrument is not level in the horizontal. In a number of studies (e.g. Andreassen *et al.*, 2008), a 24-hour running mean value for albedo (α) is calculated from the 30-minute S_i and S_r data, and used to generate a new parameterised dataset for S_i . This correction method, however, does not account for sub-daily variations that can occur in α , due to snowfall, snow ageing and removal, changing water content of the surface, and cloud amount. To allow for these variations, the S_i values in this study have only been corrected during periods when the sun is low in the sky. Based on the performance statistics provided by the radiometer manufacturer, a threshold value of $Z_s > 65^\circ$ was selected (Kipp & Zonen, 2009). A daily mean albedo value (α_d) is calculated from the observed S_i and S_r data when $Z_s < 65^\circ$, and used to calculate S_i when $Z_s > 65^\circ$ ($S_i = S_r/\alpha_d$). Observed S_i values are used for the remainder of the time.

When installed, the radiometer was levelled in the horizontal plane. The surface over which it is positioned, however, is sloped at an angle of 8° , and therefore, the intensity of the radiation exchange at this surface will be different from that recorded at the radiometer, and needs to be corrected for (van den Broeke *et al.*, 2004). As L_i , L_o , and S_r are assumed isotropic, only S_i is considered susceptible to this slope effect, and specifically, its direct component (D). As only global radiation (G) is measured by the radiometer (i.e. $S_i = G$), S_i is separated into its direct and diffuse (d) components following the methods of Hock and Holmgren (2005). The diffuse component is assumed to increase with cloudiness, which is estimated using the ratio (x) of S_i to the top of the atmosphere radiation (I_{TOA}):

$$x = \frac{S_i}{I_{TOA}}, \quad (2.6)$$

$$\frac{d}{S_i} = \begin{cases} 0.15 & \text{for } x \geq 0.8 \\ 0.929 + 1.134x - 5.111x^2 + 3.106x^3 & \text{for } 0.15 < x < 0.8 \\ 1 & \text{for } x \leq 0.15 \end{cases} \quad (2.7)$$

Here, the empirical relationships derived in the above study (Equation 2.7) are assumed to be transferable to the Nordic site. A geometric correction is then applied to D , before it is recombined with the diffuse component to determine S_i at the surface (Jonsell *et al.*, 2003):

$$D_s = D \frac{\cos\beta \cos Z_s + \sin\beta \sin Z_s \cos(\Omega - \theta)}{\cos Z_s}, \quad (2.8)$$

where D_s is the direct S_i component at the slope, Ω is the solar azimuth angle, β is the slope angle relative to the radiometer, and θ is the slope azimuth angle. β is updated every 30 minutes to account for any tilting of the radiometer from horizontal, as recorded by the inclinometer ($< 2^\circ$ over the study). The combined effect of the cosine response and slope corrections on the observed S_i (Figure 2.2C) resulted in a mean reduction of 4.1% in the energy of the flux over the season, and a maximum 30-minute reduction of 7% (66.2 W m^{-2}).

The largest possible magnitude of L_o emitted by a melting snow/ice surface (at 273.15 K) is approximately 316 W m^{-2} , and can be calculated using the Stefan-Boltzmann constant, σ ($5.67 \times 10^{-8} \text{ W m}^{-2} \text{ K}^{-4}$):

$$L_o = \varepsilon \sigma T_s^4 + (1 - \varepsilon)L_i, \quad (2.9)$$

where ε is longwave emissivity (0.98), and T_s is the surface temperature (Park *et al.*, 2010). This method accounts for the effect of emissivity and reflected L_i on the L_o value observed by the sensor. The observed L_o dataset was found to regularly exceed these calculated maximums ($+10.1 \text{ W m}^{-2}$ or $+3\%$, on average). This may have been due in part to the sensor receiving additional longwave radiation emitted by the station structure when warmed above 0°C . To correct for this,

observed L_o values in excess of this threshold were lowered to the calculated maximum. An independent surface temperature measurement would be a useful addition to the system in future deployments.

Air Temperature Correction

The air temperature and humidity probe was housed in a naturally ventilated radiation screen, rather than in a mechanically aspirated screen, due to power constraints. As a result, the data may suffer from errors due to radiative heating of the sensor during periods of strong solar radiation (WMO, 1983; Hock and Schroff, 2004; Obleitner, 2004; Fitzpatrick, 2007). To account for this, a correction was implemented using the sonic temperature from the sonic anemometer, which is assumed less susceptible to radiation error. The sonic temperature (T_{sonic}) was converted to air temperature (T_{sa}) using the method of Kaimal and Gaynor (1991):

$$T_{sa} = \frac{T_{sonic}}{\left(1 + 0.32 \frac{e}{p}\right)}, \quad (2.10)$$

where e is vapour pressure, and p is atmospheric pressure. T_{sa} and e were calculated iteratively to account for the initial uncorrected air temperature value used to calculate e . The values of T_{sa} were then compared with the air temperature observations from the sensor in the screen (T_z), during nighttime periods (no solar radiation) with wind speeds above 3 m s^{-1} when the screen is well ventilated (Harrison, 2010), to obtain the mean bias between the sensors (-0.17°C). This bias was removed from T_{sa} to obtain $T_{sa_unbiased}$, which in turn was subtracted from T_z to calculate differences from measured air temperature ($\Delta T = T_z - T_{sa_unbiased}$). The variation of ΔT with S_i was examined, and found to be well represented by a 2nd order polynomial ($\Delta T = -5.5 \times 10^{-7} S_i^2 + 0.0017 S_i - 0.052$; $r^2 = 0.76$). This empirical fit was employed to estimate the

correction required for radiation error in T_z for a given S_i magnitude, resulting in a mean temperature reduction of 0.3°C and a maximum reduction of 1.1°C (Figure 2.2D) for a 30-minute average. Adding wind speed to this regression analysis was tested, but was found not to improve the goodness of fit.

Rainfall Undercatch

Studies on tipping bucket rain gauges have observed extensive underestimation of rainfall amounts (of up to 50%), primarily due to acceleration of airflow over the top of the gauge, with other error sources including splashing, and the finite time required for the buckets to reset in between tips during heavy rain (e.g. Devine and Mekis, 2008; Duchon and Biddle, 2010). An empirical correction was applied to the Nordic data to account for wind effects, following the work on a similar gauge by Mekonnen *et al.* (2015). The correction factor, w_r , accounts for the effects of wind speed at gauge height, u_g , and precipitation intensity, I_p (mm/hr), on the observations:

$$w_r = \frac{1}{1 - \exp\left[\left(0.011 - 0.062 \ln(I_p)\right) u_g - 0.776\right]}, \quad (2.11)$$

where

$$u_g = u \frac{\ln\left(\frac{z_g}{z_{0v}}\right)}{\ln\left(\frac{z_u}{z_{0v}}\right)}, \quad (2.12)$$

and z_g is the height of the rain gauge, which is continuously updated from its initial installed height using the surface height data from the sonic ranger (as the gauge was mounted on a fixed mast rather than the quadpod). Using this correction, the undercatch for the Nordic precipitation data was estimated to be 40.4%, on average (Figure 2.2E).

Surface Height Measurements

Surface height datasets obtained from sonic rangars are characteristically noisy, and require processing prior to use. The raw data were first corrected for the effect of air temperature variation on the speed of sound, following manufacturer guidelines (Campbell Scientific Inc., 2014). A low pass filter was applied to remove a series of unrealistic spikes in surface height change with rates above 0.04 m min^{-1} , and to replace them with values from the previous minute. The surface height values were then passed through a 24-hour moving average filter, chosen to optimise the retrieval of a smooth dataset that still displays sub-diurnal fluctuations (Figure 2.2F).

Rain Heat Flux

Q_R was calculated by first cross-examining the data obtained from the rain gauge with T_z , and determining whether the precipitation was rain or snow, based on a threshold near-surface air temperature (in this case, 1°C). The energy received from rain events in W m^{-2} was then calculated following Hay and Fitzharris (1988):

$$Q_R = \rho_w c_w R (T_r - T_s) , \quad (2.13)$$

where ρ_w is the density of water ($1,000 \text{ kg m}^{-3}$), c_w is the specific heat capacity of water ($4,180 \text{ J kg}^{-1} \text{ K}^{-1}$), R is the rainfall rate, and T_r is the rain temperature which is assumed to be in equilibrium with T_z , and T_s is surface temperature. Apart from one brief period of snowfall on July 24th (DOY 205), all precipitation events during the study were deemed to have been rainfall. The utilised threshold air temperature for the occurrence or absence of snowfall was verified by examining the albedo values and camera images from these periods.

Ground Heat Flux

Q_G is estimated from the ice thermistor data, using the methods outlined in Konzelmann and Braithwaite (1995). Half-hourly flux profiles of the upper layer of the glacier were constructed using the following equation:

$$H(z_{ice}) = -K \frac{\Delta T_i}{\Delta z_{ice}}, \quad (2.14)$$

where $H(z_{ice})$ is the heat flux at the depth of each thermistor (start of season depths for $z_{ice} = 0.25\text{--}4$ m), K is the thermal conductivity of ice ($2.1 \text{ W m}^{-1} \text{ K}^{-1}$), and ΔT_i and Δz_{ice} are the differences in ice temperature and depth between z_{ice} and the surface. The magnitude of Q_G at the surface for each 30-minute period was then estimated by fitting a linear regression to the flux profile, and taking the regressed value for $H(0)$. With no significant sub-daily trends in the observed data, and to allow for the slow response time of the ice thermistors, daily averages for Q_G were used in the SEB equation. The changing depths of the thermistors over the season (z_{ice}) were estimated from the initial depths of their installation and the surface height data from the sonic ranger. Data from thermistors that came within 0.5 m of the surface were excluded, to minimise the influence of radiative heating of the cables.

Error Analysis

Following the above processing and correction steps, the random error in the values for each of the eight fluxes was estimated. Standard error propagation methods were implemented to calculate the uncertainty in Q_R and Q_G from the sensor accuracies (Table 2.1) and uncertainties in the variables in Equations 2.13 and 2.14 (e.g. R , T_s , T_i , z_{ice}). For Q_R , the assumption made in Equation 2.13 that T_r is in equilibrium with T_z may not hold true where strong near-surface gradients in air

temperature exist. Therefore, an assumed uncertainty of $\pm 2^\circ\text{C}$ was assigned to T_r for the error propagation calculations. The random error in the EC-observed turbulent fluxes due to sampling errors was estimated following the methods of Finkelstein and Sims (2001). Where Q_H and Q_L values have been replaced by bulk estimated fluxes due to periods of precipitation or nonstationary turbulence, error propagation has been applied to Equations 2.4 and 2.5. As stated previously, there may be additional unquantified uncertainty here due to the application of the bulk method during nonstationary conditions. Uncertainty values for the shortwave and longwave radiation fluxes, as provided by the sensor manufacturer (Kipp & Zonen, 2009), are listed as being $<5\%$ and $<10\%$, respectively, for daily totals. To refine these values for the measurements in this study, the uncertainty in the shortwave fluxes was estimated from the deviations of the raw S_i and S_o measurements from 0 W m^{-2} at night, and for the longwave fluxes from the deviations of the L_o measurements from the values expected for a melting surface (Litt *et al.*, 2015). The smoothed surface height dataset also contains uncertainty due to the choice of length of moving average filter used. A range of time lengths were tested for the filter window (3–48 hours), and the maximum and minimum height values for each period were used to determine the uncertainty range on the 24-hour filtered data.

2.4.4 SEB Model

In the first stage of the model, the observed energy fluxes are converted into 30-minute averages and summed to obtain averages of Q_M in W m^{-2} (Equation 2.1). The general convention in glacier SEB studies is that fluxes resulting in a gain in energy of the surface have a positive sign. The maximum temperature a snow/ice surface can be warmed to is 0°C . When the glacier surface is at

this temperature, any positive energy available in the Q_M term is used by the model to generate melting (Hock, 2005):

$$M = \frac{Q_M}{\rho_w L_f}, \quad (2.15)$$

where M is the average melt per second (for a given 30-minute average of Q_M) in m of water equivalent (m w.e. s^{-1}), and L_f is the latent heat of fusion (0.334 MJ kg^{-1}). The unit of m w.e. expresses the thickness of the layer melted (per m^2 of area) when the snow/ice is converted to water. The surface temperature of the glacier is estimated in the model using the observed (corrected) longwave radiation data (Equation 2.9). Sublimation (in m w.e. s^{-1}) is also accounted for in the model. A negative/positive value for Q_L (i.e. a loss/gain of latent heat energy) indicates mass loss/gain through sublimation/deposition and can be accounted for as follows:

$$sub/dep = \frac{|Q_L|}{\rho_w L_s}, \quad (2.16)$$

where $|Q_L|$ denotes the absolute value. The values for melt and sublimation, converted from averages to 30-minute totals, are summed together to calculate surface ablation (a). The performance of the SEB model is evaluated by comparing the values it generates with the data observed by the sonic ranger. Modelled ablation is converted into surface height changes (z_{gM}) by multiplying the half hourly ablation totals by the ratio of ρ_w to the snow or ice density ($\rho_{s/i}$):

$$z_{gM} = a \frac{\rho_w}{\rho_{s/i}}. \quad (2.17)$$

A thin layer of packed snow covered the site surface for the first three days of observations, and a constant value of 400 kg m^{-3} was used for ρ_s . For the remaining period, the ice surface was assumed to have a constant density of 900 kg m^{-3} (Arnold *et al.*, 2006; Gillett and Cullen, 2011; Van As, 2011). These surface height values can then be compared directly with the smoothed values from

the sonic ranger. Accumulation due to snowfall and deposition is also added to the modelled surface height, so as to more accurately follow the observed values. During the single, brief period of snowfall (0.001 m w.e. approx.), a density of 80 kg m^{-3} was assumed for the fresh snow; a low density value to account for the thin and incomplete coverage of snowfall over the study site.

2.4.5 Bulk Method Evaluation

The performances of bulk method parameterisations of the turbulent heat fluxes (Equations 2.4 and 2.5) were evaluated through comparisons with the observed fluxes from the EC system. Three of the bulk transfer coefficient forms most commonly used in glacier studies have been tested here. The first form assumes neutral atmospheric stability (excludes a stability function), and a logarithmic wind speed profile (e.g. Conway and Cullen, 2013):

$$C_{log} = \frac{\kappa^2}{\ln\left(\frac{zu}{z_0v}\right)\ln\left(\frac{z}{z_0t/q}\right)}, \quad (2.18)$$

where κ is the von Kármán constant (0.4). The second form includes a function for stability based on the bulk Richardson number, R_{ib} (Webb 1970; Brock *et al.*, 2010):

$$C_{bR} = \frac{\kappa^2}{\ln\left(\frac{zu}{z_0v}\right)\ln\left(\frac{z}{z_0t/q}\right)} \Phi, \quad (2.19)$$

where

$$R_{ib} = \frac{g(T_z - T_s)z}{T_z u^2}, \quad (2.20)$$

$\Phi = (1 - 5R_{ib})^2$ for stable conditions (positive R_{ib}), and $\Phi = (1 - 16R_{ib})^{0.75}$ for unstable conditions (negative R_{ib}), and g is acceleration due to gravity (9.81 ms^{-2}). The third form uses stability functions based on the similarity theory of Monin and Obukhov (1954), and is arguably

the most frequently used stability scheme in glacier SEB models (e.g. Arnold *et al.*, 2006; Giesen *et al.*, 2014):

$$C_{MO} = \frac{\kappa^2}{\left[\ln\left(\frac{z_u}{z_{0v}}\right) - \psi_m\left(\frac{z_u}{L}\right) \right] \left[\ln\left(\frac{z}{z_{0t/q}}\right) - \psi_h\left(\frac{z}{L}\right) \right]}, \quad (2.21)$$

where $\psi_m\left(\frac{z_u}{L}\right)$ and $\psi_h\left(\frac{z}{L}\right)$ are the vertically integrated stability functions for momentum and heat, with the stability function for water vapour, $\psi_e\left(\frac{z}{L}\right)$, assumed equal to $\psi_h\left(\frac{z}{L}\right)$. L is the Obukhov length:

$$L = \frac{\rho_a c_p u_*^3 T_z}{\kappa g Q_H}, \quad (2.22)$$

where u_* is the friction velocity (a function of shear or the vertical flux of horizontal momentum). Conceptually, L can be thought of as the height above the surface where buoyant forces equal shear forces in the production of turbulence (Stull, 1988). As L contains Q_H , an iterative scheme is used when solving Equations 2.4 and 2.22, following Munro (1989). The parameter $\frac{z_u}{L}$ is used to determine stability conditions, with $\frac{z_u}{L} < 0$ implying unstable, $\frac{z_u}{L} > 0$ implying stable, and $\frac{z_u}{L} = 0$ implying neutral. In this study, the functions proposed by Beljaars and Holtslag (1991) have been used in Equation 2.21 for stable conditions:

$$-\psi_m\left(\frac{z_u}{L}\right) = \frac{az_u}{L} + b\left(\frac{z_u}{L} - \frac{c}{d}\right) \exp\left(-\frac{dz_u}{L}\right) + \frac{bc}{d}, \quad (2.23)$$

$$-\psi_h\left(\frac{z}{L}\right) = \left(1 + \frac{2az}{3L}\right)^{1.5} + b\left(\frac{z}{L} - \frac{c}{d}\right) \exp\left(-\frac{dz}{L}\right) + \frac{bc}{d} - 1, \quad (2.24)$$

with $a = 1$, $b = 0.667$, $c = 5$, and $d = 0.35$. For unstable conditions, the methods of Dyer (1974) have been implemented:

$$\psi_m\left(\frac{z_u}{L}\right) = \log\left[\left(\frac{1+y^2}{2}\right)\left(\frac{1+y}{2}\right)^2\right] - 2\tan^{-1}y + \frac{\pi}{2}, \quad (2.25)$$

$$\psi_h\left(\frac{z}{L}\right) = 2 \log\left(\frac{1+y^2}{2}\right), \quad (2.26)$$

where $y = \left(1 - 16\frac{zu}{L}\right)^{\frac{1}{4}}$ for Equation 2.25, and $y = \left(1 - 16\frac{z}{L}\right)^{\frac{1}{4}}$ for Equation 2.26.

Roughness Lengths

The roughness length values for the Nordic Glacier site were calculated from EC-observed data for wind speed, air temperature, specific humidity, friction velocity, Monin-Obukhov length, and the surface layer scales for temperature and specific humidity (u_{ec} , T_{ec} , q_{ec} , u_{*ec} , L_{ec} , θ_{*ec} , and q_{*ec} , respectively) (Conway and Cullen, 2013):

$$z_{0v} = \exp\left[-\kappa \frac{u_{ec}}{u_{*ec}} - \psi_m\left(\frac{z}{L_{ec}}\right)\right] z, \quad (2.27)$$

$$z_{0t} = \exp\left[-\kappa \frac{T_{ec}-T_s}{\theta_{*ec}} - \psi_h\left(\frac{z}{L_{ec}}\right)\right] z, \quad (2.28)$$

$$z_{0q} = \exp\left[-\kappa \frac{q_{ec}-q_s}{q_{*ec}} - \psi_h\left(\frac{z}{L_{ec}}\right)\right] z. \quad (2.29)$$

q_s is determined from the surface vapour pressure (e_s) which is assumed to be at saturation at T_s ($q_s = 0.622 e_s/p$). A series of filters were applied to the 30-minute data to identify periods optimal for calculating accurate roughness length values, representative of conditions on the glacier, and with minimum scatter. Wind direction is an important filter, and data were used when the wind was blowing from within a 90° window around the main axis of the EC sensor (which pointed to 225°), to minimise flow distortion due to air flow through the station structure. Minimum values for wind speed (3 m s^{-1}) and u_{*ec} (0.1 m s^{-1}) were also implemented to avoid large errors in z_{0v} . As previously described, precipitation can affect the data observed from the gas analyser. Measurements of u_{*ec} also displayed spiking during rainfall, and so periods of

precipitation were excluded from roughness length calculations. Sufficient near surface gradients in temperature and vapour pressure are necessary to determine z_{0t} and z_{0q} . Therefore, filters for minimum differences in measurement and surface height values of air temperature ($>1^\circ\text{C}$) and vapour pressure ($>66\text{ Pa}$) were applied (Calanca, 2001; Conway and Cullen, 2013). The mean free path length for molecules at the average pressure and temperature at the station was calculated to be approximately $1 \times 10^{-7}\text{ m}$, and this value was used as a minimum physically plausible value for scalar roughness lengths (Li *et al.*, 2016). As was carried out during pre-processing of the EC fluxes, turbulence for each 30-minute period had to pass a test of stationarity (Foken, 2008) to be used for roughness length calculation. Due to the uncertainty regarding how valid the applied stability functions are for a glacier surface, a filter to only use data from near-neutral stability conditions ($-0.1 < \frac{z}{L_{ec}} < 0.2$), when these functions are negligible, has been applied (Smeets and van den Broeke, 2008; Conway and Cullen, 2013).

In addition to implementing the EC-derived roughness values calculated above, the bulk transfer coefficients were also evaluated using a number of the most commonly used ‘assumed’ roughness length schemes from previous glacier studies, where site-specific measurements of roughness length are generally unavailable. Two sets of values for z_{0t} and z_{0q} were estimated by assuming both an equal and a 1/100 relation to z_{0v} , where z_{0v} is assumed to be 10^{-3} m for ice, and 10^{-4} m for snow (Mölg and Hardy, 2004; Hock and Holmgren, 2005). A third set of values for z_{0t} and z_{0q} was calculated using these assumed z_{0v} values and the surface renewal theory methods outlined by Andreas (1987), where the ratio of the scalar (z_{0s}) and momentum roughness lengths are expressed as a function of the roughness Reynolds number R_* :

$$R_* = \frac{u_* z_{0v}}{\nu}, \quad (2.30)$$

$$\ln(z_{0s}/z_{0v}) = b_0 + b_1 \ln(R_*) + b_2 \ln(R_*)^2, \quad (2.31)$$

where ν is the kinematic viscosity of air ($1.5 \times 10^{-5} \text{ m}^2 \text{ s}^{-1}$). The values of the empirical coefficients (b_0 , b_1 , and b_2) change for smooth ($R_* \leq 0.135$), transitional ($0.135 < R_* < 2.5$), and rough ($R_* \geq 2.5$) flow regimes. For infilling the gaps in the EC-observed flux data due to precipitation and nonstationary turbulence (Section 2.4.3), an additional set of effective roughness length values were also calculated, which were tuned to return the observed turbulent flux values when implemented with C_{log} . Daily averages of these roughness values were used in Equation 2.18 to estimate the missing flux data.

2.5 Results

2.5.1 Meteorological and Flux Observations

The meteorological conditions remained mild throughout the study period (Figure 2.3), with a mean T_z of 8.9°C and consistently positive air temperatures (max: 16.1°C; min: 0.6°C). Cloud coverage was generally low, as verified by camera imagery, resulting in high net shortwave radiation fluxes over the season (mean: 130.6 W m⁻²) and low net longwave values (mean: -9.2 W m⁻²). The surface temperature T_s , was estimated to be at melting point for > 99% of the study period, with the temperature below 0°C for a total of 5 hours (min: -0.3°C). Precipitation was confined to three frontal systems and sporadic convective showers (total: 293.7 mm), with a trace amount of snowfall on July 24th (DOY 205). The mean Q_R value was 1.7 W m⁻² over the entire period, with a maximum 30-minute average of 339.2 W m⁻² during an individual event with a 34 mm/h rainfall rate (DOY 215). Winds were generally light and steady, with a mean of 3.5 m s⁻¹ and a maximum 30-minute average of 7.2 m s⁻¹. The mean wind direction was 204°, which

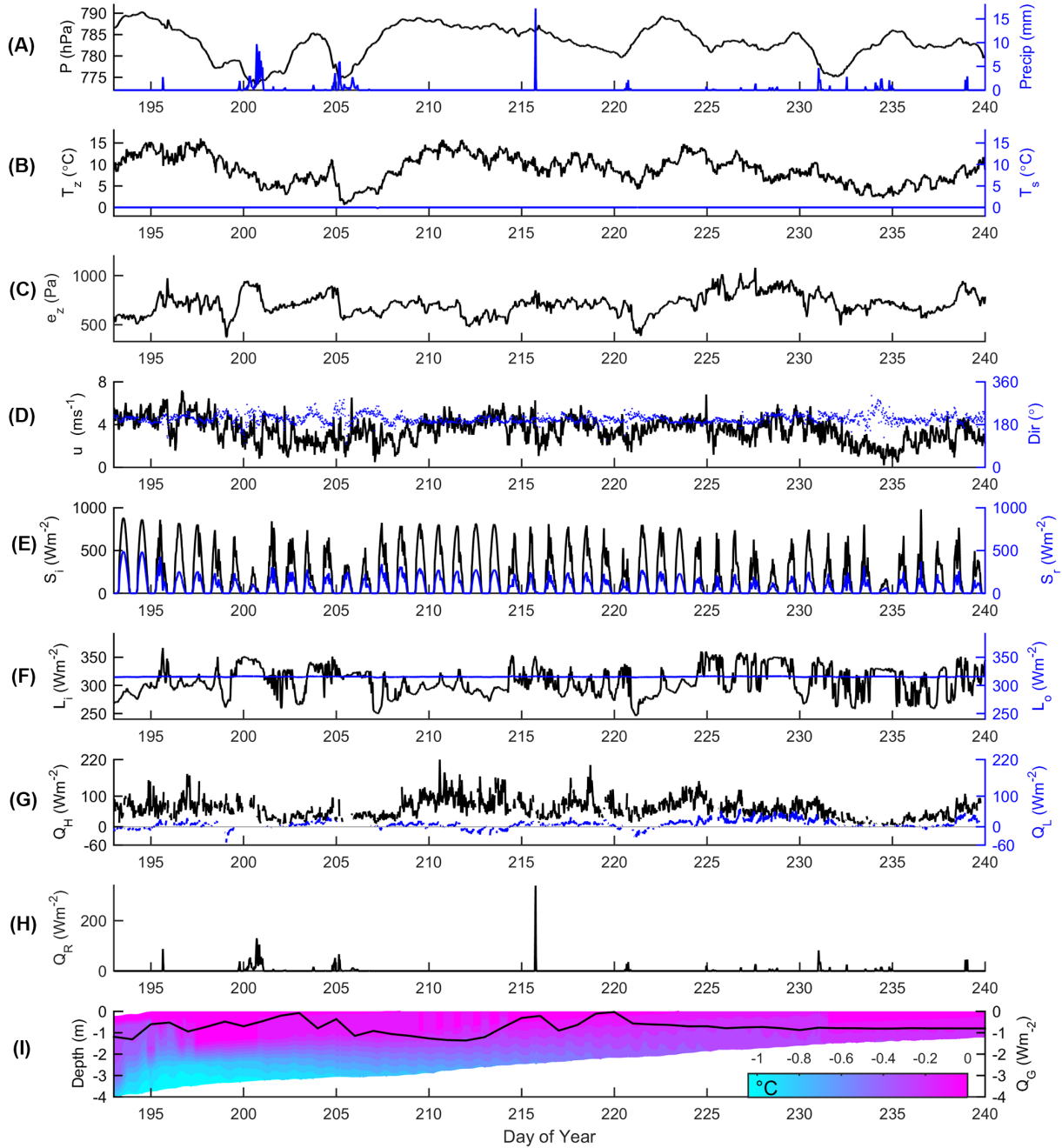


Figure 2.3. 30-minute meteorological data and surface energy fluxes for July 12th – August 28th (DOY 193 – 240) 2014 on Nordic Glacier; (A) pressure and precipitation, (B) 2 m air and surface temperature, (C) 2 m vapour pressure, (D) wind speed and direction, (E) incoming and reflected shortwave, (F) incoming and outgoing longwave, (G) sensible and latent heat fluxes, (H) rain heat flux, and (I) ice temperature profile and ground heat flux.

accords with the downslope air flow on the glacier. The wind remained within $\pm 45^\circ$ of this direction for 91% of the observation period, and within $\pm 90^\circ$ for 97% of the period, with no evident diurnal cycle. The positioning of the EC sensor within the prevailing wind window (main axis: 225°) ensured that, for the vast majority of observations, air flow was sampled by the EC system prior to being distorted by the station. Q_H remained positive for the entire observation period, with a mean value of 59.4 W m^{-2} . Q_L fluctuated about zero, with a mean value of 9.0 W m^{-2} . The ice thermistors recorded a small temperature gradient in the near-surface ice layer ($\sim 0.9^\circ\text{C}$ over 4 m). As the thermistor cables gradually melted out over the season, the depth range of ice temperature measurements reduced. From the available data, little change is observed in the temperature profile over time, with a slight warming trend commencing a few days after the removal of the snow layer (DOY 196). With such a small temperature gradient, Q_G remained small, with a mean value of -0.7 W m^{-2} .

Error analysis performed on each of the observed fluxes returned daily average error values substantially smaller than the fluxes themselves (Table 2.2). The obtained mean uncertainties for shortwave and longwave fluxes of 1.9% and 3.3% are in line with those estimated in previous studies using similar sensors (e.g. Van den Broeke, 2004). It should be noted that there remains unquantified uncertainty in S_i and Q_R due to the previously described empirical corrections applied to the data. The combined effect of the errors in each flux were propagated to obtain the error in Q_M (mean relative error: $\pm 9.9\%$). The uncertainty in the surface height data due to the required smoothing was calculated to be $\pm 0.001 \text{ m}$ ($\pm 71.4\%$) and $\pm 0.008 \text{ m}$ ($\pm 13.8\%$) for mean 30-minute and daily values, respectively.

Table 2.2. Range of daily average error values (% of mean fluxes) calculated for the observed fluxes and Q_M .

	δS_i	δS_r	δL_i	δL_o	δQ_H	δQ_L	δQ_G	δQ_R	δQ_M
Mean (%)	±1.9	±1.9	±3.3	±3.3	±2.2	±0.6	±27.0	±35.8	±9.9
Max (%)	±3.2	±4.9	±3.7	±3.3	±5.6	±2.4	±54.1	±81.1	±27.2
Min (%)	±0.4	±0.4	±2.9	±3.3	±0.4	±0.1	±13.5	±16.6	±5.8

2.5.2 Ablation Modelling and Surface Energy Balance Partitioning

The ablation values obtained from the SEB model show good agreement with those recorded by the sonic ranger (Figure 2.4). Both modelled and observed data returned a net surface ablation of 2.74 m over the 47 days. Examining model performance in estimating 30-minute changes in surface height, the model showed a correlation (r) of 0.75 with the ranger data, and a root-mean-square error (RMSE) of 0.001m/30 min. On a daily time scale, model performance was considerably improved (r : 0.86; RMSE: 0.02m/day). Net radiation (Q_N) was the largest contributor to the melt energy, providing 65.2% over the study period (Figure 2.5A), with the longwave fluxes effecting a net loss of energy from the surface (-7.6% of Q_N), as shown in Figure 2.5B. Q_H was the second largest contributor with 29.7%, followed by Q_L with 4.5%. Due to the low magnitude and frequency of negative Q_L fluxes, little sublimation was observed during the season (0.1% of total ablation), while total deposition (during positive Q_L periods) was estimated at 0.014 m w.e. Providing just 0.9% of the total melt energy, Q_R was observed to be the smallest positive contributor over the season, while Q_G was found to be a small surface energy sink (-0.4%). The day with the greatest observed ablation (in terms of m w.e) was July 29th (DOY 210), with 0.1 m w.e. of loss. This corresponds with the day of maximum net energy received at the surface, with a mean flux value of 288.8 W m⁻² observed (55% above the average daily value for the study).

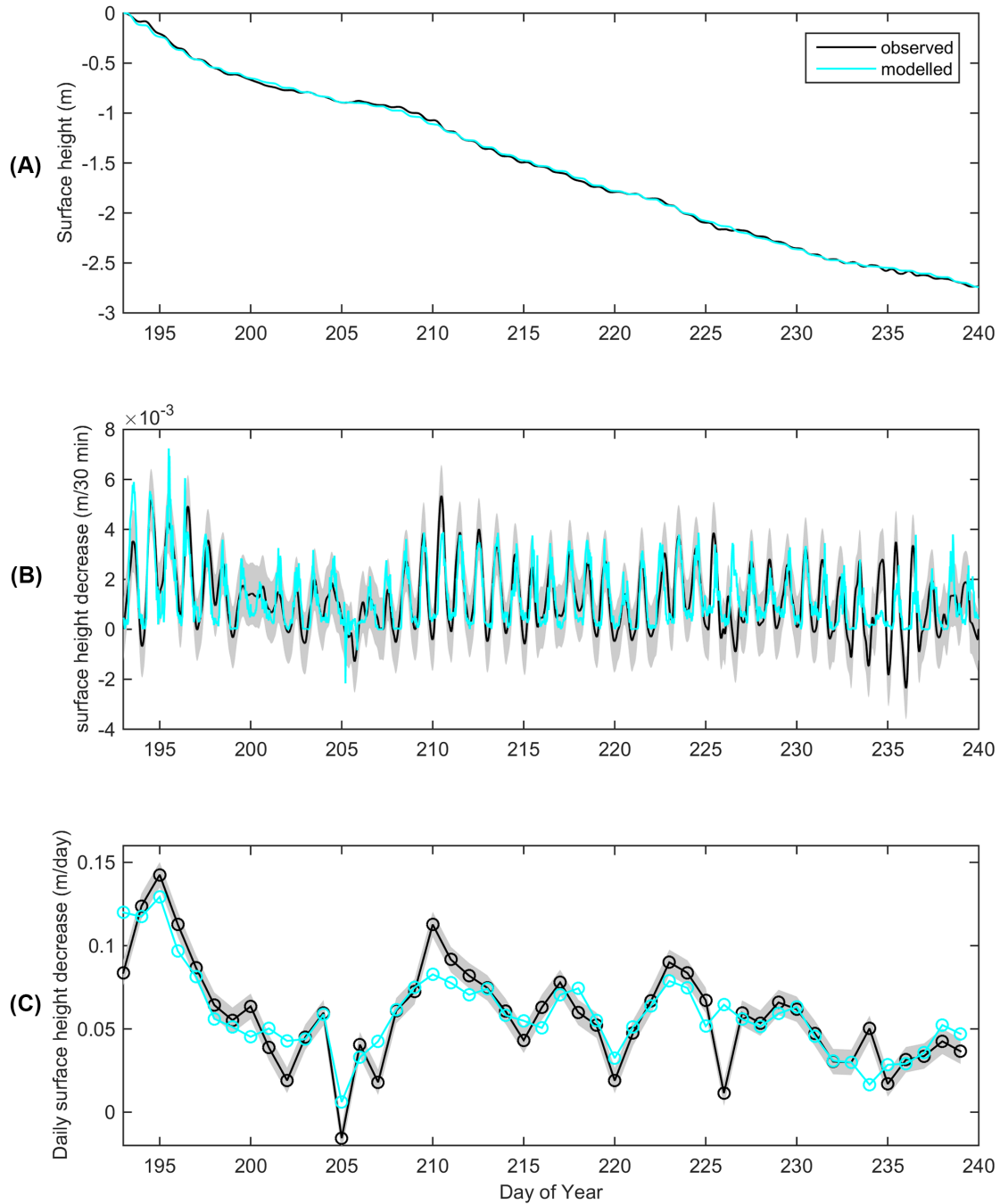


Figure 2.4. Observed (black) and modelled (cyan) surface height changes due to ablation/accumulation on Nordic Glacier, summer 2014; (A) surface height trend over the season, (B) 30-minute rate of surface height change, and (C) daily rate of surface height change (midnight to midnight). The grey shading represents the uncertainty in the observed surface height values arising from the choice of moving average filter length when processing the sonic ranger data.

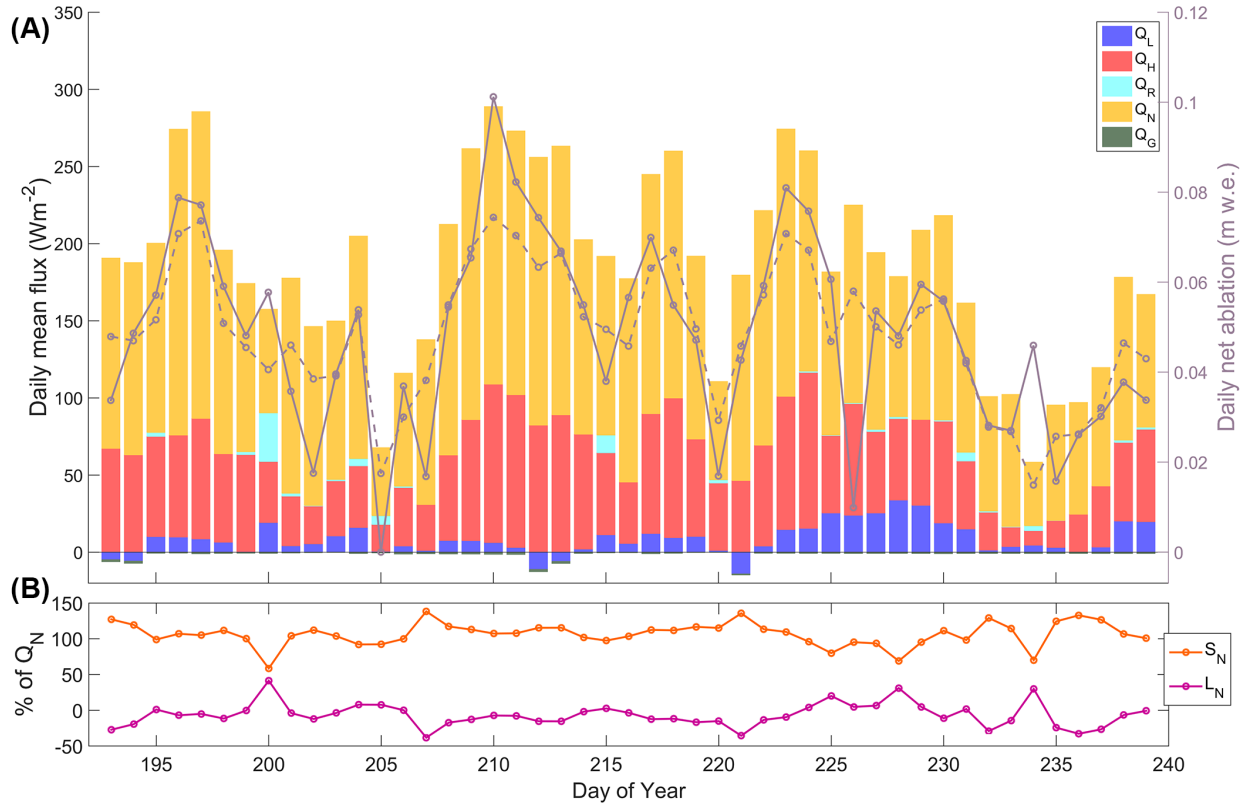


Figure 2.5. (A) Daily mean energy fluxes, and the daily net observed and modelled ablation (solid and dashed grey lines, respectively), and (B) percentage contribution of net shortwave (S_n) and longwave (L_n) radiation to daily Q_N .

2.5.3 Roughness Length Values

As previously described (Equations 2.27–2.29), the EC data obtained on Nordic Glacier were used to calculate a dataset of site-specific roughness length values (ec_z). Atmospheric conditions were predominately stable over the glacier (89% of study, as determined by $\frac{z}{L_{ec}}$) with few periods of neutral stability. As a result, application of the stability filter (along with the other filters described in Section 2.4.5) returned 69, 56, and 11 30-minute periods for z_{0v} , z_{0t} and z_{0q} , respectively, when the values were deemed representative of the study surface. The mean log values of the roughness

lengths (\pm one standard deviation) for these periods were $10^{-2.3 \pm 0.9}$ m, $10^{-4.6 \pm 1.1}$ m, and $10^{-6.0 \pm 0.8}$ m, respectively. In Figure 2.6, the ec_z values are compared with those estimated from the most commonly used roughness length schemes from existing glacier SEB studies: ‘equal’ ($z_{0v} = z_{0t} = z_{0q}$); ‘1/100’ ($z_{0v}/100 = z_{0t} = z_{0q}$); the Andreas (1987) surface renewal method for z_{0t} (mean: $10^{-3.4}$ m) and z_{0q} (mean: $10^{-3.2}$ m). For each of these three methods, z_{0v} is assumed to be 10^{-3} m for ice and 10^{-4} m for snow cover (as discussed in Section 2.4.5). Based on camera and albedo observations, the surface was assumed to transition from snow-covered to ice-covered after the first four days (DOY 197). Separating the EC-derived z_{0v} values into periods with a snow or ice surface produced mean values of $10^{-3.8 \pm 1.7}$ m and $10^{-2.2 \pm 0.7}$ m, respectively.

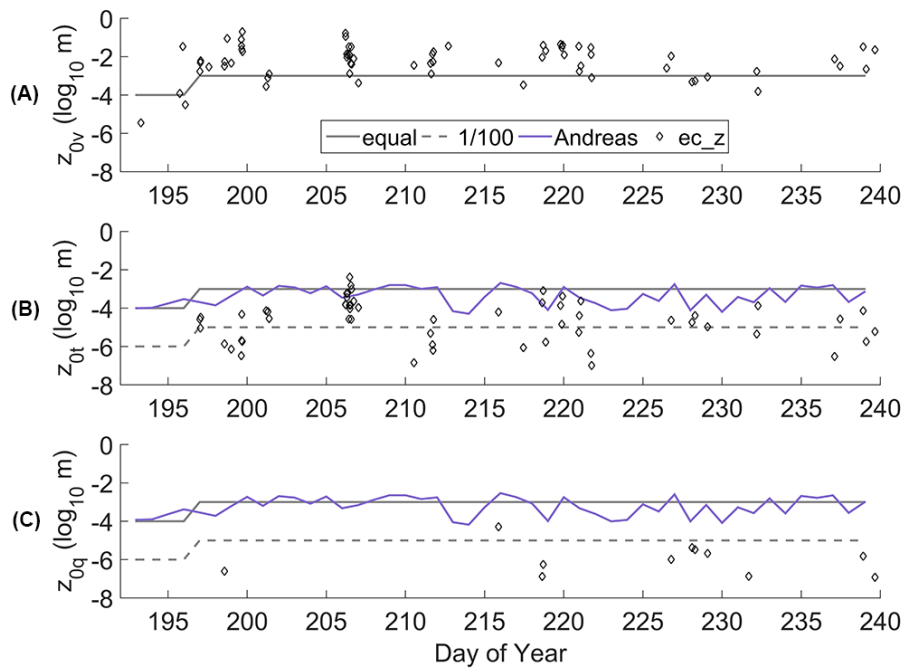


Figure 2.6. 30-minute EC-derived roughness length values for (A) momentum, (B) temperature, and (C) water vapour, compared with commonly assumed roughness length schemes from the literature. For the assumed schemes, z_{0v} is 10^{-3} m for ice, and 10^{-4} m for snow (surface of the turbulence footprint area transitioned from snow to ice on DOY 197).

2.5.4 Bulk Method Evaluation

Three forms of the bulk transfer coefficient (Equations 2.18–2.26), and the previously discussed range of observed and assumed roughness length values, were implemented to obtain 12 sets of bulk-estimated turbulent heat fluxes (see Table 2.3 and Figure 2.7). Where the ec_z data were used, the means of the available roughness length values were implemented (separating z_{0v} for snow and ice). Evaluating the bulk estimates of the fluxes against the EC observations was only carried out for periods with ideal EC measurement conditions, namely those that passed the filters used when calculating the roughness lengths (Section 2.4.5), excluding the stability filter. Therefore, 691 and 380 periods (31% and 17% of study period) were useable for Q_H and Q_L comparisons, respectively. The flux values returned by each bulk method varied greatly depending on the paired roughness scheme. For the ec_z values, C_{log} and C_{MO} show significant correlation with the EC-observed fluxes, in particular, for Q_L ($r = 0.89$, $p < 0.01$). Weaker correlation exists between C_{bR} and the observed fluxes, particularly for Q_H , in addition to substantial underestimation of Q_H and Q_L (MBE: -29.1% and -25.5%). Conversely, C_{log} and C_{MO} , substantially overestimate both fluxes. For the range of assumed roughness schemes, C_{log} , when coupled with the 1/100 roughness scheme, produces flux values closest to those observed.

2.6 Discussion

2.6.1 Energy Balance Observation and Closure

The strong performance of the model in replicating the recorded ablation rates gives a high level of confidence in the successful capture and closure of the SEB by the employed observation and correction methods. The trend of the modelled surface height over the 47 days (Figure 2.4A)

Table 2.3. Performance of the tested bulk methods in modelling the EC-observed turbulent heat fluxes.

z ₀ method	Q _H								
	C _{log}			C _{MO}			C _{bR}		
	r	RMSE(W m ⁻²)	MBE(%)	r	RMSE(W m ⁻²)	MBE(%)	r	RMSE(W m ⁻²)	MBE(%)
ec_z	0.62	33.7	35.8	0.6	32.3	31.9	0.37	37.3	-29.1
equal	0.67	43.4	51.1	0.57	29.0	21.5	0.44	34.8	-20.9
1/100	0.68	23.4	-5.2	0.65	25.8	-11.6	0.44	48.2	-50.3
Andreas	0.68	24.6	17.2	0.64	23.4	3.3	0.43	42.4	-39.2

z ₀ method	Q _L								
	C _{log}			C _{MO}			C _{bR}		
	r	RMSE(W m ⁻²)	MBE(%)	r	RMSE(W m ⁻²)	MBE(%)	r	RMSE(W m ⁻²)	MBE(%)
ec_z	0.89	7.8	47.9	0.89	7.6	44.8	0.78	8.8	-25.5
equal	0.88	18.6	111.5	0.85	13.2	67.7	0.77	7.9	7.4
1/100	0.89	6.1	32.2	0.88	5.6	22.8	0.77	9.7	-32.8
Andreas	0.89	10.5	65.8	0.88	8.3	45.7	0.78	8.0	-16.6

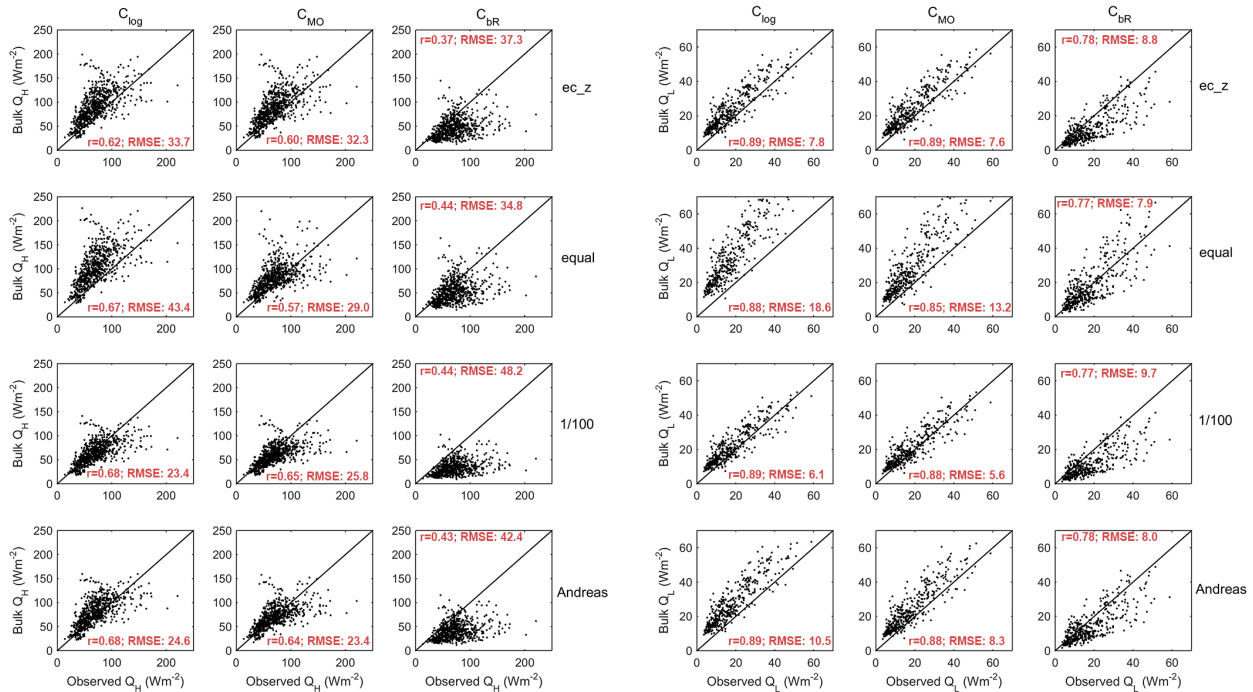


Figure 2.7. Performance of the tested bulk methods in modelling the EC-observed turbulent fluxes of sensible and latent heat.

shows no systematic bias to under or over-estimate when compared with the observed values, resulting in matching net values at the end of the study (-2.74 m). While good performance is also noted in the daily and 30-minute ablation estimates, there are a number of pronounced periods where modelled values substantially differ from observations. Examining the daily timescale (Figure 2.4C), the days with the largest model differences are DOY 193 (+0.036 m), DOY 210 (-0.03 m), DOY 226 (+0.053 m), and DOY 234 (-0.034 m). In most cases, however, these differences can be attributed to observation error. Accidental compression of the snow underneath the sonic ranger during installation prior to DOY 193 resulted in a higher snow density and smaller observed height changes, while a review of camera imagery detected a clear tilting of the sonic ranger mast on both DOY 226 and 234, with the mast tilting forward and upslope on DOY 226 (sensor closer to the surface) and backward and downslope on DOY 234 (sensor further from the surface). DOY 210 was the day with the largest observed ablation and mean surface energy flux (288.8 W m^{-2}), but recorded 30% more ablation than DOY 197, which received just 1% less energy (285.5 W m^{-2}). Camera footage from DOY 210 may indicate the enhancement of a small meltwater stream within the footprint of the sonic ranger, which may have increased mass removal during this period, but the camera angle prevents definitive confirmation of this. Evaluating the SEB model performance with confirmed ranger error days removed (DOY 193, 226, 234) results in a marked improvement with $r: 0.95$ and $\text{RMSE}: 0.01 \text{ m/day}$.

The SEB model offers good performance at 30-minute resolution ($r: 0.78$; $\text{RMSE}: 0.001 \text{ m/30 min}$, with aforementioned error days removed). The most prominent anomaly in the comparison between observed and modelled data at this timescale is the increase in surface height frequently observed by the ranger during night hours (negative values in Figure 2.4B). With only one period of trace snowfall during the study, accumulation does not account for these increases

(mean increase of 0.003 m/night). A possible explanation for this behaviour is the settling of the ranger mast into the warm surface ice, a signal that only becomes visible in the height data in the evening when surface ablation is reduced. With reduced heat and meltwater input into the borehole as the night progresses, this process slows, and at dawn, its signal is once again masked by ablation. This may also explain why the anomaly appears to be strongest in the later stages of the season (maximum increase of 0.03 m/night), when the base of the mast is closer to the surface, and more exposed to surface heat and under greater tilt leverage. An array of sonic rangers around the observation site would be a useful addition to future studies by providing additional data sources when sensor tilting or noise are obscuring the surface height signal from one. It would also help to constrain the likely range of ablation values at the glacier site where substantial variation in ablation can exist over small spatial scales.

In general, the partitioning of the observed SEB is in line with the values determined in existing studies on other mid-latitude glaciers (e.g. Greuell and Smeets, 2001; Hock and Holmgren, 1996). Q_N dominated melt energy, with its magnitude and variability primarily influenced by the net shortwave radiation (S_N), as shown in Figure 2.5B. Low cloud amount (reduced L_i fluxes) and a steadily melting surface (large magnitude L_o fluxes) resulted in a negative net longwave radiation flux (L_N), on average. The relatively large energy contribution provided by Q_H was maintained by the strong and consistently positive temperature gradients between the air and surface, and persistent downslope winds. Q_R provided a negligible contribution (<1%) to the total melt energy over the recorded period. However, over daily and sub-daily timescales, Q_R was observed to have a considerable influence on SEB and ablation during heavy rainfall. On July 19th (DOY 200), persistent heavy rain (daily total: 109.8 mm) resulted in a relatively large Q_R contribution of 20.1% to the daily energy flux (Figure 2.5A). There are previously mentioned uncertainties in the Q_R

values arising from the observed rainfall rates, and the assumption made in Equation 2.13 that drop temperature is in equilibrium with air temperature. However, the general findings from this study show that, on daily and sub-daily timescales, Q_R has the potential to be a significant flux during extreme rain events; a phenomenon projected to become more frequent in a warmer climate (IPCC, 2013). Despite extensive cloud cover on DOY 200, daily ablation (0.058 m w.e.) was above the seasonal average (0.049 m w.e./day), with the non-radiative fluxes dominating Q_M (57.6%), highlighting the importance of accurate observation or estimation of non-radiative fluxes on glaciers (e.g. Fausto *et al.*, 2016).

2.6.2 Bulk Method Evaluation

The initial step in evaluating the bulk method and its uncertainties was to compare roughness lengths calculated from the observed EC data with those commonly assumed for glacier surfaces. Despite extensive filtering, the scatter of the EC-derived roughness values was large over time (Figure 2.6) due to a dependence on a range of mean and turbulent variables in their calculation, as noted in previous studies (e.g. Andreas *et al.*, 2010). The mean z_{0v} value from *ec_z* over the first 4 day period ($10^{-3.8}$ m) was found to be 1.6 orders of magnitude smaller than for the remaining 41 days ($10^{-2.2}$ m). The area upwind from the station (i.e. turbulent flux footprint area) was predominately snow covered during this initial period, and may have presented a smoother surface to the flow than the subsequent ice surface. This observed value for snow is similar to the assumed z_{0v} of 10^{-4} m, but there is close to an order of magnitude difference between the observed and assumed (10^{-3} m) values for the ice surface. A z_{0v} value of $10^{-2.2}$ m is in the upper range of existing observations on glacier ice (Brock *et al.*, 2006), and in line with measurements over rough, heavily gullied ice surfaces (e.g. Smeets *et al.*, 1999). This relatively large roughness value may indicate

the influence of the meltwater-enhanced channel network observed to develop on the surface of Nordic Glacier during the study.

Rather than being equal to z_{0v} , the observed scalar roughness lengths were found to be several orders of magnitude smaller, as has been noted in previous studies (e.g. Beljaars and Holtslag, 1991; Smeets *et al.*, 1998). The assumption that the scalar values are equal to each other was not observed at this site, with mean z_{0q} ($10^{-6.0 \pm 0.8}$ m) 1.4 orders of magnitude smaller than mean z_{0t} ($10^{-4.6 \pm 1.1}$ m). However, only 11 data points were available for z_{0q} after filtering, and there was substantial variability and overlapping of both sets of scalar values (Figure 2.8A). Substituting the *ec_z* values for z_{0v} into the tested roughness length schemes, the equal method overestimates both of the scalar roughness lengths, in some cases, by up to 4 orders of magnitude. The 1/100 method gives a reasonable mean value for z_{0t} while overestimating z_{0q} . The observed data for z_{0t}/z_{0v} show general agreement with the curve of the Andreas (1987) model (Figure 2.8B), but with a tendency for z_{0t} to be underestimated by the model (mean: $10^{-5.3}$ m). The Andreas model was developed over snow and sea ice, which normally present a smoother surface to the flow than glacier ice. Smeets and van den Broeke (2008) proposed an adaption to this model for rougher ice surfaces ($z_{0v} > 10^{-3}$ m). This scheme was also applied to the observed z_{0v} data, resulting in a calculated mean scalar roughness length value of $10^{-3.2}$ m. Therefore, the observed z_{0t} values for this study lie mostly between both schemes. z_{0q} is overestimated by both methods, but shows best agreement with the Andreas model, with a modelled mean value of $10^{-4.9}$ m (Figure 2.8C). Relations between mean meteorological variables (e.g. air temperature, relative humidity) and the scalar roughness lengths have been proposed in previous studies (e.g. Calanca, 2001; Park *et al.*, 2010). However, such relationships were not evident in this dataset. For the roughness results

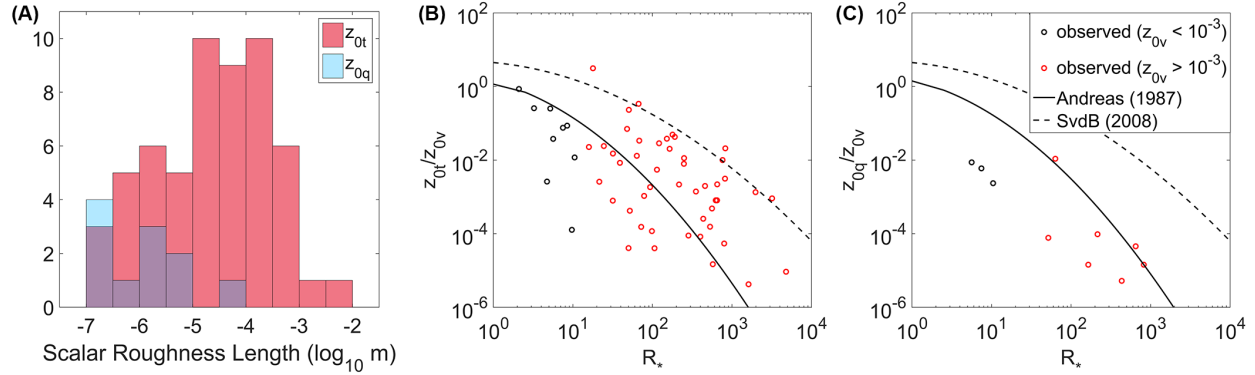


Figure 2.8. (A) Distribution of the EC-derived scalar roughness length values (overlapping regions in purple), and the relationships between the roughness Reynolds number and the (B) z_{0t}/z_{0v} and (C) z_{0q}/z_{0v} ratios, as proposed by Andreas (1987), and Smeets and van den Broeke (SvdB) (2008), and as observed in this study (during near-neutral conditions).

in general, the limited number of data points available for analysis due to the persistent stable atmospheric conditions makes it difficult to draw definitive conclusions. An expanded study over more than one location, and with a greater number of measurements during neutral conditions, would be beneficial.

Assuming the ec_z values to be representative of the glacier surface, applying these roughness lengths to the three tested bulk transfer coefficients allows for an assessment of the performance of each stability scheme in returning flux values similar to those observed (Table 3). With no stability functions, C_{log} does not account for the suppression of turbulence that would theoretically be expected in the predominately stable surface layer at the site. The iterative scheme used to determine L for the C_{MO} method (Equation 2.22) was found to overestimate when compared with EC-derived values of L_{ec} (Figure 2.9B). As a result, stability is underestimated, and the suppression applied by the stability functions is insufficient. Similar overestimation of L has been

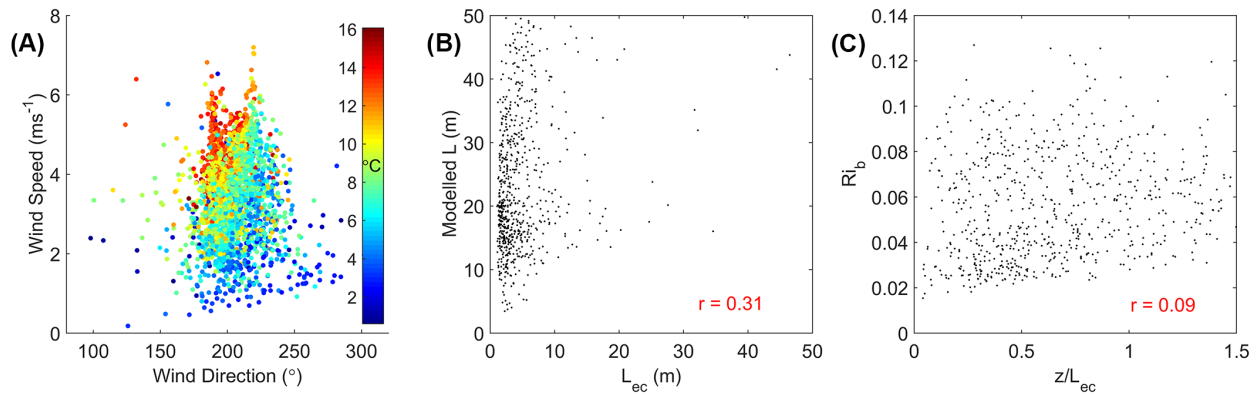


Figure 2.9. (A) Relationship between observed 30-minute wind direction, wind speed, and 2 m air temperature, (B) observed vs modelled Obukhov length values, and (C) observed stability parameter values vs the calculated bulk Richardson number. Only values from periods with ‘ideal’ EC conditions are shown.

observed in a recent comparison on a glacier surface by Radić *et al.* (2017). For daily mean fluxes (with only ideal EC measurement periods included), the performance of C_{MO} is significantly improved, with correlation values for Q_H and Q_L of 0.88 and 0.95, respectively (Figure 2.10). As mentioned, there was substantial observed variability around the mean ec_z values used in the bulk calculations. To test the sensitivity of the modelled fluxes to this variability, Monte Carlo analysis was applied to the utilised roughness lengths. For each 30-minute C_{MO} flux calculation, 10,000 runs were performed where each of the three roughness lengths were selected at random from normally distributed populations with the means and standard deviations of the corresponding ec_z values. The standard deviation of the daily means from these runs are presented as error bars on the modelled flux values in Figure 2.10. Allowing for this sensitivity to roughness length input, periods of flux overestimation remain, being most pronounced during days with combined conditions of strong stability, large near-surface air temperature gradients, and

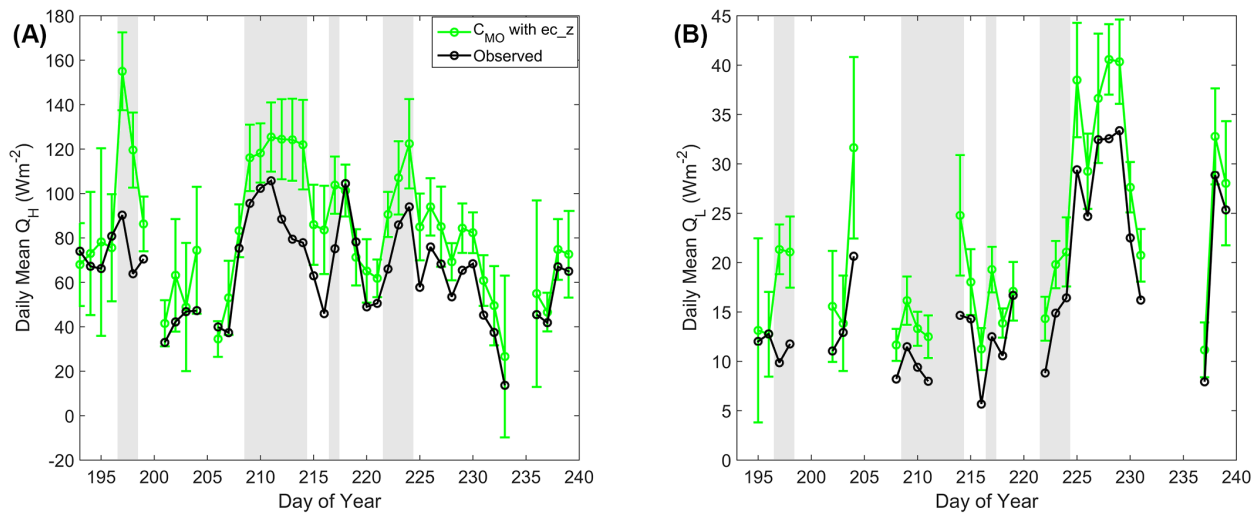


Figure 2.10. Daily means of observed turbulent heat fluxes (black) and C_{MO} modelled fluxes using ec_z roughness lengths (green), for (A) Q_H , and (B) Q_L . Periods with suspected low-level katabatic wind maximums are shaded grey. Daily means only include the 30-minute periods which pass the filters for ideal EC measurement conditions. Error bars on the modelled fluxes represent the standard deviation of the daily means from the Monte Carlo sensitivity analysis.

relatively strong downslope winds, indicative of katabatic flow. Throughout the study period, the strengthening of the near-surface temperature gradient was observed to correspond with a strengthening of the downslope airflow that dominated the observed wind direction (Figure 2.9A). The possible development during very stable conditions of a low-level wind maximum near measurement height may have decoupled turbulence generation from the surface, and invalidated the assumptions of Monin-Obukhov similarity theory, such as a constant flux layer related to near surface gradients (Van der Avoird and Duynkerke, 1999; Denby and Greuell, 2000; Grisogono and Oerlemans, 2001; Parmhed *et al.*, 2004).

As the majority of studies on glaciers do not have access to direct observations of turbulence or roughness lengths, the performances of the bulk methods were also evaluated using

existing assumed roughness values and schemes. As noted, the combination of C_{log} and the 1/100 roughness scheme provides the best performing assumed bulk method. C_{log} may have been expected to overestimate the fluxes in the predominately stable atmospheric conditions during the study. However, implementing a roughness scheme with a mean z_{0v} substantially smaller than the actual value determined for the surface reduces the magnitude of the fluxes calculated by this method. The small underestimation of Q_H can be attributed to implementing a slightly smaller mean z_{0t} than was observed, and conversely for Q_L , with a slightly larger mean z_{0q} . C_{BR} displays the poorest performance of all bulk methods; its stability function excessively suppressing both fluxes, and yielding low correlation values, particularly for Q_H . Q_L is well modelled by C_{BR} when coupled with the equal roughness scheme; the excessive suppression being balanced by a large z_{0q} value. While showing general agreement that conditions were predominately stable (Figure 2.9C), the bulk Richardson number (mean = 0.06 ± 0.02) does not correlate with the observed stability parameter $\frac{z}{L_{ec}}$ from the EC data ($r = 0.09$). C_{MO} returns better performance than C_{BR} . Q_H is relatively well modelled when coupled with the Andreas roughness model; the small assumed z_{0v} compensated by an overestimated z_{0t} , and insufficient turbulence suppression by C_{MO} . A similar situation using the 1/100 method results in a well modelled Q_L by C_{MO} .

2.6.3 Effect of Parameterisation on SEB Closure

The implementation of direct observations for all eight fluxes in the melt model returned results that effectively closed the SEB of the study site. However, as complete flux observations on glacier surfaces are rarely available, the effects of simplifying and parameterising aspects of the SEB are also considered. Some of the most basic assumptions and values used in SEB studies, namely,

negligible Q_R and Q_G , and constant T_s (0°C) and L_o (315.6 W m^{-2} , with unity emissivity), were applied to the model, and found to have little effect on performance when applied individually or in combination ($r = 0.94$; $\text{RMSE} = 0.01 \text{ m/day}$, for daily surface height change). This result is specific to this field study, and may differ significantly if applied to sites other than continental, temperate glaciers. It should also be noted that due to the discussed adjustments made to the L_o data, the assumption of constant T_s has already been partially applied to the original SEB model. The impact of parameterising the turbulent heat fluxes was also assessed, and the choice of bulk method used was found to have a major influence on closure performance. Figure 2.11A displays the daily deviation from Q_M (obtained through the fully observed SEB) for simplified SEB models with a range of previously discussed bulk methods implemented (in addition to the basic assumptions above). The returned daily model values can vary by $\pm 40\%$, depending on the scheme utilised, resulting in differences of up to $\pm 0.5 \text{ m}$ from the sonic ranger observed (or full SEB modelled) cumulative surface melt over the study period (Figure 2.11B).

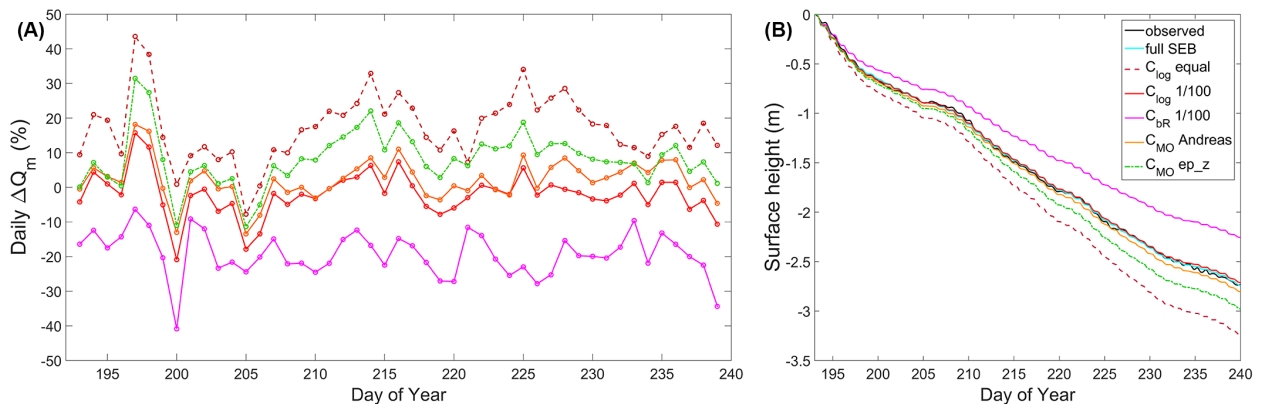


Figure 2.11. (A) Deviation from daily Q_M for a range of simplified SEB models with varying turbulence parameterisations (stability and roughness scheme identified), and (B) the cumulative effect of these deviations on modelled surface height over the study period. Each of the simplified models also assumes negligible Q_R and Q_G , and constant T_s and L_o .

2.7 Conclusions

A method to observe the complete surface energy balance of a glacier has been employed in this study to investigate the ablation characteristics of a mid-latitude, alpine glacier. Direct observations of S_i , S_r , L_i , L_o , Q_H , Q_L , Q_R , and Q_G were implemented in an SEB model to produce half-hourly estimates of surface ablation, which were then compared with the observed ablation values over a 47 day period. In addition, the Q_H and Q_L observations, obtained using eddy covariance measurements, were used to evaluate the performance of a range of bulk method parameterisation techniques commonly used in glacier SEB studies, where direct measurement of the turbulent fluxes is rare.

In general, the modelled ablation values showed excellent agreement with the observed data, accurately estimating the total surface height loss over the period (2.74 m), and providing good performance at daily (r: 0.95; RMSE: 0.01m/day) and 30-minute (r: 0.78; RMSE: 0.001m/30 min) timescales. The observation system effectively captured and closed the surface energy balance of the glacier, and maintained continuous operation throughout the study period, indicating it to be a useful system for investigating glacier-atmosphere interactions. The SEB partitioning of Nordic Glacier was found to be similar to other mid-latitude glaciers, with net radiation dominating Q_M (65.2%). Q_H was also observed to be an important contributor to melt energy (29.7%), underlining the need to accurately account for the turbulent heat fluxes. At daily and sub-daily timescales, Q_R was observed to be a substantial energy source during heavy rain events (up to 20% of daily melt energy).

EC-derived measurements of z_{0v} obtained for the study site showed general agreement with previously observed values on glaciers, with a distinct difference in mean z_{0v} between periods with a snow ($10^{-3.8 \pm 1.7}$ m) and ice ($10^{-2.2 \pm 0.7}$ m) covered surface. The z_{0v} value for ice is close to

an order of magnitude larger than that commonly used in the literature for similar surfaces (10^{-3} m). This gives emphasis to the importance of site-specific values, particularly when the impact of roughness length selection on the magnitude of the calculated fluxes, as observed in this study, is considered. The observed mean scalar roughness length values of z_{0t} ($10^{-4.6 \pm 1.1}$ m) and z_{0q} ($10^{-6.0 \pm 0.8}$ m) differ by several orders of magnitude from z_{0v} , disagreeing with the common assumption of equal momentum and scalar roughness lengths. Values for z_{0t} showed reasonable agreement with the $z_{0v}/100$ ratio and the surface renewal models of Andreas (1987), and Smeets and van den Broeke (2008).

Three of the stability schemes most commonly used in the bulk method were evaluated in this study through comparison of the parameterised fluxes with the EC-observed values. When implemented with the roughness length values calculated for the study surface (ec_z), each of the tested methods either over- or underestimated the turbulent fluxes for the stable atmospheric conditions on the glacier. The C_{MO} method returned the strongest performance overall, showing significant correlation with the observed fluxes over daily time scales, but a tendency to underestimate stability and the required turbulence suppression. Flux overestimation was most pronounced during days with a suspected low-level wind maximum near measurement height, when the associated decoupling of turbulence generation from the surface may have invalidated Monin-Obukhov similarity theory. Utilising a range of unobserved, assumed roughness length values with the above stability schemes led, in a few cases, to a balancing of errors; the inaccuracies in the roughness values counteracting the deficiencies in the stability functions. As a result, relatively good performance in modelling the turbulent fluxes was achieved using ice and snow z_{0v} values from the literature (10^{-3} m and 10^{-4} m), and a bulk method that assumes neutral conditions (C_{log}) and a 1/100 roughness length ratio. However, the above technique is not firmly

based on the physical characteristics of the study surface and boundary layer, and its transferability to other glaciers and seasons remains uncertain. As observed in this study, the choice of bulk method can dramatically influence the performance of an SEB model ($\pm 40\%$ of daily Q_M), and a systematic approach for selecting the most accurate method for given conditions on a glacier requires further development.

Chapter 3:

A multi-season investigation of glacier surface roughness lengths through in situ and remote observation

3.1 Summary

The roughness length values for momentum, temperature, and water vapour are key inputs to the bulk aerodynamic method for estimating turbulent heat flux. Observations of the roughness lengths are rare on glacier surfaces, and substantial uncertainty remains in the values and ratios commonly assumed when parameterising turbulence. Over three melt seasons, *in situ* and remote methods were implemented to derive the momentum and scalar roughness lengths at several locations on two mid-latitude mountain glaciers. The transferability of values between locations and years was examined, along with the temporal variability of roughness lengths within a season. Seasonal mean momentum roughness length values from eddy covariance observations at each location ranged from 0.7-4.5 mm for ice surfaces, and 0.5-2.4 mm for snow surfaces. Within a season, temporal variability in momentum roughness length was found to be substantial ($>$ an order of magnitude) over melting snow surfaces, while from one season to the next, mean momentum roughness length values over ice remained relatively consistent at a given location (<0.2 mm difference between seasonal mean values). Changes in wind direction affected the magnitude of the momentum

roughness length, due to the anisotropic nature of features on a melting glacier surface. Persistence in downslope wind direction on the glacier surfaces, however, reduced the influence of this variability. Eddy covariance derived values of the scalar roughness lengths showed considerable variation (up to two and a half orders of magnitude) between location and season, and little agreement with commonly assumed ratios between their values and the roughness length for momentum. The Andreas (1987) surface renewal model returned the best performance of the tested methods in estimating the scalar roughness lengths, and is recommended where momentum roughness length values have been initially determined. Two techniques were developed in this study for the remote estimation of roughness, utilising LiDAR-derived digital elevation models, with a 1 x 1 m resolution, obtained for each study location and season. Both techniques were shown to differentiate between ice and snow cover, and return momentum roughness values that were within 1-2 mm (\ll an order of magnitude) of mean eddy covariance observations. For ice surfaces, roughness estimates were found to be relatively persistent at each location over the study period (differences of 0-1.3 mm y^{-1}), potentially allowing for the use of elevation model-derived roughness values over several seasons.

3.2 Introduction

The turbulent fluxes of sensible and latent heat can form a major component of the surface energy balance (SEB) of a glacier, and substantially influence its rate of surface melt (Hock and Holmgren, 1996; Anderson *et al.*, 2010; Fitzpatrick *et al.*, 2017). With a lack of direct measurement on glaciers, the bulk aerodynamic method is commonly used to parameterise the turbulent fluxes, requiring input of roughness length values for momentum (z_{0v}), temperature (z_{0t}), and water vapour (z_{0q}). Observations of roughness length are rare on glacier surfaces,

however. The majority of SEB studies use values and ratios from previous research on similar surface types (e.g. Gillett and Cullen, 2011; Giesen *et al.*, 2014), or treat roughness lengths as model tuning parameters (e.g. Braun and Hock, 2004; Sicart *et al.*, 2005), rather than obtaining site-specific measurements. This approach introduces uncertainty into turbulent flux estimation, as the transferability of roughness lengths between locations and seasons is unknown. Furthermore, parameterisation of the turbulent heat fluxes has been shown in previous studies to be highly sensitive to the implemented roughness lengths (up to a doubling of the calculated flux for one order of magnitude increase in z_{0v}), and to dominate over stability corrections as a source of uncertainty (Munro, 1989; Braithwaite, 1995; Brock *et al.*, 2000; Fitzpatrick *et al.*, 2017). The importance of accurate roughness length selection, as identified in these studies, highlights the need for further research on the spatial and temporal variability of their values on glacier surfaces, and on the methods used in their estimation.

The roughness length values are defined as the lower limits of integration in the bulk-gradient or ‘K’ theory parameterisation of the turbulent fluxes (Stull, 1988). z_{0v} can be thought of as the height above the surface at which wind speed, extrapolated downwards along an assumed logarithmic profile, will reach its surface value. Similarly, z_{0t} and z_{0q} can be considered to be the heights at which temperature and specific humidity reach their surface values, respectively. z_{0v} accounts for the effects of form drag on the near-surface wind profile due to the interaction of airflow with features on the surface. In many glacier studies and climate models (e.g. Van As, 2011; Fausto *et al.*, 2016), z_{0v} values of 1 mm and 0.1 mm are used for ice and snow surfaces, respectively, and are often assumed constant with time. Where measurements have been obtained on glacier surfaces, however, a large range of z_{0v} values have been recorded, with several orders of magnitude of variation between different glaciers and seasons (e.g. Van den Broeke *et al.*, 2005;

Brock *et al.*, 2010). In addition, existing values for z_{0v} on glaciers (observed through mast-based vertical wind profile measurements, or estimated from eddy covariance (EC) observations or microtopography surveys) only provided values for an individual location or turbulent footprint. Implementing these single values in a glacier-wide distributed model or in a point model at another location on the glacier may not account for the potential variability in surface roughness that may exist across a glacier surface (e.g. Smith *et al.*, 2016). The turbulent footprint referred to above is the source region for the turbulent fluxes received at a given location. It represents the upwind area that influences and contributes to the observed fluxes, and hence, the surface properties that modulate turbulence generation. Broadly speaking, the turbulent footprint for fluxes measured at a given height will extend upwind by a distance of roughly 100 times the measurement height (Burba, 2013).

Efforts have been made in previous boundary-layer studies over different land surfaces to determine momentum roughness length values for large areas, including over forestry, scrubland, and outwash plains (e.g. Nield *et al.*, 2013; Li *et al.*, 2017). A range of remote sensing techniques have been implemented in such studies, including the use of light detection and ranging (LiDAR) systems. Paul-Limoges *et al.* (2013) used digital elevation models (DEMs), obtained from airborne LiDAR, to estimate z_{0v} values over a harvested forest surface ($z_{0v} = 0.13$ m), and found good agreement with corresponding EC-derived values ($z_{0v} = 0.12$ m). Similar studies on mountain glaciers are extremely rare. Smith *et al.* (2016) used terrestrial-based structure-from-motion photogrammetry and laser surveying to generate a distributed map of z_{0v} estimates for a glacier. Meteorological-based evaluation of the returned z_{0v} estimates was not carried out, however.

The scalar roughness lengths (z_{0t} and z_{0q}) are commonly estimated in SEB studies using a fixed ratio with z_{0v} , and are generally assumed to be equal to or one to two orders of magnitude

smaller than the momentum roughness length (e.g. Hock and Holmgren, 2005; Sicart *et al.*, 2005; Hoffman *et al.*, 2008). Molecular diffusion controls the rate of scalar transfer with a surface, and having a smaller spatial scale than the form drag processes driving momentum transfer, it is likely that the scalar roughness lengths would be smaller (Beljaars and Holtslag, 1991). The persistence of this ratio with time is uncertain, however. Surface renewal methods have been implemented in some studies (e.g. Andreas, 1987; Smeets and van den Broeke, 2008), where variation in this ratio is described as a function of the roughness Reynolds number R_* . Changes in mean air temperature and relative humidity have also been proposed as drivers of scalar roughness length variation (e.g. Calanca, 2001; Park *et al.*, 2010).

The initial goal of this study is to obtain *in situ* values of the momentum and scalar roughness lengths from multiple locations over several seasons. EC-observed data will be implemented into the bulk aerodynamic method to derive these values. The temporal variability of roughness lengths on a glacier will be examined, and the transferability of values between location and years will be assessed. Commonly assumed values and ratios from the literature will be compared with the obtained data, and predictive relationships for the scalar roughness lengths will be tested. The second goal of this study is to develop remote methods for estimating momentum roughness lengths for a glacier surface, which would facilitate SEB modelling for glaciers without *in situ* observations, and distributed modelling for glaciers with point measurements only. Digital elevation models will be obtained for each study location and will be used to provide surface height data for the two roughness methods developed in the study. Turbulence footprint modelling will be employed in one of these methods to identify the region of the glacier surface influencing the EC-derived roughness length values. The estimates from both remote methods will then be compared with those from corresponding *in situ* observations.

3.3 Data and methods

3.3.1 Field Campaign

Observations were carried out over three melt seasons (2014–2016) on two glaciers in the Purcell Mountains of British Columbia, Canada (Figure 3.1). Nordic Glacier (51°26' N, 117°42'W) is a small (~5 km²), north-facing glacier, ranging in elevation from 2,000 m to 2,900 m above sea level (a.s.l.), approximately. An automatic weather station (AWS) was installed in the ablation zone of the glacier through July and August 2014 (NG14). Conrad Glacier (50°49' N, 116°55'W) is located 87 km to the southeast of Nordic, with an area of ~15 km², and an elevation range of 1,800 m to 3,200 m a.s.l., approximately. A total of four AWS deployments were executed on Conrad during 2015 and 2016; two stations in the ablation zone from July to September 2015 (CG15-1 and CG15-2), and one in both the ablation (CG16-1) and accumulation (CG16-2) zones from June to August 2016 (Table 3.1). An exposed ice surface was present during observations at NG14, CG15-1, CG15-2, and for most of the observation period at CG16-1, while a snow surface was present throughout at CG16-2, and for the first 10 days at CG16-1. A transitional snow surface was present for the first four days at NG14, with partial snow cover diminishing to a fully bare ice surface.

Table 3.1. Locations and dates of operation of the automatic weather stations used in this study.

Station	NG14	CG15-1	CG15-2	CG16-1	CG16-2
Glacier	Nordic	Conrad	Conrad	Conrad	Conrad
Location	51.43434°N 117.69973°W	50.82486°N 116.92247°W	50.82306°N 116.92128°W	50.82303°N 116.91992°W	50.78219°N 116.91197°W
Zone	ablation	ablation	ablation	ablation	accum.
Elevation	2208 m	2138 m	2163 m	2164 m	2909 m
Deployed	12/07/2014	15/07/2015	16/07/2015	19/06/2016	16/06/2016
Removed	28/08/2014	05/09/2015	07/09/2015	28/08/2016	22/08/2016

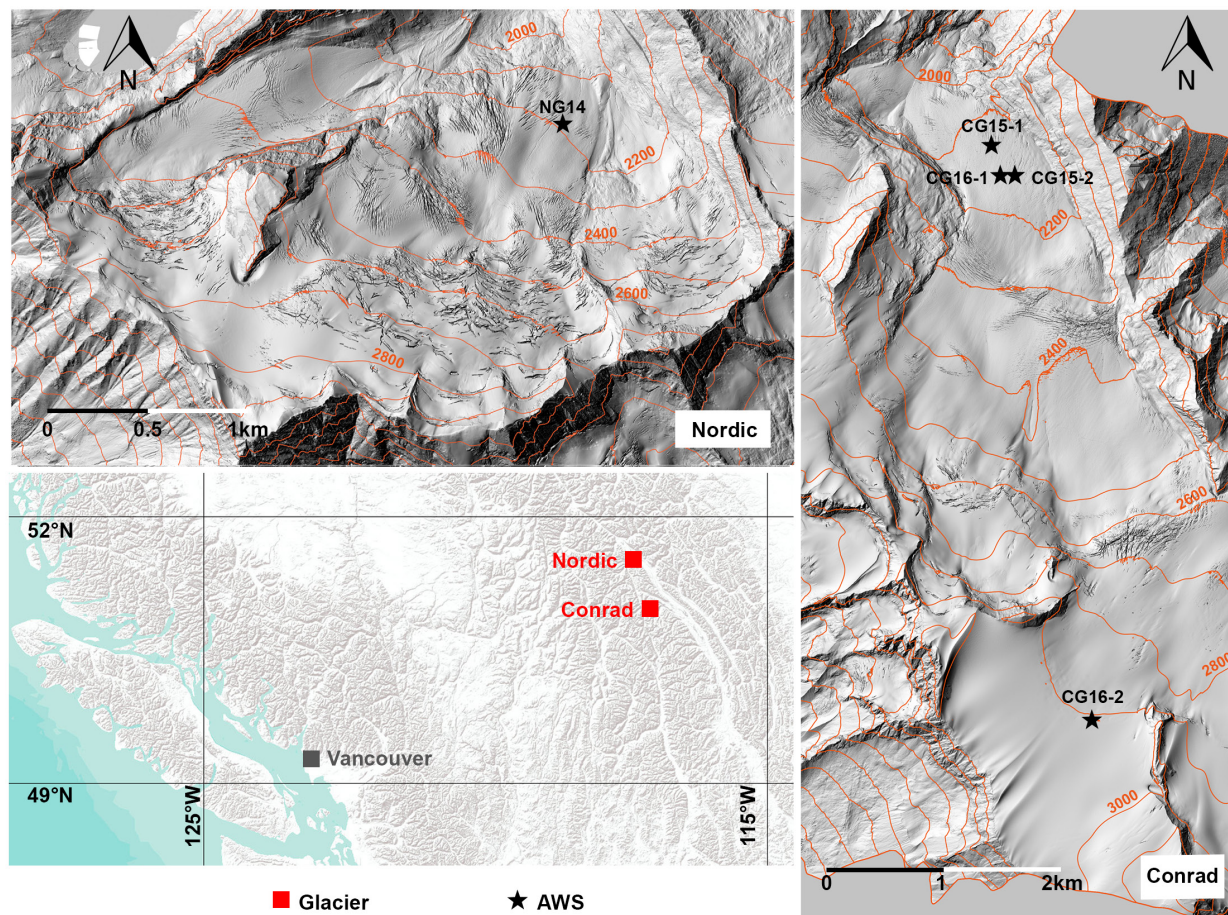


Figure 3.1. Location of the study glaciers and the stations installed during the 2014–2016 melt seasons.

3.3.2 AWS

The AWS developed for this project (see Section 2.4.1) was equipped with an array of meteorological and glaciological sensors to observe the complete SEB, with additional sensors added to the stations each year (Table 3.2). Open and closed path eddy covariance (OPEC and CPEC) systems were used in this project to observe the turbulent heat fluxes, with both forms installed on the same station, in some cases (CG15-1 and CG16-1). Both systems were comprised of a 3D sonic anemometer, and an infrared gas analyser; the OPEC analyser has a sample space that is open to passive air flow, while the CPEC analyser has a closed sample space into which air

Table 3.2. Instrument list for each deployed station, including sensor accuracy and height of installation.

Variable	Sensor	Accuracy	NG14	CG15-1	CG15-2	CG16-1	CG16-2
Wind speed/direction	Young 05103ap Wind Monitor	$\pm 0.3 \text{ ms}^{-1}$	●	●	●	●	●
Air temperature/humidity	Rotronic HC2 Probe	$\pm 0.1 \text{ }^\circ\text{C} / 0.8\%$	●	●	●	●	●
Air temperature/humidity	Aspirated Rotronic HC2 Probe	$\pm 0.1 \text{ }^\circ\text{C} / 0.8\%$	-	-	-	●	●
Atmospheric Pressure	Vaisala PTB110	$\pm 0.3 \text{ hPa}$	●	●	●	●	●
Precipitation	Texas Elec. Tipping Bucket Gauge	$\pm 1\%$ (up to 10 mm hr^{-1})	●	●	●	●	●
Radiation fluxes	Kipp & Zonen CNR4	10 - 20 W m^{-2} (pyranometer) 5 - 15 W m^{-2} (pyrgeometer)	●	●	●	●	●
Turbulent fluxes: water vapour 3D wind (u,v,w) sonic temp	OPEC System CSI IRGASON CSI IRGASON CSI IRGASON	$3.5 \times 10^{-3} \text{ gm}^{-3}$ 1 mm s^{-1} $\pm 0.025^\circ\text{C}$	●	●	-	●	-
Turbulent fluxes: water vapour 3Dwind (u,v,w) sonic temp	CPEC System LI-7200 Gill R3-50 Gill R3-50	$\pm 2\%$ $< 1\% \text{ RMS}$ $\pm 0.1^\circ\text{C}$	-	●	●	●	●
Ground heat flux	Thermistor Array (self)	$\pm 0.1 \text{ }^\circ\text{C}$	●	●	●	●	●
Surface height	CSI SR50A Sonic Ranger	$\pm 0.01 \text{ m}$	1	3	3	3	3
Surface temp	Apogee SI-111	$\pm 0.2 \text{ }^\circ\text{C}$	-	1	1	2	2
Station tilt	Turck Inclinometer	$\pm 0.5^\circ$	●	●	●	●	●
Data storage	CSI CR3000 Logger	-	●	●	●	●	●
Site/Surface Conditions	Time Lapse Camera (self)	-	●	●	●	●	●
z (m)	-	-	2.0	2.0	2.0	1.9	1.9
z_u (m)	-	-	2.6	2.5	2.6	2.6	2.4

is drawn using a pump. Implementing these methods together helped minimise gaps in the turbulence dataset (OPEC analysers are susceptible to errors during precipitation), and enabled a comparison of their values and performance in a glacial environment. The EC data was recorded in raw 20Hz format, with observations from the remaining sensors stored in one-minute averages.

The meteorological sensors were housed on a four-legged quadpod, which provided a stable platform (verified by an inclinometer sensor) that lowered as the ice melted, and maintained a constant height of the sensors above the surface. EC measurements were carried out at a constant height ($\sim 2 \text{ m}$ at each station) to avoid substantially varying the turbulence footprint area and to reduce the risk of elevating the sensor above the turbulence coupled with the surface (Burba, 2013;

Aubinet, 2008). The installation site for each station was selected based on the criteria of a relatively uniform upwind footprint and slope angle, so as to minimise the corrections required in the EC (and radiation) data processing. The EC systems were installed on the upslope side of each station, so as to be the first point of contact with the prevailing wind (downslope), and to help minimise flow distortion. Time lapse cameras at each location were used to observe the surface and atmospheric conditions over a season, and to monitor station behaviour.

Over the three melt seasons, the stations performed well, operating continuously over each study period. The solar power systems for the stations had been designed to have sufficient battery storage for approximately a week of operation without sufficient recharge (due to persistent overcast conditions or covering of the solar panels by snow/ice.). If battery voltages dropped below a critical level, the system was designed to restrict power supply to the higher consuming sensors (e.g. CPEC system) to ensure continued operation of the bulk of the instruments, and to allow the batteries to recharge. This occurred at only one station, CG16-2 in the accumulation zone, after consecutive periods of snowfall and persistent low cloud, resulting in four intermittent gaps in the CPEC dataset (28% of total observation time).

3.3.3 LiDAR

Airborne LiDAR was employed to obtain high resolution topographic data over each of the study locations, using a Riegl 580 laser scanner and dedicated Applanix PosAV 910 Inertial Measurement Unit. In general, flights were performed over Nordic and Conrad glaciers twice per year (Table 3.3), close to the end of the winter and summer seasons (April and September), as part of an ongoing mass balance survey of the study glaciers (Brian Menounos, personal communication, February 27, 2018). By analysing the altimetry data from these times of the year,

Table 3.3. Dates of LiDAR flights over the two study glaciers from 2014 to 2016. *For the September 12th 2015 flight over Conrad Glacier, only the accumulation zone was adequately captured.

	Nordic Glacier		Conrad Glacier	
	Spring	Autumn	Spring	Autumn
2014	July 10 th	Sept 11 th	-	Sept 11 th
2015	April 19 th	Sept 11 th	April 20 th	Sept 12 th *
2016	April 17 th	Sept 12 th	April 17 th	Sept 12 th

it was hoped that the variation in surface roughness due to the transition from a snow-covered to bare ice surface could be captured. In addition, the repeat mapping of each location from one year to the next would help identify the persistence in surface roughness. In 2014, April flights were not performed over the glaciers (a July flight was performed over Nordic), while in 2015, the September flight over Conrad captured usable data for the accumulation zone, only.

3.3.4 Data Treatment

Eddy Covariance Data

Prior to calculating observed values for the turbulent heat fluxes and roughness lengths, the raw (20 Hz) EC data were passed through a series of preprocessing steps using the EddyPro data package (LI-COR, 2016). These steps are described in detail in Section 2.4.3, but a summary of the main techniques is provided below. A planar fit coordinate rotation method (Wilczak et al., 2001) was applied to all of the sonic anemometer data to account for misalignment of the z axis of the sensor with the w component of the mean air flow. For the OPEC water vapour measurements, the Webb-Pearman-Leuning correction (Webb *et al.*, 1980) was used to correct for the density effects of air temperature fluctuations, while readings from periods affected by precipitation on the analyser windows were removed. These corrections were not required for the

CPEC water vapour data. The turbulence data were averaged over 30-minute blocks, and the calculated fluxes were filtered using quality tests for steady state and developed turbulent conditions, following Mauder and Foken (2004).

LiDAR Data

The trajectories of each LiDAR flight had been previously post processed using a network of permanent GPS base stations in British Columbia (Brian Menounos, personal communication, February 27, 2018). The positional uncertainties of the flight trajectories were typically better than 5 cm, with the total uncertainty in the processed LiDAR point clouds better than ± 10 cm, while the average point density for the LiDAR surveys over the ice-covered terrain was 1–2 laser shots per m^2 . LAStools (Isenburg, 2006) was utilised to classify the LiDAR data into ground and non-ground laser returns. The ground returns were subsequently gridded into DEMs with a 1 m^2 grid cell, the grid lines aligned with true north and east.

3.3.5 In Situ Roughness Length Values

Roughness length values were calculated by implementing EC data into the bulk method, with separate values calculated for OPEC and CPEC systems when both sensors were used at the same station:

$$z_{0v_ec} = \exp \left[-\kappa \frac{u_{ec}}{u_{*ec}} - \psi_m \left(\frac{z}{L_{ec}} \right) \right] z, \quad (3.1)$$

$$z_{0t_ec} = \exp \left[-\kappa \frac{T_{ec} - T_s}{\theta_{*ec}} - \psi_h \left(\frac{z}{L_{ec}} \right) \right] z, \quad (3.2)$$

$$z_{0q_ec} = \exp \left[-\kappa \frac{q_{ec} - q_s}{q_{*ec}} - \psi_h \left(\frac{z}{L_{ec}} \right) \right] z, \quad (3.3)$$

where κ is the von Kármán constant (0.4), z is the sensor height, and u_{ec} , T_{ec} , q_{ec} , u_{*ec} , θ_{*ec} , and q_{*ec} are the 30 minute EC-observed values for mean wind speed, air temperature, specific humidity, friction velocity, and the surface layer scales for temperature and specific humidity, respectively (Conway and Cullen, 2013). $\psi_m\left(\frac{z}{L_{ec}}\right)$ and $\psi_h\left(\frac{z}{L_{ec}}\right)$ are the vertically integrated stability functions for momentum and heat (Beljaars and Holtslag, 1991; Dyer, 1974), where L_{ec} is the Monin-Obukhov length. Glacier surface specific humidity q_s is calculated from atmospheric pressure p , and the surface vapour pressure (e_s) which is assumed to be at saturation at the glacier surface temperature T_s ($q_s = 0.622 e_s/p$).

To minimise potential errors and to obtain roughness lengths representative of the conditions at each site, an extensive series of filters were applied to the 30-minute values (see Section 2.4.5 for full details). These filters included a 90° wind direction window centred on the main axis of the EC sensor (to minimise the influence of flow distortion due to the station structure), minimum values for wind speed ($> 3 \text{ m s}^{-1}$) and u_{*ec} ($> 0.1 \text{ m s}^{-1}$), minimum differences between measurement and surface height values of air temperature ($> 1^\circ\text{C}$) and vapour pressure ($> 66 \text{ Pa}$) (Calanca, 2001; Conway and Cullen, 2013), a minimum scalar roughness length value of $1 \times 10^{-7} \text{ m}$ based on the mean free path length of molecules (Li *et al.*, 2016), a precipitation filter, and a test for stationarity of the turbulence (Foken, 2008). Only roughness length values calculated during near-neutral stability conditions ($-0.1 < \frac{z}{L_{ec}} < 0.2$) were retained, to minimise the uncertainty associated with the stability functions applied in Equations 3.1–3.3 during non-neutral conditions (Smeets and van den Broeke, 2008; Conway and Cullen, 2013).

Scalar Roughness Length Modelling

The scalar roughness lengths from Equations 3.2 and 3.3 were compared with values from the surface renewal models of Andreas (1987) and Smeets and van den Broeke (2008), where the ratio of the scalar (z_{0s}) and momentum roughness lengths are expressed as a function of the roughness Reynolds number R_* :

$$R_* = \frac{u_* z_{0v}}{\nu}, \quad (3.4)$$

$$\ln(z_{0s}/z_{0v}) = b_0 + b_1 \ln(R_*) + b_2 \ln(R_*)^2. \quad (3.5)$$

ν is the kinematic viscosity of air ($1.5 \times 10^{-5} \text{ m}^2 \text{ s}^{-1}$), and the EC-derived roughness lengths (Equations 3.1–3.3) were used to populate z_{0v} and z_{0s} . The values of the empirical coefficients (b_0 , b_1 , and b_2) change for smooth ($R_* \leq 0.135$), transitional ($0.135 < R_* < 2.5$), and rough ($R_* \geq 2.5$) flow regimes, and between models.

3.3.6 Remote Momentum Roughness Length Estimation

The set of 1 x 1 m grid cell DEMs obtained for the study glaciers from the LiDAR data were utilised to remotely estimate momentum roughness length values. Estimates were determined at the location of each station using the DEMs from the same year the station was in place, and compared with the EC-derived z_{0v_ec} values. September DEMs were used to estimate roughness length values for bare ice surfaces, and April DEMs for snow-covered surfaces (both the April and September DEMs at CG16-2 in the accumulation zone represent a snow-covered surface). The DEM for Nordic Glacier in July 2014 was used to estimate roughness lengths for the transitional snow-ice surface at NG14. The estimation of z_{0v} was also repeated on DEMs from periods without a station present at that location to allow for an examination of the temporal variation of roughness

properties at each site over the three years. Two methods were developed in this study, referred to as the (i) block and (ii) profile methods. Both methods assume that a DEM with a 1 x 1 m grid cell can adequately resolve the scale of the surface features that have the primary influence on roughness length. Where airflow encounters a dense distribution of roughness elements (as can be present on an ablating glacier surface), the flow is likely to experience wake-interference or skimming (Wieringa, 1993), reducing the relative influence of smaller scale roughness features on z_{0v} (Smeets *et al.*, 1999), and increasing the influence of elements that are potentially resolvable at the DEM scale.

Both methods draw on the empirical theory of Lettau (1969) for the estimation of z_{0v} from microtopography measurements:

$$z_{0v} = 0.5h^* \frac{s}{S}, \quad (3.6)$$

where h^* is the average effective height of the roughness elements above the surface, s is the average crosswind silhouette or face area of the roughness elements encountered by oncoming air flow, S is the lot area, equal to the total area of the site divided by the number of roughness elements on its surface, and the value 0.5 represents an average drag coefficient. The original application of the above theory assumes that the surface is composed of regularly spaced roughness elements of similar size and shape, an assumption that may not always hold for a glacier surface.

DEM: Block Estimation

The first method developed in this study to estimate z_{0v} aimed to account for the variation in shape and distribution of roughness elements on a glacier surface. First, the form drag generated by the features on an individual portion or block of the surface was estimated, before combining the

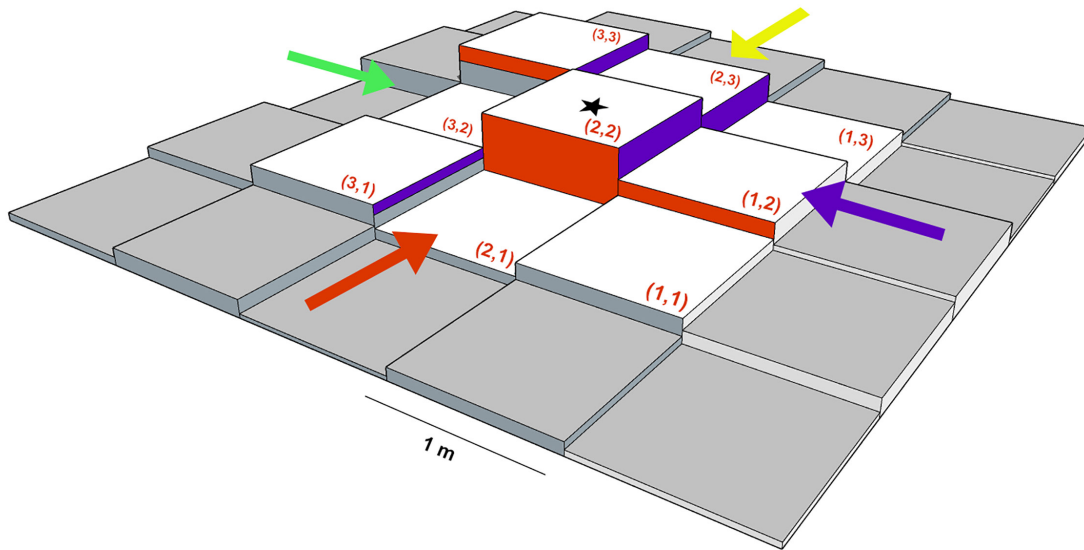


Figure 3.2. DEM-based block method for estimating the local drag generated by roughness elements on the surface. The total surface area that is perpendicular and ‘visible’ to the direction of air flow (matching-coloured face area and arrows) is assigned to s_b (Equation 3.7). The displayed grid cell indices are for airflow in the direction of the red arrow. A F_{D_local} value is estimated for the four cardinal wind directions, with the values assigned to the central grid cell of the block (starred). The block is then moved by one grid cell at a time, and the process repeated over the DEM.

influence of each portion over a footprint to determine the momentum roughness length value for a given downwind location. Similar methods were proposed and evaluated by Kondo and Yamazawa (1986) for estimating z_{0v} over irregular surfaces. To account for the often dense distribution of roughness elements on a melting glacier surface, and the effects of this distribution on airflow, the block method developed here also considers the relative height differences and potential sheltering influence of neighbouring features on the surface.

As the method would be evaluated using roughness measurements derived from the EC systems, it was applied to subareas of each DEM that contained the potential turbulent footprint for a given station. Each subarea was 2,000 x 2,000 m in dimension, and centred on the grid cell containing the station site. For each grid cell in the subarea, a one-cell-thick border was selected around the cell of interest, creating a 3 x 3 m block of cells (Figure 3.2), representing a roughness element and its surrounding area of influence. A localised drag value (F_{D_local}) was estimated for each block, by utilising Equation 3.6, and building on the methods of Smith *et al.* (2016). The heights of the cells in the block were detrended for the mean slope of the glacier in the region of the station, as it was assumed that mean airflow was parallel to this plane. The height values within the block were normalised, and the mean height of all the cells above the zero plane was assigned to h_b^* . A value for s_b was calculated for each cardinal wind direction, as follows. The heights of the first line of cells in the block perpendicular to the oncoming wind (h_{i1}) set the base levels for the silhouette area, and the maximum height of the cells in each row set the upper level. The sum of the silhouette areas of each row was then assigned to the s_b value for that block and wind direction:

$$s_b = \sum_{i=1}^n \max(h_{ij}) - h_{i1} , \quad (3.7)$$

where n is the number of rows. The area of the block was assigned to the value for S_b . F_{D_local} values were then calculated for each of the four cardinal wind directions for each 1 x 1 m grid cell; the block in Figure 3.2 shifting by one cell each step:

$$F_{D_local} = 0.5h_b^* \frac{S_b}{s_b} . \quad (3.8)$$

A range of border thicknesses around each grid cell, from one to five cells (3 x 3 m to 11 x 11 m block area), was also implemented to test the performance sensitivity to this choice.

To estimate a momentum roughness length value at the location of a station, the effective influence of the F_{D_local} values over the entire footprint must be determined. The flux footprint of the turbulence observed at each station was estimated using the model of Kljun *et al.* (2015). This model involves a two-dimensional parameterisation of a more complex, backward Lagrangian particle dispersion model (the LPDM-B model in Kljun *et al.*, 2002). In the above study, the parameterisation was developed and evaluated for a wide range of boundary layer conditions and surface types, and was shown to agree with the footprint estimates of the more complex model. To estimate the footprints for the glacier stations in this study, EC-observed values for mean wind speed and direction, z_{0v_ec} , L_{ec} , u_{*ec} , and the standard deviation of lateral wind velocity were implemented into the parameterisation. Flux footprint maps were generated from the model, with a 1 x 1 m grid cell and dimensions of 2,000 x 2,000 m, centred on the station location, to match the selected DEM subareas. Each 1 x 1 m grid cell was assigned a flux footprint value (f_c), representing its normalised contribution to the turbulent flux observed at the station. Maps were generated for every 30-minute period in the EC data, from which an average seasonal footprint for the station was determined. For stations with both OPEC and CPEC systems, separate footprint maps were generated for each to investigate sensitivity to the observation method.

The seasonal flux footprint map for a given station (or EC system) was overlaid over the corresponding F_{D_local} values for the wind direction of interest. The F_{D_local} value for each grid cell was then weighted by its flux footprint contribution, and summed over the subarea to obtain

z_{0v_bloc} :

$$z_{0v_bloc} = \sum_{i=1}^n F_{D_local_i} f_{c_i} , \quad (3.9)$$

where n is the number of grid cells in the subarea. This process was then repeated for the DEMs available from each season. Standard error propagation methods were used to calculate the uncertainty in z_{0v_bloc} by considering the uncertainties in the LiDAR height data ($< \pm 0.1$ m) and the normalised mean square error in the f_c values from the footprint model (0.48; Kljun *et al.*, 2015). The primary application of a remote technique to estimate momentum roughness lengths would be to obtain values for where *in situ* observations are not available, and therefore, where the turbulent flux footprint for a given site is unknown. z_{0v_bloc} values were first calculated with EC-derived footprints, as above, to evaluate the effectiveness of the local form drag estimation (Equation 3.8). To test the performance of the block method in situations when EC data is not available, the observed turbulent footprints were then replaced with a series of assumed footprint areas at each site and applied to the corresponding F_{D_local} values to calculate z_{0v_bloc} .

DEM: Profile Estimation

The second method developed in this study takes a profile-based approach to estimating momentum roughness lengths, and aims to identify the length scales relevant to form drag over that profile, rather than using the element by element approach of the previous technique. As with the block method, the first step was to detrend the surface height values for the mean slope of the glacier. Beginning with roughness estimation for the downslope (southerly) wind direction, a profile of grid cells was selected from a given DEM along the glacier slope; 600 m in length, one grid cell wide, and centred on the location of a station. A linear trend was fitted to this profile to identify the slope, and the trend was then removed from the original height data (Figure 3.3A-B). This step was repeated for 50 parallel profiles on either side of the central ‘station’ profile (101

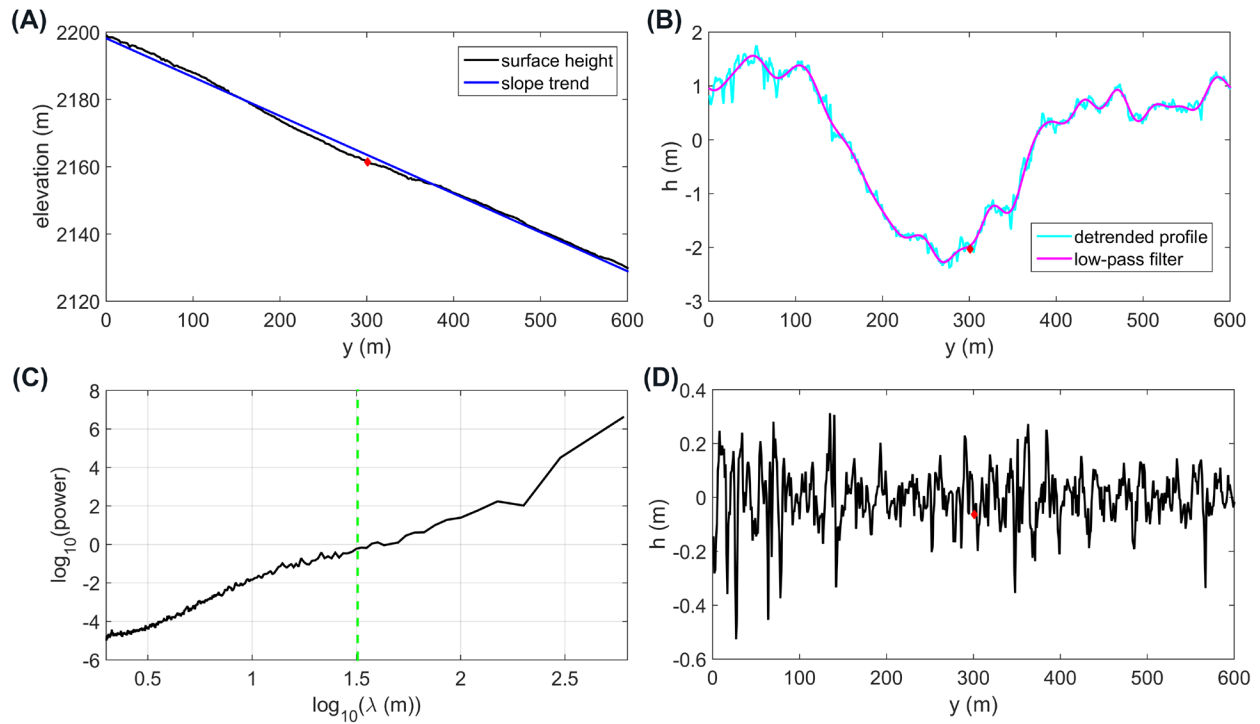


Figure 3.3. (A) Surface height profile from the September 2016 DEM centred on CG16-1 (red diamond) and a fitted linear trend; (B) detrended profile and low-pass filter according to cut-off wavelength of λ_0 ; (C) log-log power spectrum of the mean detrended profile, with large scale wavelengths greater than λ_0 (green dashed line) used in the low-pass filtering; (D) filtered profile used in the calculation of momentum roughness length.

profiles, in total). The next step was to determine the scale of the features relevant to form drag, that is, the features that act as obstacles to air flow, and to remove large scale surface features or waves which air flow may follow rather than be impeded by. The power spectrum was calculated for the detrended profile, and a cut-off wavelength was visually identified between large and small scale features. In Figure 3.3C, an example of the mean power spectrum over 101 detrended profiles is shown in log-log for CG16-1 in September 2016. In this case, a cut-off wavelength of $\lambda_0 = 35$ m was manually selected from the plot as differentiating between the large and small power wavelengths. With the cut-off wavelength identified, a fast Fourier transform (FFT) high pass filter

was applied to the detrended profile to remove the large wavelengths (Figure 3.3B), and to obtain a filtered profile. The filtering was performed in the wavenumber (k) domain with the following steps: (i) FFT was applied to the detrended profile $h(y)$ in Figure 3.3B to get $H(k)$; (ii) $H(k)$ values for $k < 2\pi/\lambda_0$ were set to zero; (iii) an inverse FFT was applied to the modified $H(k)$ to get the filtered profile $h(y)$ in Figure 3.3D.

Finally, Lettau's theory was applied to the filtered profile to estimate a value for momentum roughness length. S was calculated as the width of the profile ($w = 1$ m) multiplied by the length of the fetch (L_F) upwind of the station. A range of values for L_F were applied from λ_0 to $2\lambda_0$ in 1 m increments. The height of the grid cells along a given fetch was assigned to an array from h_0 to h_N , where N is the number of grid cells in the fetch, and the standard deviation of the height array along L_F was assigned to h^* . A value for s was obtained from the sum of the height differences between adjoining grid cells:

$$s = w \sum_{j=1}^N |h_j - h_{j-1}|, \quad (3.10)$$

and substituted into Equation 3.6, with S and h^* , to estimate a momentum roughness length value for a given fetch (z_{0v_fetch}). The mean of the z_{0v_fetch} values from $L_F = \lambda_0$ to $2\lambda_0$ was then assigned to the momentum roughness length for the station grid cell (z_{0v_prof}). To examine roughness length variability in the vicinity of the station grid cell, and to determine the uncertainty in the presented results, the above process was repeated for all grid cells in the 101 x 101 m area upwind of the station (i.e. 50 m either side of the station profile).

The profile method was also applied over a range of angles in addition to the prevailing downslope, southerly direction, to examine the effects of changing wind direction on momentum roughness length (Figure 3.4). To do so, the x-y grid matrix of a patch of grid cells (101 m wide

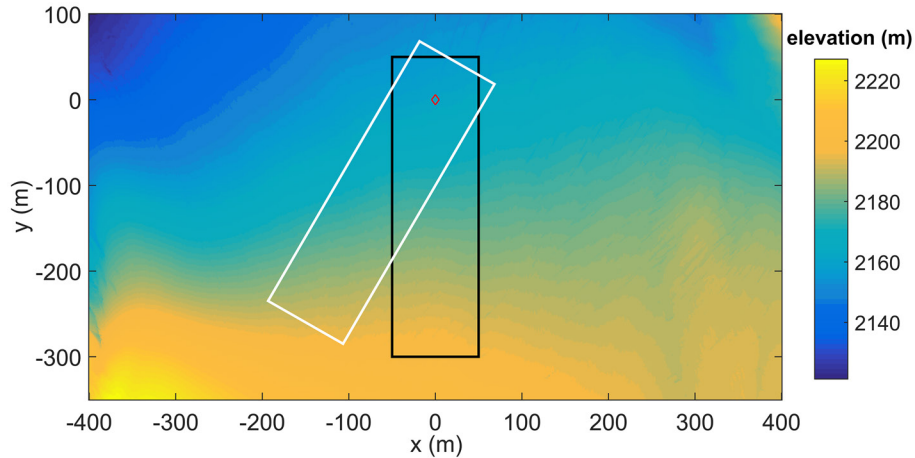


Figure 3.4. Example of the rotation applied to a DEM patch selected around a station location (red diamond), with the original orientation outlined in black, and a rotated patch, turned 30° clockwise, outlined in white.

and 351 m long, containing the station site) was multiplied by a rotation matrix (in 5° increments between 90° and 270°). The height values from the DEM grid cells were then bi-linearly interpolated to the rotated grid to derive new rotated height values. A value for z_{0v_prof} was then calculated as above for profiles in line with the long axis of the patch, for each 5° increment.

The sensitivity of the profile method to the use of a DEM with a finer (1 x 0.1 m) or coarser resolution (3 x 3 m) than the original 1 x 1 m DEM was tested. As a 1 x 0.1 m DEM could not be derived from the LiDAR data, a synthetic test surface was created using data from microtopography profile measurements obtained at CG16-1 at the end of the melt season. Four surface height profiles, 2 m in length and with 0.1 m resolution, were obtained at distances of 10 m, 50 m, 100 m, and 150 m upwind of the station (Figure 3.5A). The profiles were taken perpendicular to the prevailing wind direction (downslope), and measured using a 2 m snow probe, horizontally laid on the surface and allowed to partially melt in place. The long axis of the probe was set as the zero plane, and the height of the surface was measured relative to this level at 0.1 m

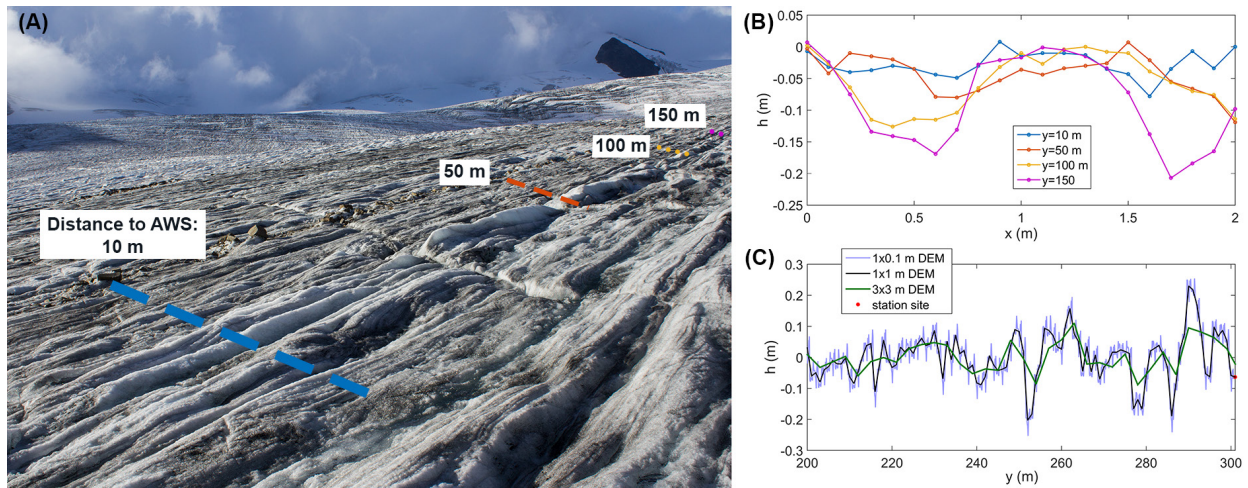


Figure 3.5. (A&B) Microtopography profiles taken upwind of CG16-1 at the end of the 2016 melt season. Profiles were 2 m in width and taken perpendicular to the downslope direction. The locations of the profiles marked in (A) are representative rather than exact. (C) Examples of the filtered height profiles, as derived from the three DEM resolutions used in the z_{0v_prof} sensitivity test.

spacings. Height variability parallel to the downslope direction was expected to be smaller than in the parallel direction which crosscuts supraglacial channels on the surface. Therefore, in the absence of microtopography measurements in this direction, the profile from the cross-slope direction with the smallest variance i.e. the 10 m upwind profile (Figure 3.5B), was used to represent the slope-parallel variance. This 2 m profile was demeaned at a 1 m interval and lined up in a repeated sequence to obtain an extended (600 m long) synthetic microtopography profile. The final test profile was constructed by adding this extended synthetic profile to the detrended profile in the downslope wind direction from the 1 x 1 m DEM. The same synthetic profile was added to the detrended profiles from each side of the station, at 1 m distance apart, yielding the synthetic 1 x 0.1 m DEM. The 3 x 3 m DEM was created by applying a 2-D smoothing of the original 1 x 1 m DEM, using a 3-point running mean in both x (Easting) and y (Northing)

directions. The profile method was then applied to both the 1 x 0.1 m and 3 x 3 m DEMs for the 600 x 101 m area upwind (slope-parallel) of the station, using the same steps as outlined previously. The same threshold wavelength, $\lambda_0 = 35$ m, was used to filter the profiles. Figure 3.5C displays examples of filtered profiles, $h(y)$, as derived from the three DEM resolutions.

3.4 Results

3.4.1 EC-Derived Roughness Lengths

The geometric means of the roughness length values calculated from each EC dataset are presented in Table 3.4, with separate z_{0v_ec} values for periods with snow and ice surfaces. Each of the observed 30-minute roughness length datasets were found not to have a normal distribution (using one-sample Kolmogorov-Smirnov tests), but one that was approximately log-normal. For presenting mean EC-derived values in the remainder of this study, geometric means are used to avoid excessively weighting the larger roughness values (Andreas *et al.*, 2010).

Table 3.4. Seasonal geometric means of the EC-derived roughness length values ($\pm\sigma$) from the open and closed path systems for each station site. z_{0v_ec} values for periods with a snow-covered surface are underlined. The number of 30-minute periods available for roughness estimation (after filtering) is presented in square brackets.

(mm)	NG14 OPEC	CG15-1 OPEC	CG15-1 CPEC	CG15-2 CPEC	CG16-1 OPEC	CG16-1 CPEC	CG16-2 CPEC
z_{0v}	4.5±28.8 [93] <u>0.46±3</u> [16]	3.8±31.7 [206]	2.0±19.2 [281]	0.9±7.4 [417]	1.7±11.7 [308] <u>0.62±5.1</u> [114]	0.7±6.4 [429] <u>0.51±2.3</u> [138]	<u>2.4±16</u> [312]
z_{0t}	0.01±0.1 [77]	0.01±0.88 [181]	0.09±0.81 [270]	0.03±0.28 [390]	0.03±0.23 [396]	0.05±0.29 [546]	0.01±0.07 [247]
z_{0q}	0.001±0.008 [16]	0.23±1.5 [43]	0.28±1.9 [17]	0.21±3.1 [74]	0.02±0.28 [194]	0.01±0.19 [186]	0.01±0.1 [38]

Stable atmospheric conditions persisted over the glaciers for much of each season, limiting the number of suitable 30-minute periods for roughness calculation after application of the filters discussed in Section 3.3.5 (number of available measurements presented in Table 3.4). Across all test sites, z_{0v_ec} had a mean of 2.3 mm and 1 mm for ice and snow, respectively, while the scalar roughness lengths had mean values of 0.05 mm for z_{0t_ec} and 0.11 mm for z_{0q_ec} . Where OPEC and CPEC systems were used on the same station, the OPEC system returned slightly larger mean z_{0v_ec} values (2.8 mm and 1.4 mm, respectively). Mann-Whitney U tests applied to the 30-minute roughness values from CG15-1 rejected the null hypothesis that the z_{0v_ec} values from the OPEC and CPEC systems had the same distribution ($p < 0.01$), but the hypothesis could not be rejected for the scalar values ($p > 0.5$).

The ice z_{0v_ec} values were within the expected range for moderately rough glacier ice (Brock *et al.*, 2006). Where measurements were repeated in the same area a year apart (CPEC observations on CG15-2 and CG16-1), persistence in the mean ice roughness length values was noted (0.86 ± 7.4 mm, and 0.74 ± 6.4 mm, respectively), with a failure to reject the hypothesis of equal distributions ($p = 0.16$). Within a season, substantial variability was noted in the 30-minute z_{0v_ec} values for each ice surface (Figure 3.6A), but with no evident trend in z_{0v_ec} due to changes in surface roughness over time. Mean momentum roughness lengths for snow were also within previously observed values on glacier surfaces, with a particularly large mean value observed at CG16-2 in the accumulation zone (2.4 ± 16 mm). Extensive variability was also present in the 30-minute z_{0v_ec} values for CG16-2 (Figure 3.6B), with a general increasing trend in roughness over the season. Across all stations and seasons, substantial variability was noted in the mean scalar roughness lengths, with z_{0q_ec} , in particular, showing a range of two and a half orders of

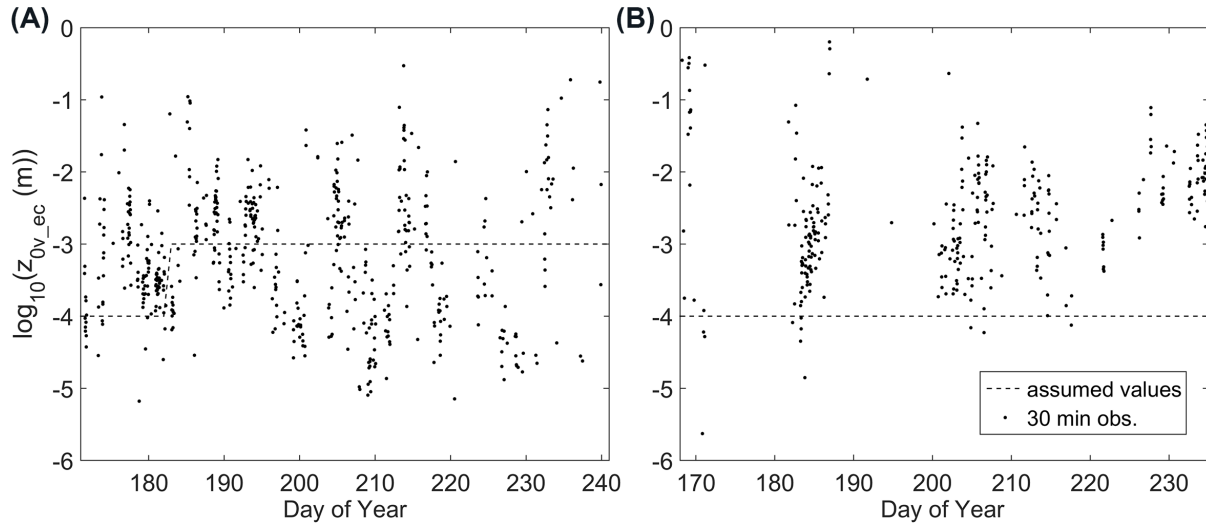


Figure 3.6. 30-minute z_{0v_ec} values as observed at (A) CG16-1 and (B) CG16-2. The dash line represents the commonly assumed z_{0v} values of 1 mm and 0.1 mm for ice and snow, respectively. At CG16-1, the surface transitioned to bare ice on day of year (DOY) 183.

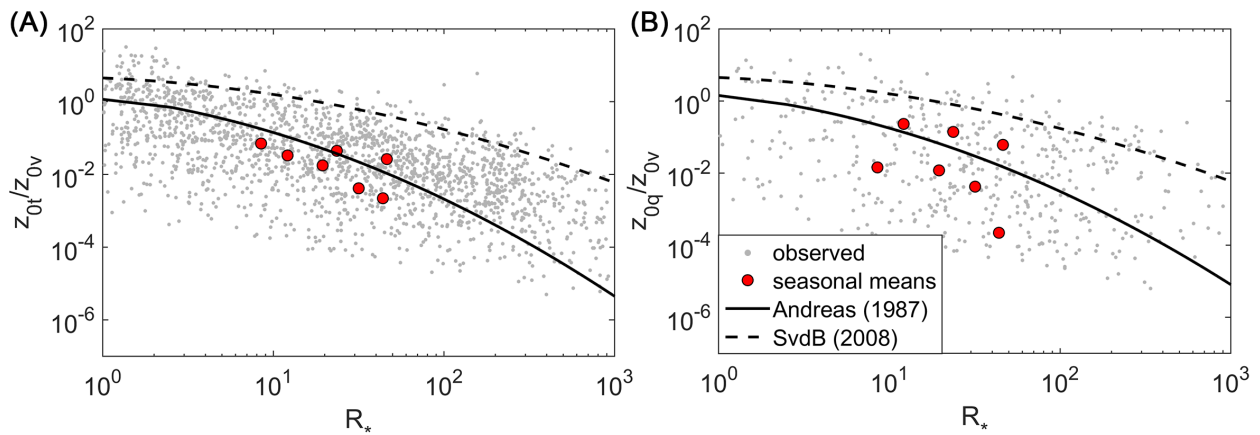


Figure 3.7. Performance of the surface renewal models of Andreas (1987) and Smeets and van den Broeke (2008) for estimating the ratio of (A) z_{0t} and (B) z_{0q} to z_{0v} . The filtered 30-minute (grey) and seasonal mean (red) ratios of the EC-derived roughness lengths and R_* values are shown for all seasons and EC sensors.

magnitude. z_{0t_ec} exhibited less variability (~one order of magnitude), with similar mean values observed for CG15-2 and CG16-1 (0.03 ± 0.28 mm and 0.05 ± 0.29 mm), and a failure to reject the null hypothesis of equal distributions ($p = 0.11$).

The ratios of the 30-minute EC-determined scalar roughness lengths to z_{0v_ec} were expressed as a function of R_* using the data from all stations and seasons (Figure 3.7). These values were compared with the surface renewal models of Andreas (1987) and Smeets and van den Broeke (2008). The seasonal mean ratios and R_* were also compared with these models. In general, the roughness ratios were shown to decrease with increasing R_* , with substantial scatter in the 30-minute values. The seasonal mean z_{0t}/z_{0v} ratios were in line with the output of the Andreas (1987) model ($r = 0.81$; $p < 0.05$), with greater scatter in the z_{0q}/z_{0v} values ($r = 0.2$), while both sets of ratios were overestimated by the Smeets and van den Broeke (2008) model.

3.4.2 Momentum Roughness Length from LiDAR

Block Method

F_{D_local} maps were generated from LiDAR-derived DEMs using the block estimation method (Figure 3.8A-B) for all available years and seasons, and for each of the four cardinal wind directions. Substantial variation in F_{D_local} was observed across each glacier surface, ranging from 10^{-4} m for snow-covered grid cells to $10^{-0.5}$ m for large crevasses. Figure 3.9 displays the seasonal turbulent flux footprint maps generated using the model of Kljun *et al.* (2015) for each EC sensor deployment. In general, the fluxes were sourced from regions to the south of each station, in line with the prevailing downslope winds at each site. Over 80% of flux contribution came from an area within 200 m upwind of each station, with concentrated peak source regions 15–20 m upwind,

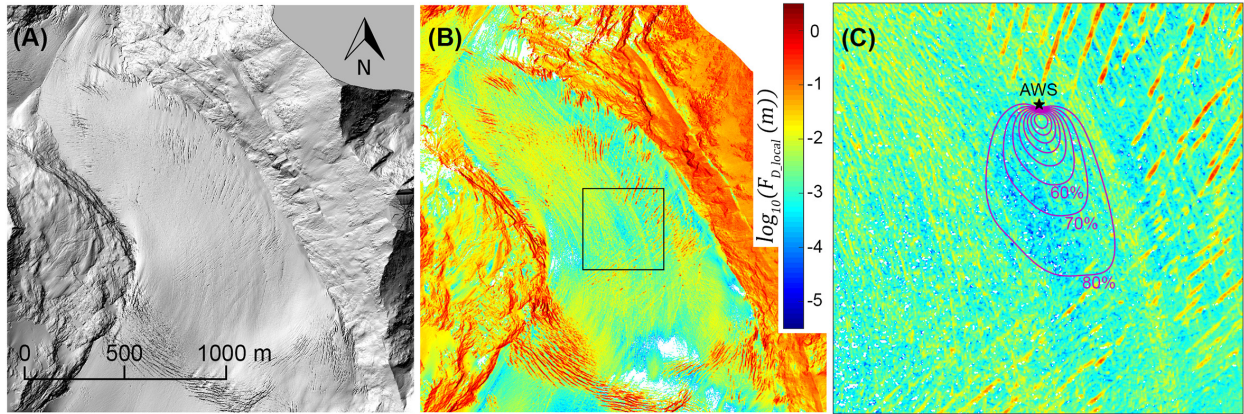


Figure 3.8. Example from CG16-1 of the steps taken to estimate z_{0v_bloc} from LiDAR data: (A) 2,000 x 2,000 m subarea extracted from the DEM; (B) localised drag values (F_{D_local}) calculated for each 1 x 1 m cell; (C) flux footprint for corresponding EC data, shown as percentage of crosswind integrated flux contribution (purple), overlaid over the F_{D_local} map (400 x 400 m square expanded from (B) for display purposes).

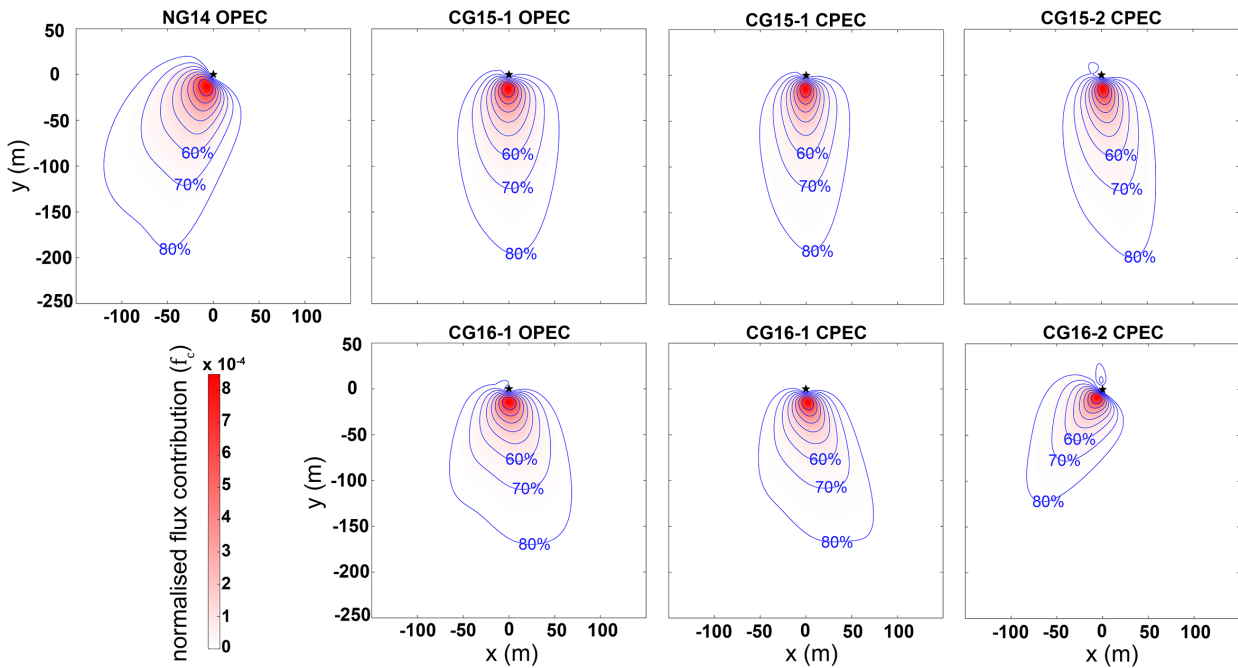


Figure 3.9. Flux footprint maps for each EC system deployed during the study, including percentage of crosswind integrated flux contribution (purple contours). Distances are in metres east (x) and north (y) of the AWS (black star). Maps were produced following the methods of Kljun *et al.* (2015).

on average. The flux footprints of each EC dataset were merged with the corresponding F_{D_local} maps (Figure 3.8C), producing a series of z_{0v_bloc} values for each site. As stated, wind direction was predominately from the south during each station deployment, so the roughness estimates for this wind direction (Table 3.5) are used for comparison with the EC-derived values. z_{0v_bloc} (and z_{0v_prof}) values for the cross-glacier east and west wind directions are presented in Table A.1 and A.2 in the appendices, and the influence of wind direction on the roughness length estimates is discussed in Sections 3.4.3 and 3.5.1. The mean uncertainty in the z_{0v_bloc} values, estimated from propagation of the errors in the LiDAR and flux footprint values, was ± 0.26 mm. Where OPEC and CPEC systems were used simultaneously on the same station (CG15-1 and CG16-1), virtually identical z_{0v_bloc} values were returned when the flux footprints were applied. Therefore, only one set of values is presented for each station in Table 3.5.

Mean z_{0v_bloc} values for ice and snow surfaces, over all sites and seasons, were 3.1 mm and 0.6 mm, respectively, with strong persistence in site roughness values from one year to the next. A range of assumed footprint areas were also applied to the F_{D_local} maps to determine the effectiveness of the method in the absence of observed footprint data. Applying equal weighting to F_{D_local} values in a 101 x 101 m area directly upwind of a site (f_{c_100}) was found to return roughness values close to the z_{0v_bloc} and z_{0v_ec} values, in most cases (Table 3.5). As previously stated, the sensitivity of roughness length estimation to the selected block size was tested by varying the border thickness around the grid cell of interest. Overall, increasing the block area from 9 to 121 m² lead to an increase in estimated roughness length for a given footprint (~1 mm increase over ice and ~0.5 mm increase over snow, between 3 x 3 m and 11 x 11 m), with a border thickness of 1 cell (3 x 3 m block) returning roughness lengths closest to the EC-derived values.

Table 3.5. Momentum roughness length values (in mm) for each station estimated using remote methods (z_{0v_bloc} and z_{0v_prof}) from the LiDAR-derived DEMs. The roughness values for the prevailing downslope southerly wind direction are shown here. f_{c_100} represents values for an assumed 101 x 101 m upwind footprint where F_{D_local} values are given equal weighting. The uncertainty values from error propagation are shown for z_{0v_bloc} , while for z_{0v_prof} , $\pm\sigma$ of the roughness values for the 101 x 101 m upwind patch is presented.

z_{0v_bloc}	NG14		CG15-1		CG15-2		CG16-1		CG16-2	
	April	Sept	April	Sept	April	Sept	April	Sept	April	Sept
2014	-	6.3±0.9	-	2.5±0.1	-	2.5±0.5	-	1.6±0.4	-	0.5±0.2
2015	2.0±0.2	5.0±0.1	0.3±0.2	-	0.5±0.2	-	0.3±0.2	-	0.3±0.1	0.4±0.2
2016	2.5±0.1	4.0±0.4	0.6±0.3	4.0±0.4	0.8±0.2	3.2±0.5	0.3±0.1	1.6±0.5	0.4±0.1	0.4±0.1
f_{c_100}	2.0±0.2	3.2±0.4	0.5±0.2	4.2±0.2	0.6±0.2	2.1±0.5	0.2±0.1	0.9±0.4	0.2±0.1	0.2±0.1
z_{0v_prof}										
2014	-	6.9±0.3	-	2.6±0.2	-	2.0±0.3	-	2.1±0.2	-	0.4±0.02
2015	4.6±0.4	4.2±0.4	0.2±0.04	-	0.5±0.02	-	0.9±0.03	-	0.1±0.01	0.2±0.04
2016	3.6±0.2	5.6±0.1	0.6±0.1	5.6±0.5	1.7±0.1	7.1±0.6	0.7±0.03	2.6±0.2	0.1±0.02	0.6±0.04

Profile Method

The detrending and filtering of the surface height data, as shown in Figure 3.3, was performed for downslope profiles at each station site using the DEMs for all available years and seasons. Similar values for the cut-off wavelength ($\lambda_0 = 35$ m, approximately) were identified at each station site. z_{0v_prof} values were then estimated for each station location, and for each grid cell in a 101 x 101 m upwind area (Figure 3.10A), from all corresponding DEMs. Table 3.5 presents the z_{0v_prof} values for each station and LiDAR flight. Mean z_{0v_prof} values for ice and snow surfaces, over all sites and seasons, were 4.3 mm and 1.1 mm, respectively. Where repeated over the same location, the z_{0v_prof} values displayed substantial differences from one year to the next over ice surfaces

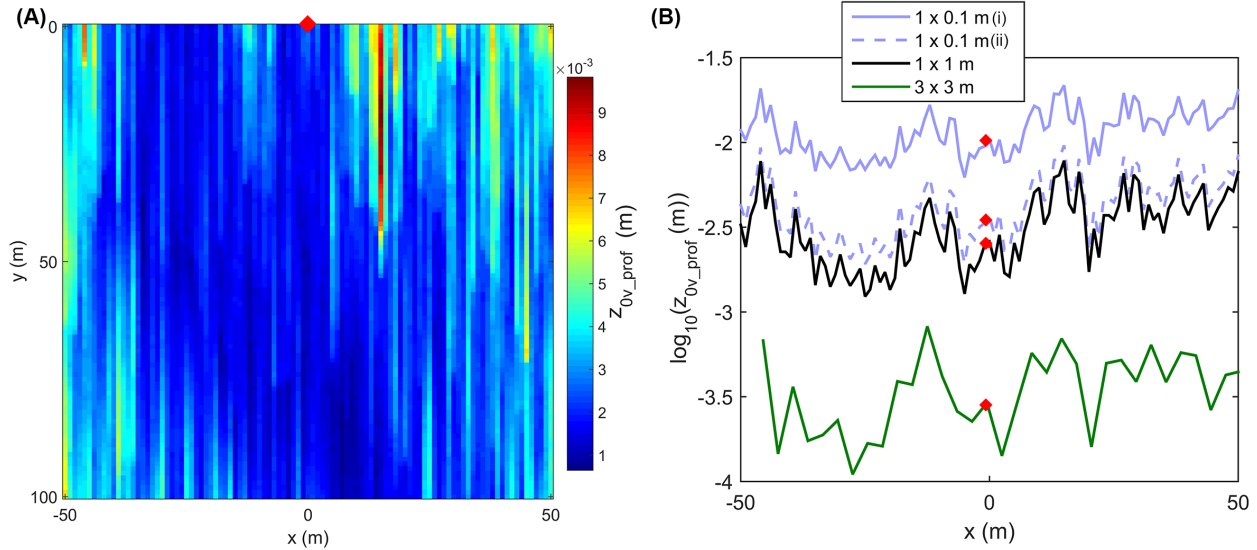


Figure 3.10. (A) z_{0v_prof} values estimated for each grid cell in a 101 x 101 m area upwind from CG16-1 (red diamond) from the September 2016 DEM of Conrad Glacier. (B) z_{0v_prof} values derived for the downslope profiles at CG16-1 ($x = 0$) and for the grid cells 50 m to the east and west of the station from the original DEM (1 x 1 m), and from the higher (1 x 0.1 m) and lower (3 x 3 m) resolution DEMs constructed for sensitivity testing. The 1 x 0.1 m (i) values are from the initial high resolution DEM used in the sensitivity test, while the DEM used for 1 x 0.1 m (ii) had the amplitude of the synthetic microtopography profiles reduced by a factor of 10.

(up to 5 mm), in contrast to the noted z_{0v_bloc} persistence.

Figure 3.10B displays the z_{0v_prof} values derived for the downslope profiles from the original DEM (1 x 1 m), and from the higher (1 x 0.1 m) and lower (3 x 3 m) resolution DEMs constructed for sensitivity testing. Roughness values are presented for the station location at CG16-1 and for the grid cells 50 m to the east and west of the station. The same pattern of spatial variability in z_{0v_prof} across the grid cells was captured with each DEM, but with substantial differences in magnitude. On average, the 3 x 3 m DEM yielded z_{0v_prof} values one order of magnitude smaller than the original 1 x 1 m DEM. This result is expected since the original surface

has been smoothed, and the relevant scales of the roughness elements may not be adequately resolved in the 3 x 3 m DEM. Applied to the 1 x 0.1 m DEM, the profile method yielded roughness values, on average, a half order of magnitude larger than those for the 1 x 1 m DEM. The primary reason for differences in z_{0v_prof} values with changing DEM resolution was the difference in s values (Equation 3.10). While h^* values remained almost unaltered for different resolutions, the s values changed by > 50%, resulting in large changes in z_{0v_prof} . The first-order estimate of surface variability from the microtopography survey may overestimate the variability in the downslope wind direction. To test for this, the amplitude of the synthetic microtopography profiles was reduced by a factor 10 (from dm to cm scale) and z_{0v_prof} recalculated. The resulting roughness length values were reduced and matched more closely the original z_{0v_prof} from the 1 x 1 m DEM, however, still yielding up to 10% larger values than original (Figure 3.10B).

In Situ vs Remote Methods

The estimates from both DEM-based roughness methods were compared with the EC-derived values (Figure 3.11 and Table 3.6). In cases where LiDAR data were not available from the same year a station was in place, the averages of the roughness estimates from the two other years were utilised for the comparison. Overall, estimates from both DEM-based roughness methods provided values for ice and snow surfaces in line with previous observations on glacier surfaces (Brock *et al.*, 2010), and were generally within 2 mm and 0.2mm (< half order of magnitude) of the corresponding z_{0v_ec} observations over ice and snow, respectively. Over ice surfaces, the z_{0v_bloc} values were slightly smaller than the corresponding z_{0v_prof} values (mean values of 3.1 mm and 4.3 mm, respectively), and tended to align more closely with the z_{0v_ec} estimates (mean of 2.3

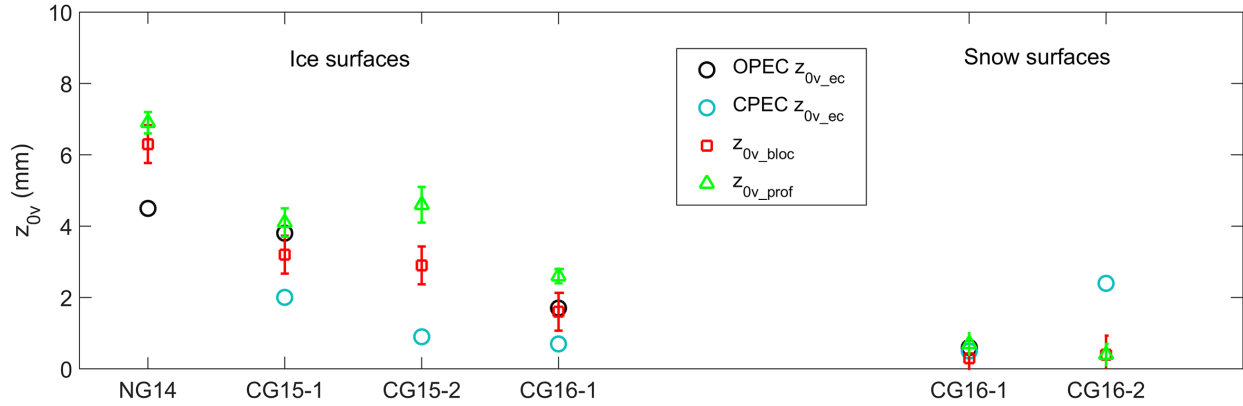


Figure 3.11. Comparison of geometric mean OPEC and CPEC momentum roughness length observations with z_{0v_bloc} and z_{0v_prof} estimates from the remote methods. Values are separated into ice and snow surface types. Error bars represent the calculated uncertainty in the z_{0v_bloc} method, and σ of the z_{0v_prof} values for an 101 x 101 m upwind patch. The standard deviation on each of the mean z_{0v_ec} values (see Table 3.4) extends beyond the y-axis range.

Table 3.6. Comparison of momentum roughness length values (in mm) for each station, as observed from the EC systems (z_{0v_ec}), and as estimated using the DEM-based methods (z_{0v_bloc} and z_{0v_prof}). *For years where LiDAR data was not available from the same year a station was in place, the averages of the roughness estimates from the two other years were utilised for evaluation.

	NG14 OPEC	CG15-1 OPEC	CG15-1 CPEC	CG15-2 CPEC	CG16-1 OPEC	CG16-1 CPEC	CG16-2 CPEC
	ice	ice	ice	ice	snow	ice	snow
z_{0v_ec}	4.5	3.8	2	0.9	0.6	1.7	2.4
z_{0v_bloc}	6.3	3.2*	3.2*	2.9*	0.3	1.6	0.4
z_{0v_prof}	6.9	4.1*	4.1*	4.6*	0.7	2.6	0.4

mm). For the snow surface at CG16-2 in the accumulation zone, the mean roughness lengths from both DEM methods (0.4 mm) substantially underestimated the z_{0v_ec} value (2.4 mm). Potential causes for this deviation will be discussed in Section 3.5.1. For the transitional snow/ice surface

present at NG14 during the first four days of observations, the z_{0v_bloc} and z_{0v_prof} values from the July 2014 flight (4.5 mm and 6.8 mm) aligned more closely with the mean z_{0v_ec} value for ice over the season (4.5 ± 28.8 mm) than with the z_{0v_ec} value obtained during the four day period (0.5 ± 3.0 mm). The mean z_{0v_ec} value for this period, however, was based on a very limited number of EC observations after filtering ($n=16$) with substantial scatter.

3.4.3 Wind Direction and Momentum Roughness Length

The 30-minute EC data and the rotated z_{0v_prof} values were used to examine the influence of wind direction on the effective roughness length at each location. It should be restated at this point that the z_{0v_ec} values had been filtered to remove values when wind direction was beyond $\pm 45^\circ$ of the main axis of the EC sensor to minimise the influence of flow distortion due to the station structure. Therefore, only a limited direction window is available in the z_{0v_ec} data over which to examine this dependence. For the ice surface of CG16-1, z_{0v_ec} values were observed to increase and become more scattered as the wind direction veered towards the southwest, a pattern that was also detected in the z_{0v_prof} (Figure 3.12A). Similar behaviour was noted at the same location in 2015 (CG15-2), with greater variation in z_{0v_ec} with wind direction (Figure 3.12B). The rotated z_{0v_prof} values were also used to examine a wider angle of wind direction than was possible with the z_{0v_ec} data. Figure 3.13 displays the z_{0v_prof} values in 5° increments in wind direction between 180° and 270° for an April (snow) and September (ice) surface at each station. The magnitude of roughness length variation with direction was greatest over ice surfaces. For the three stations in Conrad's ablation zone, z_{0v_prof} was observed to increase as wind direction approached a cross-glacier

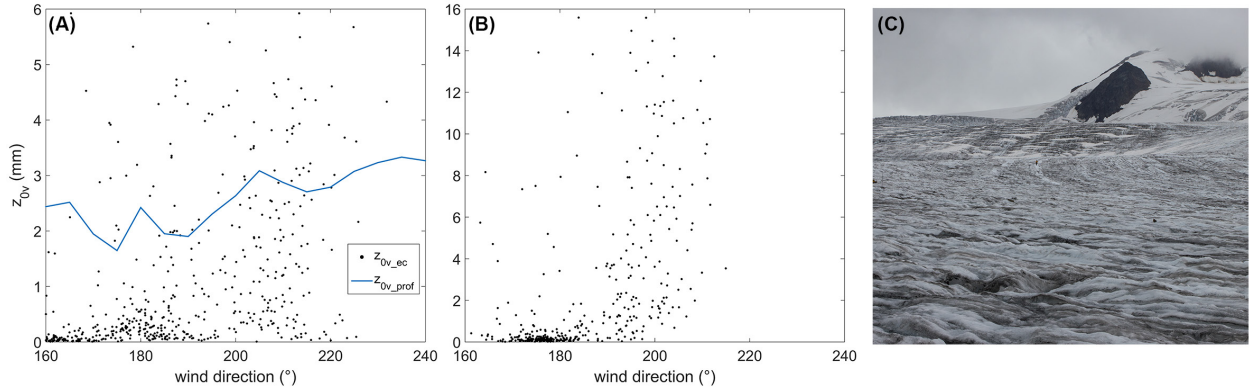


Figure 3.12. Dependence of momentum roughness length on wind direction for (A) z_{0v_ec} (filtered 30-minute values) and z_{0v_prof} at CG16-1, and (B) z_{0v_ec} at CG15-2 (LiDAR data was not available for CG15-2 during this period). (C) Elongated roughness features on Conrad glacier, looking south from CG15-1 in July 2015. Meltwater channels had dimensions of 0.5–1 m in width and 0.1–0.2 m in depth, with substantial variability.

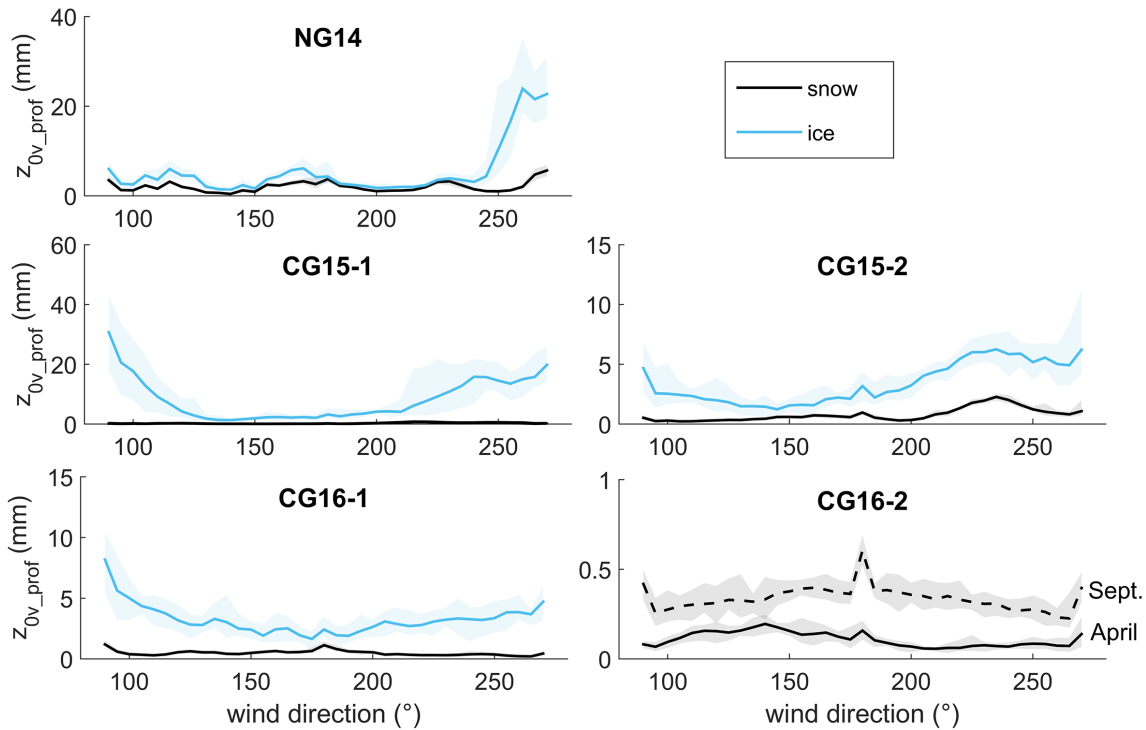


Figure 3.13. Roughness values from rotated z_{0v_prof} method for 5° increments in wind direction between 90° and 270° for April (snow) and September (ice) surfaces (snow surface at CG16-2 for both periods). Shaded area represents range of roughness lengths estimated for five profiles either side of the station (11 profiles).

orientation (east or west), while at NG14, a pronounced increase in roughness was noted over the ice surface at 240°. The snow surfaces at CG16-2 in April and September presented very similar roughness profiles with wind direction, with slightly larger z_{0v_prof} in the autumn. The apparent peaking in z_{0v_prof} over CG16-2 at 90°, 180°, and 270° is likely the result of an artificial reduction in roughness at all other angles due to the smoothing of the DEM when the height values were bilinearly interpolated to the rotated grid. The roughness values at 90°, 180°, and 270° are calculated from the original DEM, without the need for interpolation, and the effect of this appears to be most visible in the smaller magnitude z_{0v_prof} values over the snow surface.

3.5 Discussion

3.5.1 Spatial and Temporal Variability of z_{0v}

Ice Surfaces

Variation in both the z_{0v_ec} and DEM-based roughness length values was noted across test sites with a melting glacier ice surface (e.g. 4.5 mm and 0.7 mm for mean z_{0v_ec} at NG14 and CG16-1, respectively). An assumed z_{0v} value for ice (e.g. 1mm), applied uniformly to all locations in this study, would have substantially misrepresented the surface roughness characteristics, and the resulting turbulent flux parameterisations. In the case of NG14, implementing the commonly assumed z_{0v} value for ice of 1 mm in the bulk parameterisation of turbulent heat fluxes, rather than the mean observed value of 4.5 mm, would result in a ~20% reduction in the mean estimated fluxes. Furthermore, stations throughout the study were installed in secure regions of the glaciers with relatively smooth and uniform surfaces, and away from crevasse fields and glacier margins where the surface drag on airflow would be higher (Figure 3.8). Therefore, the true range of

roughness length values over the entire surface of the study glaciers would be greater than that represented by the values estimated for the station locations. Smith *et al.* (2016) detected a z_{0v} range of over three orders of magnitude across a small ($\sim 1 \text{ km}^2$) mountain glacier (Kårsaglaciären in Sweden).

Over the study period, the mean momentum roughness length estimates for ice at each site showed little temporal variance from one year to the next. This persistence in seasonal ice roughness values may allow for the use of z_{0v} estimates from pre-existing EC or DEM campaigns at a site of interest. The period of validity of these estimates may vary, however, depending on the surfaces processes of each glacier. Within a single melt season, changes in momentum roughness length due to the evolution of the ice surface with time were not evident in the $z_{0v_{ec}}$ values (Figure 3.6A). Previous glacier roughness studies (e.g. Sicart *et al.*, 2014) have also noted persistence in z_{0v} despite extensive ice melt. Smith *et al.* (2016) noted that this persistence was most evident over ice surfaces with defined melt features, such as supraglacial channels, similar to the ice surfaces of this study. There was substantial scatter observed in the 30-minute $z_{0v_{ec}}$ values that is likely unrelated to changes in surface roughness. While estimated using EC-observed data, the $z_{0v_{ec}}$ calculations are still derived from the bulk aerodynamic method (Equation 3.1). Extensive filtering was applied to $z_{0v_{ec}}$ values, in particular, to avoid uncertainty in the bulk method due to non-neutral stability conditions. However, using a filter that allows values from near-neutral conditions ($-0.1 < \frac{z}{L_{ec}} < 0.2$) rather than strictly neutral, only ($\frac{z}{L_{ec}} = 0$), may introduce some uncertainty and variability to the $z_{0v_{ec}}$ estimates. Furthermore, previous studies have suggested that some assumptions of the bulk method, namely, constant friction velocity and turbulent flux values with height, may not be valid during katabatic conditions with shallow

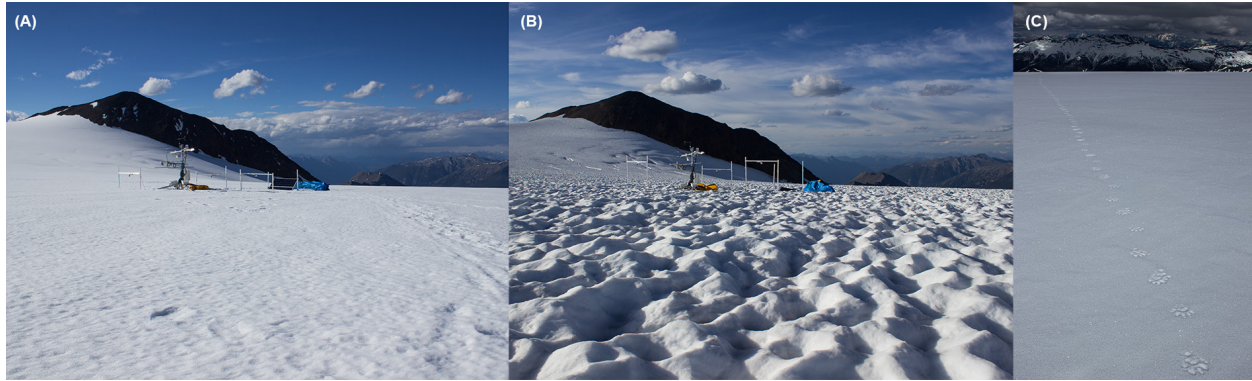


Figure 3.14. Observed snow surface roughness variations at CG16-2 from camera imagery for (A) June 30th – July 3rd ($z_{0v_ec} = 1.0 \pm 4.2$ mm), and (B) Aug. 19th – 21st ($z_{0v_ec} = 9.6 \pm 21.7$ mm). For scale, the upper crossarm of the AWS is at a height of 1.9 m. (C) Smooth snow surface observed at the location of CG16-2 on April 26th, 2016 (wolverine tracks for scale).

wind maximums, which can develop frequently over sloped glaciers (e.g. Denby and Smeets, 2000).

Snow Surfaces

Large differences in z_{0v} between sites were also noted in this study for snow-covered surfaces. The annual persistence in roughness values observed over ice was also present in the snow surface values, with similar z_{0v_bloc} values returned for the same time each year when repeated at the same location. Where both *in situ* and remote values over snow surfaces were available, agreement between z_{0v_ec} and the DEM-obtained roughness values varied substantially. In the case of CG16-2, which had a snow-covered surface throughout, the relatively large mean z_{0v_ec} value (2.4 ± 16 mm) was substantially greater than z_{0v_bloc} and z_{0v_prof} (both 0.4 mm). This difference may be due to the temporal variance in roughness of a snow surface within a melt season (as observed in

Figure 3.6B), and the difference in observation time between the EC and LiDAR data. Images from the time lapse camera installed at CG16-2 (Figure 3.14A-B) illustrate the variety in roughness conditions of the snow surface at that site. Two periods were selected with visually apparent roughness differences and an adequate number of 30-minute z_{0v_ec} observations; a moderately smooth, melting snow surface (June 30th – July 3rd; 78 observations), and a rough, sun-cupped surface (Aug. 19th – 21st; 38 observations). Examining the z_{0v_ec} values, an order of magnitude difference was noted between the mean values for the moderately smooth (1.0 ± 4.2 mm) and rough (9.6 ± 21.7 mm) snow surfaces. In view of this short-term variability in snow roughness, the z_{0v_bloc} and z_{0v_prof} values, derived from LiDAR flights in April and September, cannot be considered comparable to the z_{0v_ec} values from the summer. Imagery taken in the same location as the station site a few days after the April LiDAR flight (Figure 3.14C) show a very smooth snow surface. With fresh snowfall in late August and September, a similar surface was likely present during the second flight, resulting in the small DEM-based values returned. Relatively large z_{0v_bloc} and z_{0v_prof} values were obtained for NG14 during the April LiDAR flights, possibly in response to a rough snow surface. Comparable *in situ* imagery of the site was not available for these periods, however. The effect of the size of the roughness elements on a melting snow surface is discussed further in Section 3.5.2.

Wind Direction

Evidence of roughness length dependence on wind direction was observed in the 30-minute EC data at some locations, and in the rotated z_{0v_prof} values, also. The strongest dependence on wind direction in the z_{0v_ec} values was noted for the ablation zone of Conrad Glacier, at the location of

CG15-2 and CG16-1. Elongated roughness features, including meltwater channels, were present on the surface during these observations, with the orientation of their long axes pointing in a southeast to northwest direction (Figure 3.12C). As the wind veered to the southwest, airflow became perpendicular to the faces of these features, likely resulting in increased form drag, which produced the larger roughness lengths observed. The rotated z_{0v_prof} values for the three stations in Conrad's ablation zone revealed an increase as wind direction approached a cross-glacier orientation. At NG14, the pronounced increase in roughness over the ice surface at 240° was likely due to a crevasse field to the west of the station. This feature was not evident in the April values, suggesting snow cover had smoothed the surface in that region. Dependence of momentum roughness length on wind direction has been observed in several other glacier studies (e.g. Munro, 1989; Brock *et al.*, 2006; Smith, 20014). Over all seasons and locations in this study, wind direction was found to be within 45° of the mean slope angle for approximately 93% of the time. This persistent, katabatic downslope wind is a common feature in glacial boundary layers, and as a result, will substantially reduce the influence of surface roughness anisotropy on the variation in the effective roughness lengths and mean generated turbulence.

3.5.2 Performance of DEM-based z_{0v} Estimation

The methods developed here for remotely estimating z_{0v} were found to return roughness length values within 1–2 mm (\ll an order of magnitude) of those determined from *in situ* EC measurements, and were shown to respond to changes in surface cover from snow to ice. Using a DEM with a 1 x 1 m grid cell appears to resolve the length scales influencing z_{0v} on the ice surfaces of this study. With a dense distribution of roughness elements (Figure 3.12C), the previously mentioned effects of wake-interference and skimming of the airflow over the ablating ice may

have reduced the influence of the smaller roughness elements on z_{0v} , as noted in previous studies (e.g. Wieringa, 1993; Smeets *et al.*, 1999). During the April flights over Conrad Glacier, the DEM methods returned roughness values in line with previous observations over smooth, fresh or compacted snow surfaces (Brock *et al.*, 2006). Over rough, undulating snow surfaces, larger-scale features will have the dominant influence on roughness length (Fassnacht *et al.*, 2009), and are potentially resolvable in the utilised DEM, as may have been the case with the April values for NG14. Between these scales, however, it is likely that the roughness elements influencing z_{0v} are not resolvable with a 1 x 1 m grid cell, making the usefulness of these methods over a melting snow surface uncertain (in addition to the temporal variation discussed in Section 3.5.1).

The profile method developed here has been shown to return values in line with *in situ* estimates of the momentum roughness lengths without the need for the assumptions employed by the block method. The value of the selected cut-off wavelength ($\lambda_0 = 35$ m) is likely similar to the height of the stable boundary layer over the glacier sites, and may indicate the upper scale of the surface features that this shallow flow is impeded by. The z_{0v_prof} values did show a tendency towards overestimation, relative to the z_{0v_ec} values. In addition, the persistence between seasons in roughness length, noted in the z_{0v_ec} and z_{0v_block} values, was less evident in the z_{0v_prof} values, suggesting that the profile method is sensitive to changes in small scale features which may not have a substantial influence on the observed (z_{0v_ec}) roughness values. The profile method also displayed sensitivity to the choice of DEM resolution, arising from substantial differences in the estimate of s (Equation 3.10) for different resolutions (>50% difference between 1 x 1 m and 1 x 0.1 m resolutions). This sensitivity is to be expected for methods dependent on estimates of the surface derivative (s is effectively an integral of the surface derivative). While profiles taken in

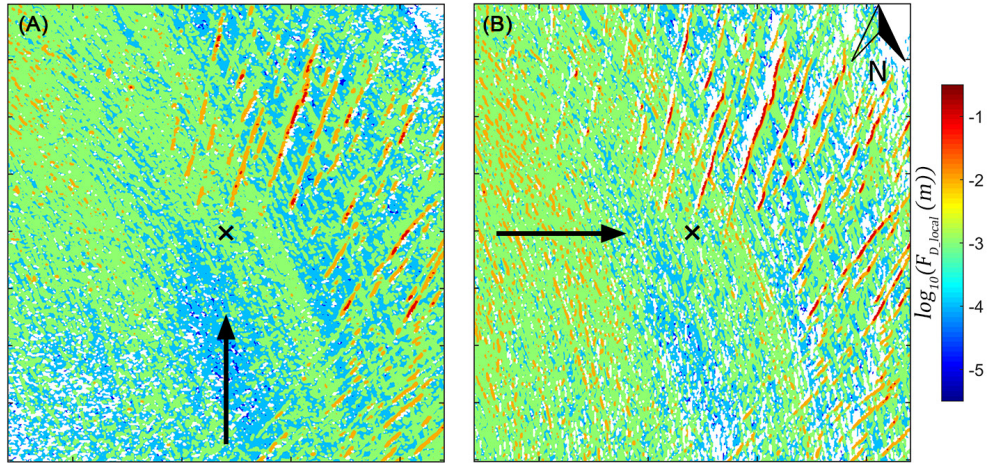


Figure 3.15. Comparison of the F_{D_local} values from the block method for (A) southerly (downslope) and (B) westerly (cross-slope) wind direction at CG16-1 in September 2016. Air flow (black arrow), and AWS location (black cross) are also identified.

two different resolutions may have similar absolute values and variance, the derivatives of these profiles (dh/dy) can be substantially different.

The block estimation method returned roughness length values that were smaller than those from the profile method, and more in line with mean z_{0v_ec} , in general. The technique used in the z_{0v_bloc} method to calculate s across overlapping block areas (Figure 3.2 and Equation 3.7) was developed in an effort to account for the shadowing of elements from airflow by upwind features. Rather than assuming that each feature above the mean surface has an additive influence on roughness length, as done in the z_{0v_prof} method (below the cut-off wavelength) and other profile-based methods (e.g. Munro, 1989; Arnold and Rees, 2003), the relative height differences and potential sheltering influence of neighbouring features in the block are considered. On glacier surfaces, where elongated roughness features such as melt channels are common, the block approach may also help account for the channelisation of air flow and the shadowing of the

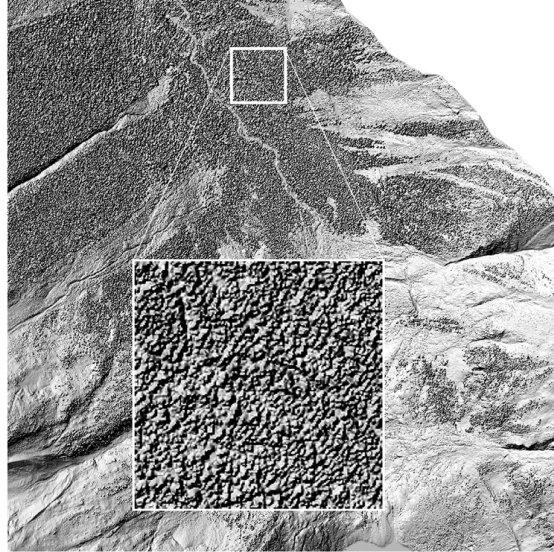


Figure 3.16. DEM of a 200 x 200 m area (white box) of coniferous forest to the east of Conrad Glacier used for estimating z_{0v_bloc} (1.28 m).

roughness element by the upwind continuation of the feature, which in turn, may reduce the effective roughness length. The response of the block method to this effect can be seen when the F_{D_local} estimates for the southerly (downslope) wind direction are compared with those for the westerly (cross-slope) wind direction (Figure 3.15). Drag values estimated for the meltwater channels on the surface are lower when air flow is close to parallel to these features, and higher when air flow is perpendicular to the channels. This effect may have led to the smaller z_{0v_bloc} values, relative to the z_{0v_prof} values. When implemented with an assumed turbulent footprint, the block method returned roughness length values that were very similar to those calculated using a footprint modelled from EC data, indicating the potential for its use where turbulence observations are unavailable. To apply the block approach, a number of additional assumptions were required, however. The choice of grid cell and block size corresponds to an assumption on the size of the dominant roughness elements influencing z_{0v} on the glacier surface, and an assumption on the

range of a feature's shadowing effect. The downwind shadowing and wake effects generated by a feature will likely vary with wind speed, and this variation is not accounted for here. The optimal block size may vary between locations and wind regimes, and require tuning for application to other surfaces. Over the range of surfaces in this study, however, a 3 x 3 m block was observed to be optimal, and to respond to changes in surface roughness due to snow and ice cover. As a test of robustness, z_{0v_bloc} values were also estimated for a region of forest captured in the LiDAR data (Figure 3.16). This forest was located on a valley floor to the east of Conrad Glacier, and consisted of tall (~20 m), coniferous trees. The z_{0v_bloc} value for a 200 x 200 m subarea within this forest was 1.28 m. This value is in line with existing z_{0v} measurements over coniferous forest (Wieringa, 1993). While the z_{0v_bloc} method (including the LiDAR data utilised) is not configured nor intended for use over forestry, this test indicates that its configuration (including selected block size) is responsive to a range of roughness element sizes, beyond the scale of those encountered on the glacial surfaces of this study.

3.5.3 Scalar Roughness Relationships

Whilst displaying similar mean values over the entire dataset (0.05 mm for z_{0t_ec} and 0.11 mm for z_{0q_ec}), the scalar roughness lengths differed substantially from each other when examined on a site-by-site basis. There was no evidence of a consistent ratio between z_{0t_ec} and z_{0q_ec} , with their seasonal means ranging above and below each other by up to an order of magnitude. Between the momentum and scalar roughness lengths, seasonal z_{0t_ec} displayed a more consistent relationship with z_{0v_ec} , being approximately one and a half orders of magnitude smaller than z_{0v_ec} in most cases. This relation did not hold for NG14 and CG16-2, however, and between z_{0v_ec} and z_{0q_ec} ,

there was no persistent ratio. Calanca (2001) observed z_{0t} to be a function of the temperature gradient between the air and a melting ice surface, while Park *et al.* (2010) found a relation between relative humidity at 2 m height and z_{0q} . In this study, variation in the scalar roughness lengths was compared with fluctuations in air temperature gradient and relative humidity, but no dependent relationship was evident. The surface renewal model of Andreas (1987), where the ratio of momentum to scalar roughness was expressed as a function of R_* , showed relatively good performance, particularly for seasonal values of z_{0t} . If momentum roughness length values have been obtained for a given surface (through remote or *in situ* methods), this model appears to be the best available method for estimating the scalar values.

3.6 Conclusions

Over three melt seasons, *in situ* and remote methods were implemented to determine the momentum and scalar roughness lengths on the surface of two glaciers in the Purcell Mountains of British Columbia, Canada. EC sensors were employed to obtain continuous *in situ* measurements throughout each melt season, while LiDAR-derived DEMs were utilised in the development of two remote estimation techniques. Seasonal mean momentum roughness length values, estimated from eddy covariance observations at each location, ranged from 0.7–4.5 mm for ice surfaces, and 0.5–2.4 mm for snow surfaces. For representative turbulent flux modelling, this study suggests that site-specific z_{0v} values are necessary for glacier surfaces. From year-to-year, z_{0v} values were noted to remain relatively consistent at a given location (<0.2 mm difference between seasonal mean values). Within a melt season, continuous EC observations and camera imagery noted greater temporal variation in roughness for snow surfaces than for ice. These

findings indicate that site-specific z_{0v} values on an ice surface may be valid to implement over multiple melt seasons, while over snow surfaces, the utilised roughness values require intraseasonal updating. Wind direction was also noted to affect z_{0v} variability where elongated features such as melt channels dominated the surface topography. Persistence in wind direction on sloped glacier surfaces, however, reduces the influence of this variability.

Observations of the scalar roughness lengths differed substantially from the corresponding momentum values, showing considerable variation between location and season, and little agreement with fixed ratios commonly assumed with z_{0v} . In general, the Andreas (1987) surface renewal method showed agreement with the observed ratios between EC-derived scalar and momentum roughness lengths, and would seem to be the appropriate method to implement where continuous EC observations are not available, but site-specific z_{0v} values have been established.

The DEM-based methods described in this study were shown to perform well over most surfaces, differentiating between ice and snow cover, and returning momentum roughness values that were within 1–2 mm (\ll an order of magnitude) of EC-derived values for the corresponding footprints. Both the block and profile methods could be employed together in future studies to constrain a likely range for z_{0v} . Over ice surfaces, the employed assumption that the features dominating surface roughness were of a scale resolvable using a 1 x 1 m grid cell appears to be valid. This may allow for the potential upscaling of these methods with high resolution satellite imagery, greatly expanding the number of glaciers for which roughness length estimates could be obtained. Furthermore, the observed persistence in seasonal mean z_{0v} values for a given ice surface may allow for DEM-based estimates to be assumed valid over more than one season. z_{0v} estimates were found to be sensitive to DEM resolution, and evaluation of the proposed remote methods over a wider range of resolutions and surface height data sources (e.g. photogrammetry,

microtopography) is recommended. Over melting snow surfaces, the validity time of a retrieved DEM is reduced due to the discussed temporal variability in roughness, and as a result, the estimated roughness lengths may quickly become unrepresentative. In addition, the roughness features observed to develop on melting snow in this study may not be resolvable using a 1 x 1 m grid cell, and further testing over snow, with simultaneous *in situ* and remote observations, would be useful.

Chapter 4:

Constraining the role of turbulent heat flux in glacier surface energy balance and its parameterisation for katabatic surface layers

4.1 Summary

As an important component of glacier SEB, variation in the magnitude of the turbulent heat fluxes will have a substantial influence on surface melt rates, motivating the need to understand the extent and cause of such variation. The role played by atmospheric stability in turbulent flux generation and variation is poorly understood for glacier surfaces, with considerable uncertainty in commonly used stability corrections for flux parameterisation. Katabatic surface layers, which can form frequently over sloped glacier surfaces, can have different wind shear and flux profiles to the surface layers for which such stability functions were developed, potentially invalidating their use in these conditions. A multi-year observation campaign was carried out on two glaciers, where continuous observations of the complete SEB, including the turbulent heat fluxes, were obtained at multiple locations. The turbulent fluxes were observed to be important components of the SEB at each location, providing 31% of seasonal melt energy on average, and up to 78% of melt energy on individual days. Substantial variation was observed in the daily and sub-daily magnitude of the turbulent fluxes over the course of a season, with large differences in magnitude between ablation

and accumulation zones (65%), underlining the need for accurate flux estimation in distributed SEB and ablation applications. Turbulent heat flux estimates from two commonly used bulk parameterisation methods (one assuming neutral atmospheric stability, the other using a stability correction based on the Monin-Obukhov length) were compared with eddy covariance observations. The performance of both methods was found to be sensitive to the occurrence of a katabatic, low-level wind maximum close to measurement height, and a metric was developed to help identify these conditions. The observed reduction in friction velocity in the vicinity of a wind maximum was not captured in the bulk method, leading to overestimation in the modelled fluxes. Furthermore, this variation in the wind shear profile through a shallow katabatic surface layer invalidates the application of the tested bulk methods, which are derived assuming constant friction velocity with height. In katabatic environments with frequent development of a low-level wind maximum, it is suggested that correcting for the associated changes in the wind shear profile should take precedence over the application of existing stability functions which have been shown to be unreliable in these conditions.

4.2 Introduction

Turbulent heat fluxes have been observed to be important contributors to the SEB of mountain glaciers (e.g. Hock and Holmgren, 1996; Greuell and Smeets, 2001; Fitzpatrick *et al.*, 2017). Variation in the magnitude of the turbulent heat fluxes will, therefore, have a substantial influence on surface melt rates. This emphasises the need for accurate estimation of these energy terms in ablation models, and an understanding of the drivers of turbulent heat flux variability on glaciers. The roughness lengths have been shown to vary substantially from one location to the next (e.g. Van den Broeke *et al.*, 2005; Brock *et al.*, 2010), and as an important control on turbulent flux

generation, to require accurate representation in the bulk aerodynamic method (as discussed in Chapters 2 and 3). Atmospheric stability is generally recognised as another primary modulator of turbulent heat flux. As has been identified in previous studies, however, uncertainty remains regarding the magnitude and mechanism of this influence over sloped glaciers, and the validity of the stability corrections commonly applied when parameterising the fluxes for such surfaces (Denby and Greuell, 2000; Grisogono and Oerlemans, 2001; Fitzpatrick *et al.*, 2017; Radić *et al.*, 2017).

The bulk aerodynamic method assumes that the profiles of wind, temperature, and water vapour in the boundary layer are logarithmic with height. This assumption has been shown to be valid only during neutral atmospheric stability conditions (Stull, 1988), and as a result, corrections are commonly applied to adjust the turbulent fluxes for non-neutral boundary layers. The theories and empirical data used for developing these stability functions were obtained from studies over flat terrain (e.g. Monin and Obukhov, 1954; Dyer, 1974; Holtslag and De Bruin, 1988; Beljaars and Holtslag, 1991), and generally assume that turbulence generation will be suppressed (enhanced) in stable (unstable) conditions. For the parameterisation of turbulent heat fluxes on Nordic Glacier (Section 2.5.4), assuming neutral atmospheric conditions, or using a stability correction based on the Obukhov length (L), led to overestimated fluxes when compared with EC observations, with peaks in overestimation corresponding with stable, katabatic conditions (Figure 2.10). Similar behaviour has been noted in studies on other glaciers (e.g. Radić *et al.*, 2017).

A number of previous studies have examined reasons for the failure of existing bulk methods and stability functions based on Monin-Obukhov similarity theory, and give an indication as to why they may not be suitable for application over a glacier surface. To begin with, observations over the flat surfaces for which the stability corrections were developed (e.g. Holtslag

and De Bruin, 1988; Holtslag *et al.*, 2014) have shown poor performance of the original functions during periods with very stable stratification ($\frac{z}{L} > 1$); conditions which can frequently occur over a melting glacier (Cuffey and Paterson, 2010). Furthermore, glacier surfaces are rarely flat. A sloped surface, combined with stable stratification, can lead to the development of a katabatic wind. During seasons when air temperatures are warmer than the surface snow or ice, cooling of the air close to the sloped surface generates a horizontal density gradient, which drives a layer of downslope air flow (Oerlemans and Grisogono, 2002). Within this katabatic flow, the height of the maximum wind speed is often close to the surface, with wind speed maximums observed below standard measurement height (2 m) on even relatively gentle slopes ($\sim 4^\circ$) (Denby, 1999). The structure of a surface layer with a low-level wind maximum (LLWM) can differ greatly from that of a stable surface layer over a flat surface (Van Der Avoird and Duynkerke, 1999). Wind shear, represented in the bulk method through friction velocity (u_*), will diminish to zero as the height of a wind maximum is approached, as will the momentum flux and the mechanical production of turbulence (Denby and Greuell, 2000). A key assumption of Monin-Obukhov similarity theory is that the turbulent fluxes change by less than 10% through the height of the surface layer in which it is being applied, allowing for the assumption of constant flux and u_* values through this layer (Oerlemans and Grisogono, 2002). In the presence of a shallow, katabatic flow, strong gradients must exist in momentum flux between the surface and the region of zero wind shear at the LLWM. The closer to the surface a LLWM is, the more suppressed the constant momentum flux layer will be, limiting the region in which the theory will be valid (Denby and Smeets, 2000). Denby and Greuell (2000) note that this reduction in momentum flux may lead to an increase in the temperature gradient (relative to a logarithmic profile) due to reduced mixing as a LLWM is approached from below. This may potentially balance the loss of mechanical turbulence

generation, and allow for the assumption of constant sensible heat flux magnitude through the surface layer.

In this chapter, the results of a multi-year, glacier SEB observation campaign will be analysed to improve understanding of the topics described above. The contribution of the turbulent heat fluxes to the SEB at a series of test sites will be quantified, and the variation of this contribution between locations and over different timescales will be examined. The performance of common parameterisation methods and stability schemes in estimating these fluxes will be assessed for each period and location, and variation in this performance will be compared with differences in corresponding atmospheric conditions and surface slope angles. Focus will be given to the detection of katabatic LLWMs, and the influence of these regimes on turbulence parameterisation performance. Friction velocity estimates from the bulk method will be compared with observed values during these conditions, and the effects of a non-constant wind shear profile on the parameterised fluxes will be explored.

4.3 Data and Methods

4.3.1 Field Campaign

Observation data were obtained from a field campaign carried out on Nordic and Conrad glaciers in the Purcell Mountains of British Columbia over the 2014–2016 melt seasons (described in detail in Sections 2.4 and 3.3). A total of five station deployments were executed over the three seasons (see Figure 3.1 and Table 3.1); one in the ablation zone of Nordic (NG14), three in the ablation zone of Conrad (CG15-1, CG15-2, and CG16-1), and one in Conrad’s accumulation zone (CG16-2). The five locations were selected so as to facilitate a comparison of SEB and the role of turbulent heat flux between multiple sites and temporal scales. As noted in Chapter 3, the surface conditions,

in terms of snow/ice coverage and roughness, varied between sites. In addition, there were differences in the mean surface slope angle of the station locations; 13° towards the northeast at NG14, 8° towards the north at the three stations in Conrad's ablation zone, and 3° towards the northeast at CG16-2.

4.3.2 AWS

The design and installation of the AWS developed for this project has been described in detail in sections 2.4 and 3.3. The sensor payload evolved from season to season, and an instrument list for each station, including height of installation and sensor accuracy, is provided in Table 3.2. A CPEC system was added to both stations for 2015 and 2016, helping to minimise gaps in the turbulence dataset due to precipitation, and to facilitate a comparison of the performance of open and closed path eddy covariance systems in a glacial environment. Where OPEC and CPEC systems were present on the same station (CG15-1 and CG16-1), good agreement was observed between flux observations (Figure 4.1), with the OPEC systems showing a tendency to return smaller flux values, on average (-8%). Other major additions to the original design deployed in 2014 include aspirated radiation screens for the temperature and relative humidity probes, infrared surface temperature sensors, and an increase in sonic ranger units from one to three per station.

In addition to the main stations, an array of air temperature and humidity probes were installed along the midline of Conrad Glacier during the 2016 melt season (Figure 4.2A) to measure the near-surface lapse rate. Six probes in total (each housed in a radiation screen) were deployed between 1,900 m and 3,000 m elevation; one on each of the two main station structures, and a further four on independent masts (Figure 4.2B) designed to lower with the melting surface and maintain a constant height of the probes (~1.6 m). Prior to deployment, the probes were

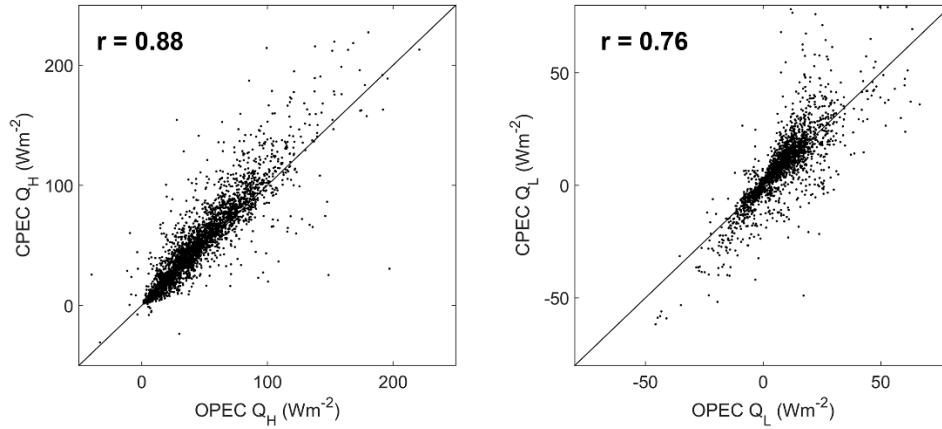


Figure 4.1 Comparison of the turbulent heat fluxes as observed by the OPEC and CPEC sensors on CG16-1.

Similar behaviour was noted for the OPEC and CPEC comparison at CG15-1.

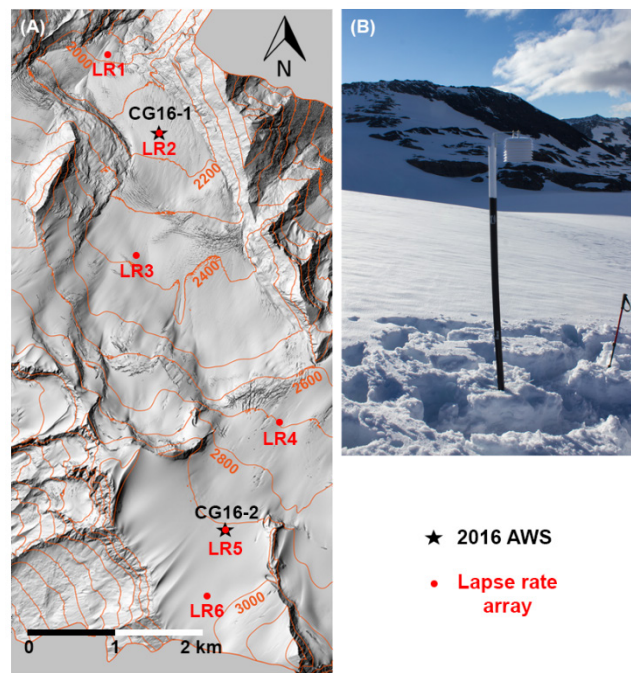


Figure 4.2. (A) Array of air temperature and humidity probes installed on Conrad Glacier during the 2016 melt season to measure the near-surface lapse rate. (B) Four of the probes were installed on independent masts designed to lower with the melting surface and maintain a constant height of the probes (~1.6 m).

operated side-by-side in a lab environment for one week to identify any mean differences in observed values, and to ensure comparable measurements. The mean temperatures of the probes were within a 0.09°C range over the calibration period, with a maximum 30-minute difference between any two probes of 0.1°C .

4.3.3 Data Treatment and SEB Analysis

The raw observations from the EC systems, radiation sensors, air temperature probes, rain gauges, and sonic rangers were processed following the steps described in Sections 2.4.3 and 3.4.1. Where aspirated temperature and humidity probes were used (2016), a correction for radiation error was not applied to the obtained T_z values. The fluxes of Q_R and Q_G were calculated from the rain gauge data and ice thermistor values, as outlined in Sections 2.4.3.

Prior to quantifying the importance of the turbulent heat fluxes to surface ablation, and investigating their behaviour and parameterisation on sloped surfaces, a test for closure of the SEB was performed. This was done to determine if the employed observation and data processing methods had adequately captured the energy balance at each location, and to give confidence to the implementation of these values in the analysis required for this study. The eight observed fluxes were implemented into the SEB model described in Section 2.4.4 to produce 30-minute, daily, and seasonal estimates of ablation at each station. With similar values returned from the OPEC and CPEC systems (Figure 4.1), the CPEC datasets were used to populate the turbulent heat flux values in the SEB model, as that form of system was present on each station (other than for NG14, where only OPEC data were available). T_s in the model was observed from the infrared surface temperature sensors in 2015 and 2016, and estimated from capped, outgoing longwave radiation in 2014 (as described in Section 2.4.3). Modelled ablation was converted into surface height

changes (Equation 2.17) by multiplying the half-hourly ablation totals (in m w.e.) by the ratio of the density of water to the density of ice or snow. A constant value of 900 kg m^{-3} was used for ρ_i , a ρ_s value of 440 kg m^{-3} (400 kg m^{-3}) was used for the firn/old snow surfaces at CG16-1&2 (NG14), and a range of ρ_s values from 80 to 400 kg m^{-3} were used across the station sites for fresh snowfall layers, determined by comparing precipitation amounts from the rain gauge data with observed increases in surface height. The modelled surface height values were then compared with the changes in height observed by the sonic rangers; their values smoothed as outlined in Section 2.4.3. Where multiple sonic rangers were present at a station (2015 and 2016), the mean of their 30-minute height change values were used. Through the season, if the onset of tilting of one of the rangers was detected (by examination of the height data and camera imagery, as done in Section 2.6.1), that sensor's data was excluded from the remaining model to ranger comparisons. Tilting of one or more of the sonic rangers was noted at all stations other than CG16-2. At CG16-1, all rangers exhibited some tilting by the end of the season, adding uncertainty to model comparisons during the last portion of observations. The ablation model returned good performance for each station when compared with observed ablation rates (see Figure B.1 in the Appendices), with RMSE values of $0.02\text{--}0.04 \text{ m day}^{-1}$, indicating closure of the SEB, and giving confidence to the observed values. The partitioning of the SEB was then determined for each location by calculating the relative contribution of each flux to melt energy over seasonal, daily, and 30-minute timescales. The importance of the turbulent heat fluxes to surface ablation at each site, and the variation of this importance with time was then assessed, along with determining the key drivers of this variability.

4.3.4 Katabatic flow and LLWM Detection

As described in Section 4.3.1, the surface slope angles of the glacier sites in this study ranged from 3° to 13°. Observations of wind speed, direction, and the temperature gradient between the air and surface were examined to determine the occurrence of slope-driven air flow, with the frequency of this occurrence compared between station locations and slope angles. Coarse identification of potential katabatic wind conditions was initially carried out by highlighting periods when air flow ($> 3 \text{ ms}^{-1}$) persisted in the downslope direction for that site over the course of several hours or days. At CG16-1, changes in the near-surface temperature lapse rate, as observed by the probe array described in Section 4.3.2, were also examined for the influence of katabatic flow.

To refine the identification of katabatic periods at each station, and to investigate the potential influence of these conditions on turbulent flux generation and parameterisation performance, a method was developed to determine when a LLWM may have been close to measurement height. Ideally, data from observation masts with measurements of wind speed at multiple heights in the surface layer would be used for detecting the height and speed of a LLWM (e.g. Smeets *et al.*, 2000). In the absence of such measurements, an identification method was proposed using the available wind data from the stations. At each station, the wind monitor had been vertically offset from the sonic anemometer of the EC system, positioned above by between +0.5 m and +0.7 m (sonic anemometers were located ~ 2 m above the surface; see Table 3.2). The differences in the 30-minute values for mean wind speed (Δu) between the lower sonic anemometer (\bar{u}_{sonic}) and the upper wind monitor (\bar{u}) were examined to identify periods when a LLWM may have been close to measurement height:

$$\Delta u = \bar{u}_{sonic} - \bar{u} . \quad (4.1)$$

Periods when the \bar{u}_{sonic} values from the lower anemometer approached ($\Delta u \approx 0$) or surpassed ($\Delta u > 0$) the \bar{u} values were proposed to have a LLWM close to or below the height of the upper wind monitor. This method assumes that the wind profile in the surface layer is sufficiently smooth (over a 30-minute averaging period) so that changes in Δu are due to changes in position of the wind maximum rather than noise in the profile. In addition, it is assumed that changes in Δu are substantially larger than calibration differences between the sensors. As described in Section 4.2, previous studies have noted that the structure of a surface layer, in terms of wind shear and the mechanical production of turbulence, will be substantially modified in the vicinity of a LLWM, with friction velocity values reducing towards zero. The friction velocity values recorded by the EC sensors (u_{*ec}) were compared with Δu at each station, to examine if this expected behaviour was observed when Δu indicated a proximal LLWM.

4.3.5 Turbulent Flux Parameterisation

The turbulent heat fluxes were initially parameterised using the C_{log} and C_{MO} forms of the bulk aerodynamic method (as introduced in Sections 1.6.1 and 2.4.5). The bulk method assumes constant values for the turbulent fluxes and friction velocity between a given measurement height and the surface. Friction velocity in the bulk method can be expressed as follows (Stull, 1988):

$$u_{*bulk} = C_v \bar{u} , \quad (4.2)$$

where the transfer coefficient, C_v , representing bulk eddy viscosity, is expressed as:

$$C_v = \frac{k}{\ln\left(\frac{zu}{z_0v}\right) - \psi_m\left(\frac{zu}{L}\right)} . \quad (4.3)$$

The turbulent fluxes of sensible and latent heat have the following bulk expressions:

$$Q_H = \rho_a c_p C_v \bar{u} C_T (\bar{T}_z - \bar{T}_s) , \quad (4.4)$$

$$Q_L = \rho_a L_v C_v \bar{u} C_q (\bar{q}_z - \bar{q}_s) . \quad (4.5)$$

Substituting friction velocity directly into Equations 4.4 and 4.5, the fluxes can be expressed as:

$$Q_H = \rho_a c_p u_{*bulk} C_T (\bar{T}_z - \bar{T}_s) , \quad (4.6)$$

$$Q_L = \rho_a L_v u_{*bulk} C_q (\bar{q}_z - \bar{q}_s) , \quad (4.7)$$

where the transfer coefficient $C_{T/q}$ represents the bulk eddy diffusivity for temperature/humidity:

$$C_{T/q} = \frac{k}{\ln\left(\frac{z}{z_{0t/q}}\right) - \psi_{h/e}\left(\frac{z}{L}\right)} . \quad (4.8)$$

The C_{log} form of the bulk method excludes a stability function and assumes neutral atmospheric stability ($\psi_m\left(\frac{z_u}{L}\right) = \psi_{h/e}\left(\frac{z}{L}\right) = 0$), while the C_{MO} form uses empirically-derived stability functions (Equations 2.23–2.26) based on the Monin-Obukhov length (Monin and Obukhov, 1954; Dyer, 1974; Beljaars and Holtslag, 1991). Site-specific roughness length values determined from EC measurements (Table 3.4) were implemented into the transfer coefficients in order to isolate the effects of the applied stability method on the parameterised values. The bulk estimates of u_{*bulk} , Q_H and Q_L were evaluated against observed values for periods with ideal EC measurement conditions, namely, periods without precipitation, with wind direction within $\pm 45^\circ$ of the main axis of EC sensor (to reduce the effects of air flow distortion through station structure), with sufficient gradients in air temperature ($> 1^\circ\text{C}$) and vapour pressure (> 66 Pa) between measurement height and the surface, and with stationary and developed turbulent conditions as identified following the quality control methods of Mauder and Foken (2004).

4.3.6 Katabatic Influence on Friction Velocity and Bulk Parameterisation

Variation in Δu was compared with the difference between modelled and observed turbulent heat flux at each station, to quantify the potential influence of the presence of a LLWM on parameterisation performance. Differences in 30-minute values of EC-observed and bulk-modelled friction velocity (Δu_*), expressed as:

$$\Delta u_* = u_{*bulk} - u_{*ec} , \quad (4.9)$$

were examined to detect the expected reduction of friction velocity in the vicinity of a LLWM, and the resulting overestimation in u_{*bulk} ($\Delta u_* > 0$). To investigate the influence of friction velocity estimation on parameterisation performance, the turbulent heat fluxes were parameterised by replacing the u_{*bulk} values in the C_{log} bulk method (Equations 4.6 and 4.7) with observed u_{*ec} values. The hypothesis was that when $\Delta u_* = 0$, the bulk-estimated fluxes would agree with the EC-observed values. Following on from this, a metric was proposed as a potential indicator of shallow, katabatic conditions, and a predictor of Δu_* . As determining Δu_* requires observed friction velocity from sonic anemometers, the goal was to develop a predictor for Δu_* that relied on mean meteorological variables, only. The proposed metric, Δu_{log} , was the deviation at measurement height of the observed wind profile from the assumed log wind profile of the bulk method. Wind speed values (\bar{u}) from the upper level (z_u) were used to estimate wind values (u_{log}) at the level of the lower anemometer (z) through use of the log wind profile, where friction velocity is assumed constant:

$$u_{log} = \bar{u} \frac{\ln\left(\frac{z}{z_{0v}}\right)}{\ln\left(\frac{z_u}{z_{0v}}\right)} . \quad (4.10)$$

The difference between the observed mean wind speed at z (\bar{u}_{sonic}) and u_{log} was expressed as:

$$\Delta u_{log} = \bar{u}_{sonic} - \bar{u}_{log} , \quad (4.11)$$

and compared with variation in Δu_* for each of the EC systems on the five deployed stations (seven systems in total). A linear regression model for Δu_* with Δu_{log} was estimated separately for each of the seven datasets using cross-validation methods. Each dataset was divided into a training subset (50%), a validation subset (25%), and a test subset (25%). Bootstrapping methods were used to resample the training subset 100 times and to estimate regression coefficients for each resampling. These 100 linear models were then applied to the validation subset, and the model producing the lowest RMSE value was selected as the model for that system's dataset. The performance of this model was then evaluated using the test subset. This process was repeated for each system, returning seven linear models in total. These models were then compared to determine if the departure of the wind profile from logarithmic led to similar friction velocity behaviour at each location, and if Δu_{log} was a robust katabatic indicator. The seven models were used to estimate the potential adjustment required to bring u_{*bulk} values in line with EC-observed values. The means of the regression coefficients from the linear models (β_0, β_1) were used to estimate adjusted friction velocity values, u_{*adj} :

$$u_{*adj} = u_{*bulk} - (\beta_0 + \beta_1 \Delta u_{log}). \quad (4.12)$$

For non-katabatic conditions (as indicated by Δu_{log}), when the application of the bulk method and the assumption of a constant flux layer were considered valid, the u_{*adj} values were implemented into Equations 4.6 and 4.7, replacing u_{*bulk} , and used to calculate adjusted turbulent heat fluxes.

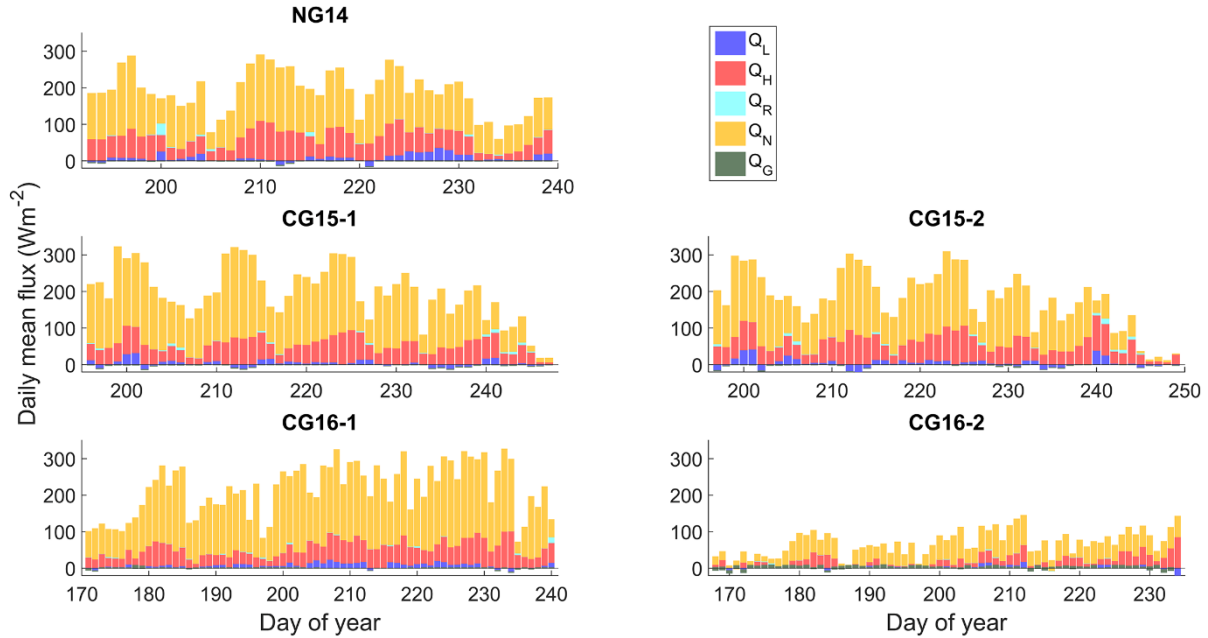


Figure 4.3. Partitioning of the daily mean energy received at the surface for each station.

4.4 Results

4.4.1 Turbulent Flux Importance and Variability

While net radiation dominated the SEB overall, the turbulent heat fluxes provided a substantial contribution to melt energy received at each station (Figure 4.3), ranging from 28% at CG16-1 to 35% at NG14. The majority of this energy was supplied through the sensible heat flux, with an average melt energy contribution over the five stations of 28%. Q_L was relatively small at each location, providing 3.1% of melt energy, on average, and generating little sublimation ($< 0.1\%$ of ablation). Seasonal mean values of Q_H were relatively consistent between the four stations in the ablation zones of Nordic and Conrad Glaciers (53–56 W m^{-2}), and substantially reduced at CG16-2 in the accumulation zone (19 W m^{-2}).

Substantial variability in the magnitude of daily mean Q_H and Q_L was observed at each station (Figure 4.3), ranging from 9 to 105 W m^{-2} for daily mean Q_H at NG14, for example. The

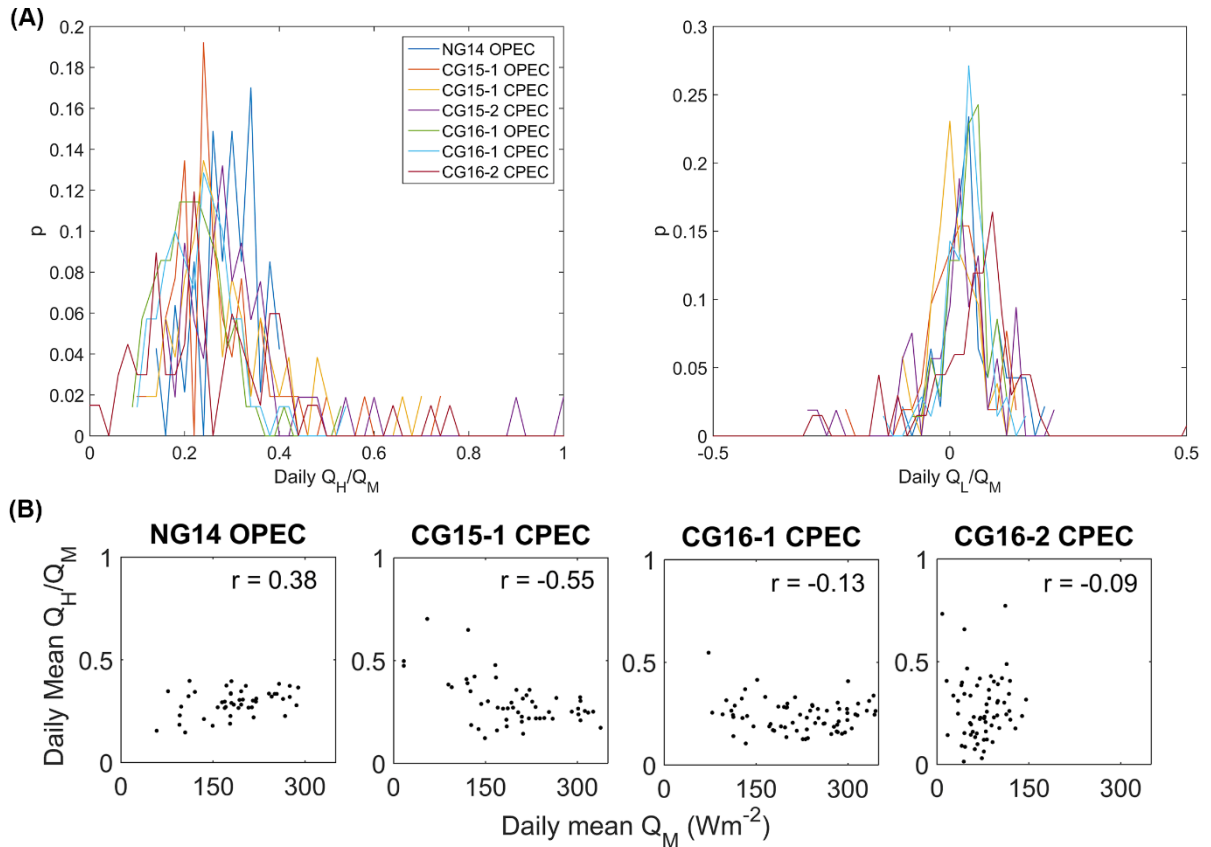


Figure 4.4. (A) Frequency (p) in occurrence of the daily ratios of the turbulent heat fluxes to melt energy for each station, and (B) relationship between daily mean melt energy and the relative contribution of the sensible heat flux.

relative contribution of the turbulent heat fluxes to daily Q_M was calculated for each day at each station as the ratios of daily Q_H/Q_M and Q_L/Q_M . The most frequently occurring daily ratios were identified at each station (Figure 4.4A), and showed similar values between locations (0.21 to 0.34 for Q_H/Q_M , and 0 to 0.09 for Q_L/Q_M). Days with greater Q_H contributions to Q_M showed moderate correlation with larger Q_M days at NG14 ($r = 0.38$; $p < 0.01$). At all other stations, however, negative or no significant correlation was noted between greater Q_H contributions and larger Q_M days (Figure 4.4B). As in Figure 4.4B, the data from some EC sensors are not presented in this

chapter's figures, as very similar results were achieved for OPEC and CPEC sensors at the same location, and for stations in Conrad's ablation zone.

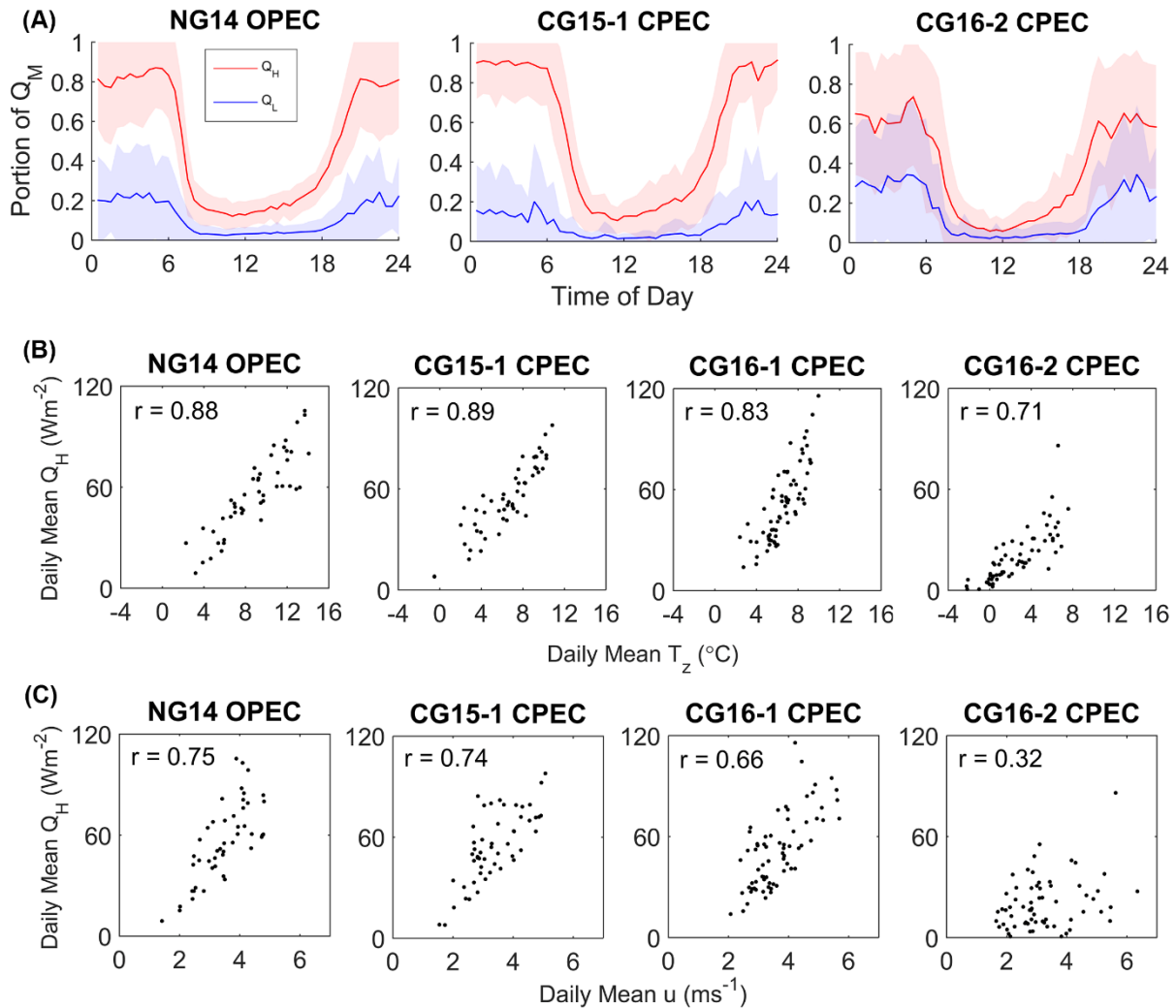


Figure 4.5. (A) Mean daily cycle of turbulent heat flux contribution to melt energy. Flux contribution is expressed as a portion of the mean Q_M received over the season for each 30-minute period. Shaded areas represent the standard deviation in flux contribution over the season for each period. Also shown is the relationship between daily mean Q_H and (B) air temperature, and (C) wind speed.

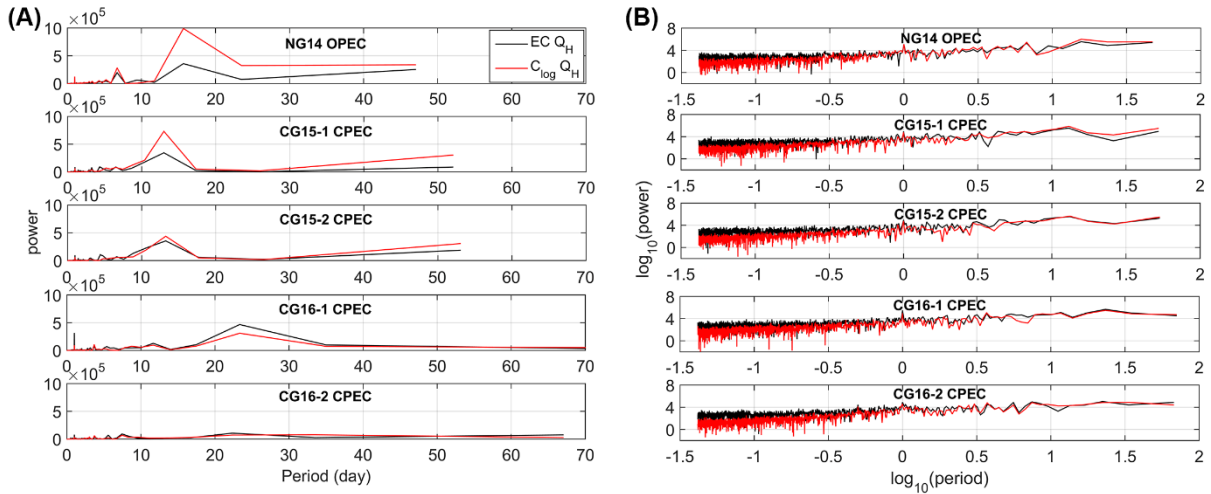


Figure 4.6. (A) The temporal variability in the magnitude of the sensible heat flux for each station, analysed using a FFT power spectrum; (B) the same, shown in log-log scale.

The mean daily cycle of turbulent flux contribution to Q_M was noted to be similar at each station (Figure 4.5A). From mid-morning to late afternoon, Q_H and Q_L provided approximately 20% and 2% of the energy to Q_M , respectively. As the input of solar radiation diminished, the relative contributions of Q_H and Q_L to melt energy rapidly increased to 80% and 20% during night hours. At CG16-2, Q_H provided a lower contribution to melt energy than at the other stations, with 10% and 60% contributions during day and night periods, respectively.

The magnitude of daily mean Q_H was strongly correlated with both daily mean T_z ($r = 0.71\text{--}0.92$; $p < 0.01$) and daily mean u ($r = 0.32\text{--}0.82$; $p < 0.01$) at each station other than CG16-2, where the correlation between daily mean Q_H and u was substantially reduced (Figure 4.5B-C). The temporal variability in the 30-minute Q_H values was analysed using an FFT power spectrum (Figure 4.6A). At all stations, a small peak in variability was noted for a period of one day, likely indicating the influence of the diurnal air temperature cycle on sensible heat flux. Additional peaks in variability with periods of three to seven days were also observed at each station, possibly

indicating the passage time of synoptic-scale weather systems. The period of the dominant peak in Q_H variability was noted to change between seasons, but to be consistent across stations operating at different locations during the same season. These periods (15 days for 2014; 13 days for 2015; 23 days for 2016) appear to correspond with the period of warm air temperature events during each season. Spectrum analysis was also performed on the Q_H values from the C_{log} bulk method, and showed agreement with the aforementioned periods of peak variability in the observed values, with a general tendency for the magnitude of variability to be overestimated. This is also shown in the log-log scale spectrum (Figure 4.6B), where the long-term variability is generally overestimated by the C_{log} method, and the short-term variability (period < 1 day) is underestimated.

4.4.2 Glacier Winds and Friction Velocity

At each station site, the prevailing wind was in line with the mean downslope direction of the glacier at that location (Figure 4.7). Persistence in wind direction varied between sites, with air flow remaining within $\pm 45^\circ$ of downslope for 97% of observations at NG14, approximately 92% of observations at each of CG15-1, CG15-2, and CG16-1, and 77% of observations at CG16-2. Peak wind speed events at NG14 corresponded with strong gradients in temperature between measurement height and the surface, with a correlation between \bar{u} and $T_z - T_s$ of $r = 0.55$ ($p < 0.01$). This relationship was weaker at each of the stations in Conrad's ablation zone (mean $r = 0.3$), and essentially non-existent at CG16-2 ($r = -0.1$).

Figure 4.8 displays the difference in 30-minute values of observed mean wind speed (Δu) between the vertically offset sonic anemometer (\bar{u}_{sonic}) and upper wind monitor (\bar{u}) at each station. \bar{u}_{sonic} regularly approached and surpassed \bar{u} at each location, suggesting the presence of

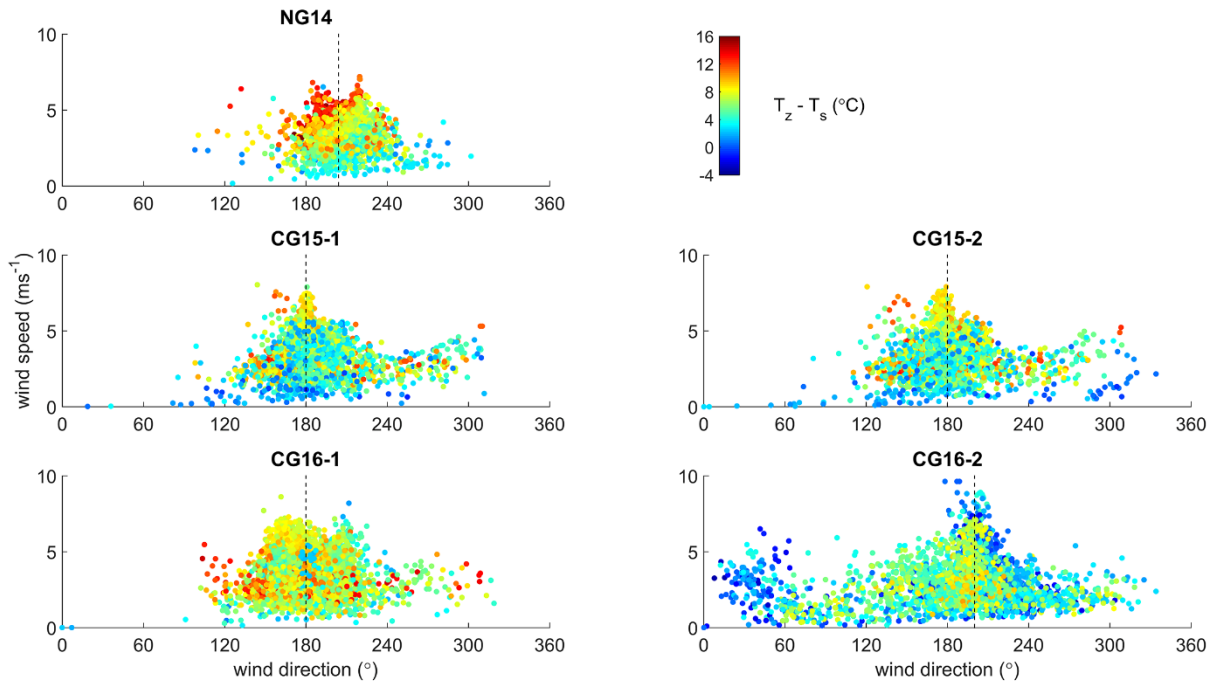


Figure 4.7. Relationship between observed 30-minute values of wind direction, wind speed, and temperature difference between air at measurement height (2 m) and the surface at each station. The dashed line marks the mean azimuth of the surface slope for each site.

a LLWM close to measurement height during these periods. This occurred most commonly at NG14, where \bar{u}_{sonic} exceeded \bar{u} for 60.3% of observations. In Figure 4.9, the u_{*ec} values recorded by the EC sensors are compared with Δu for each system. Friction velocity values were observed to decrease as \bar{u}_{sonic} approached and exceeded \bar{u} , corresponding with the expected wind shear behaviour close to a lowering wind maximum.

When compared with u_{*ec} (Figure 4.10A), the parameterised friction velocity values (u_{*bulk}) showed weak correlation and a tendency to overestimate, particularly during stable conditions. This overestimation is most pronounced at NG14, with mean u_{*ec} and u_{*bulk} values of 0.14 ms^{-1} and 0.22 ms^{-1} , respectively, and $r = 0.1$ ($p < 0.01$). At CG16-2, however, modelled

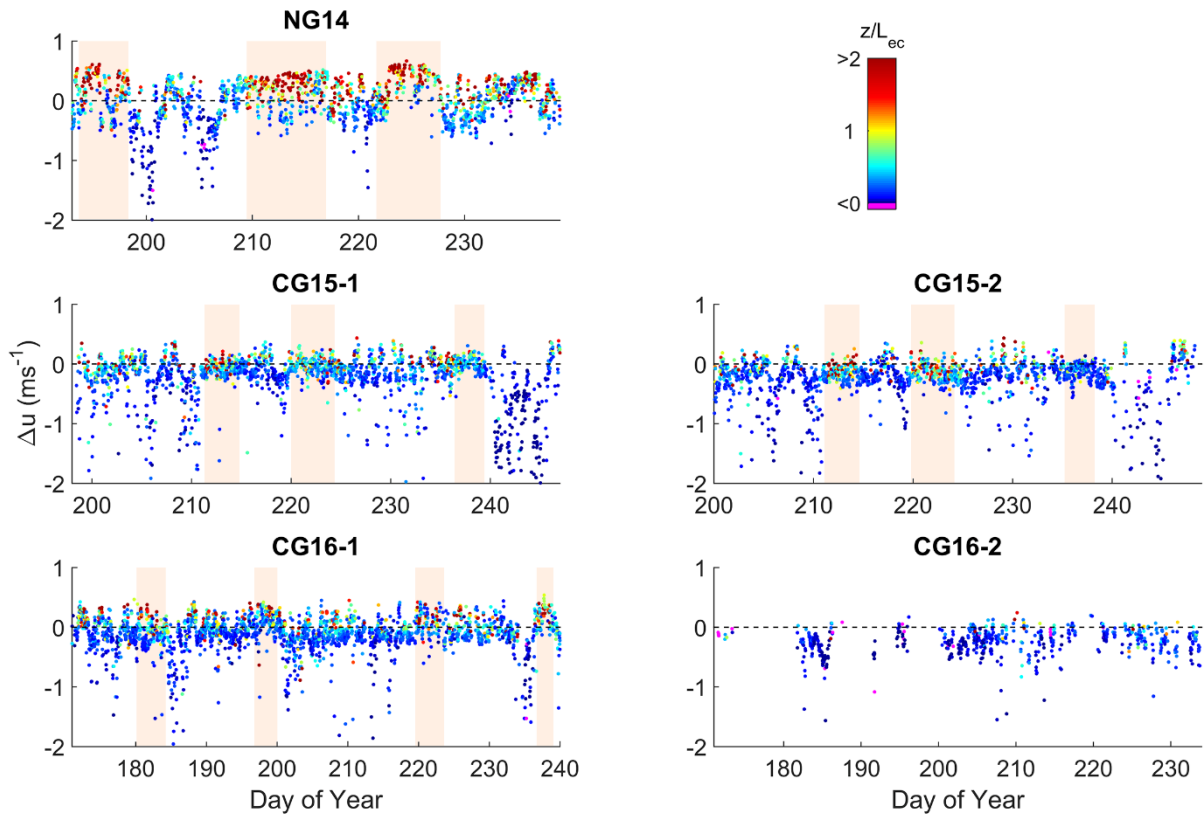


Figure 4.8. Difference in 30-minute values of observed mean wind speed ($\Delta u = \bar{u}_{sonic} - \bar{u}$) between the lower sonic anemometer (\bar{u}_{sonic}) and upper wind monitor (\bar{u}) at each station. Stability for each period is identified through the EC-derived stability parameter, $\frac{z}{L_{ec}}$. Periods broadly identified as having katabatic conditions are shaded orange.

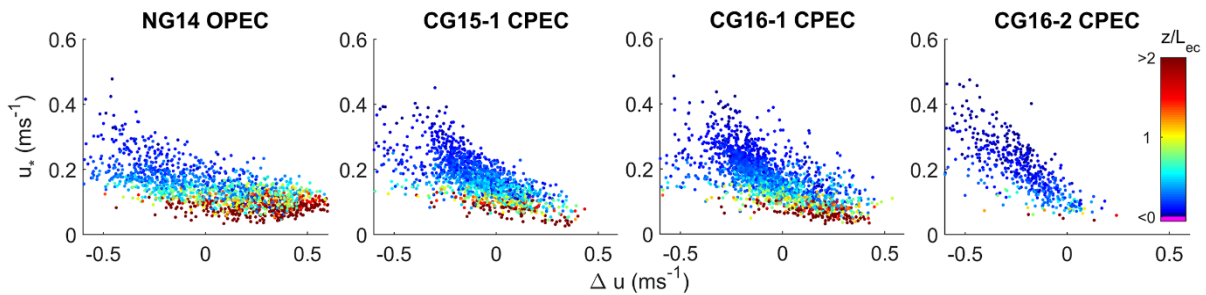


Figure 4.9. Friction velocity values, as recorded by each EC sensor, compared with Δu .

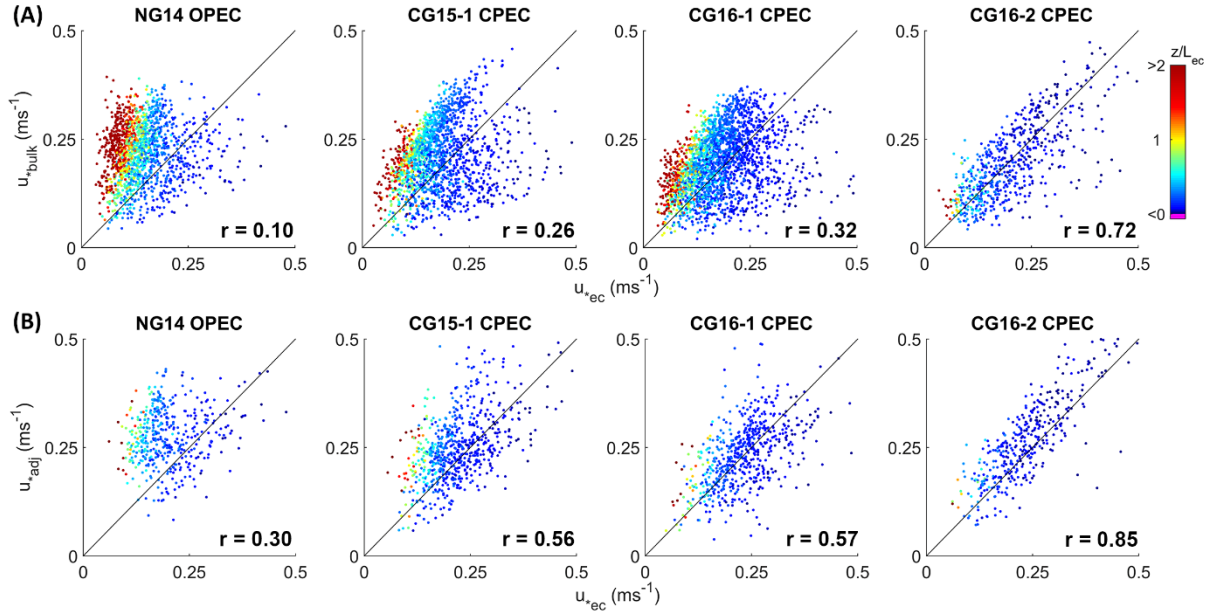


Figure 4.10. Comparison of EC-observed friction velocity (u_{*ec}) with (A) u_{*bulk} values from the C_{log} method, and (B) modelled u_{*adj} values for non-katabatic periods ($\Delta u_{log} < 0$).

and observed u_* showed good agreement ($r = 0.72$), with mean values of 0.19 ms^{-1} and 0.20 ms^{-1} , respectively. A strong linear relationship between u_{*ec} and wind speed was observed at CG16-2 ($r = 0.72$), but with substantial scatter in this relationship observed at all other stations (see Figure B.2 in the Appendices).

Δu_{log} values were calculated for each EC sensor, following Equations 4.10 and 4.11. The differences in bulk and observed friction velocity (Δu_*) were plotted against Δu_{log} for each of the seven systems, as shown in Figure 4.11. In general, u_{*bulk} performed well ($\Delta u_* \approx 0$) when the wind profile was close to logarithmic ($\Delta u_{log} \approx 0$), and showed a tendency to overestimate (underestimate) as Δu_{log} became more positive (negative). Most observations occurred within a Δu_{log} range of $\pm 0.5 \text{ ms}^{-1}$. The cross-validation methods outlined in Section 4.3.6 were applied to the Δu_{log} and Δu_* values for each EC system, returning seven linear models for Δu_* with Δu_{log}

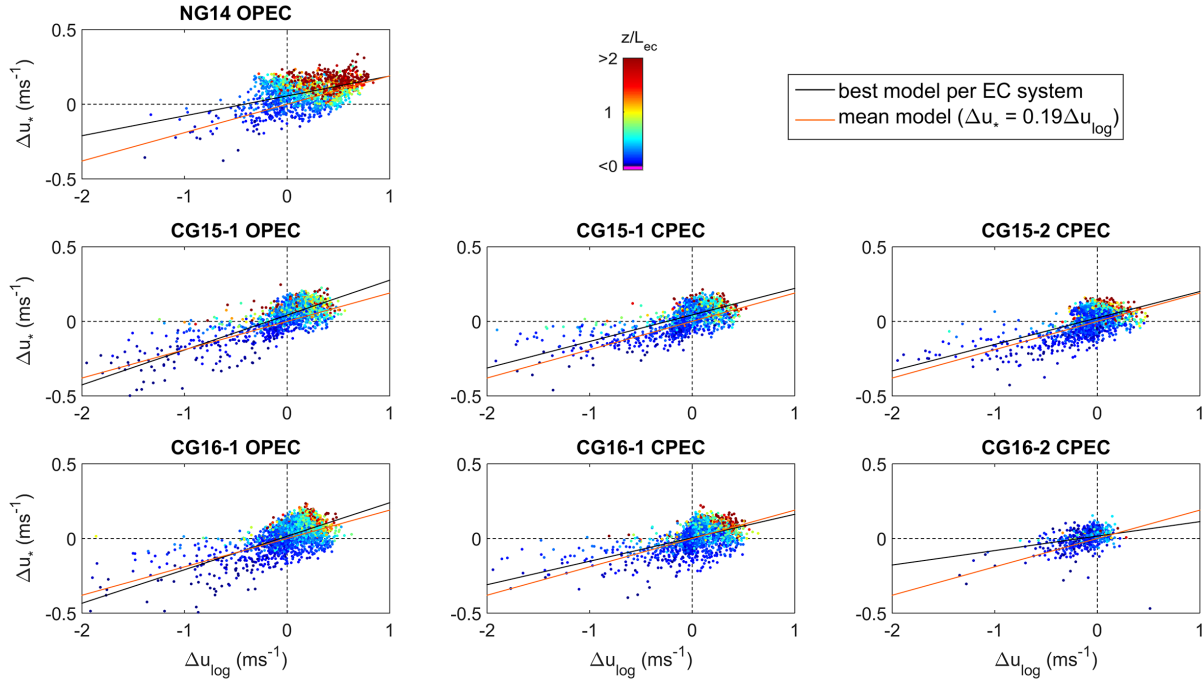


Figure 4.11. 30-minute differences in bulk and observed friction velocity (Δu_*) plotted against Δu_{log} for each EC system. The best performing linear model obtained through cross-validation for each system is shown (black line), as is the mean model applied to all datasets (orange line).

as the predictor (Figure 4.11). Six of the models returned similar regression coefficients (CG16-2 model being the outlier), indicating the relationship between Δu_{log} and Δu_* to be transferable across these test locations. In addition to corresponding with overestimation of modelled friction velocity and increased atmospheric stability, positive Δu_{log} values were also found to correspond with suppressed temperature lapse rates, a further indication of katabatic conditions. Across the lower trunk of Conrad Glacier (between the LR1 and LR3 probes; elevation range of 1972–2393 m), reduced lapse rates (Γ) were observed when Δu_{log} at CG16-1 was positive (mean ‘katabatic’ $\Gamma = 3.1^\circ\text{C km}^{-1}$), relative to the mean observed Γ for non-katabatic conditions of $5.7^\circ\text{C km}^{-1}$. For non-katabatic conditions (as indicated by $\Delta u_{log} < 0$), the means of the regression coefficients of

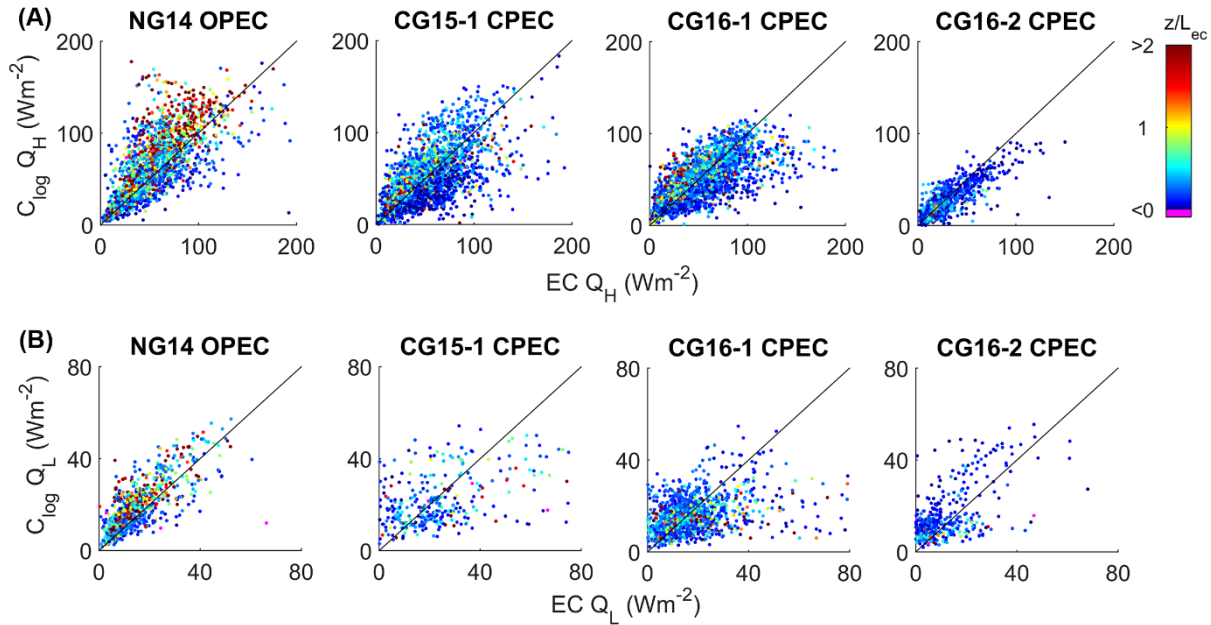


Figure 4.12. Performance of the 30-minute C_{log} parameterised fluxes when compared with EC observations for (A) Q_H and (B) Q_L . Comparisons were carried out for periods with ideal EC measurement conditions only. Similar performance was observed for the C_{MO} method (not shown).

the six agreeing models in Figure 4.11 (slope of 0.19, with intercept through the origin) were implemented into Equation 4.12 to estimate adjusted friction velocity values, u_{*adj} (Figure 4.10B). These adjusted values showed moderate to strong correlation with observed u_{*ec} ($r = 0.3\text{--}0.85$; $p < 0.01$).

4.4.3 Parameterisation Performance

Figure 4.12 and Table 4.1 display the performance of the bulk parameterised fluxes when compared with observations from each EC system (during ideal measurement conditions). Utilised with site-specific roughness length values, the tested bulk methods displayed relatively good performance in estimating the turbulent heat fluxes at each station. In general, the C_{log}

Table 4.1. Performance of the C_{log} , C_{MO} , and u_{*ec} and u_{*adj} bulk parameterised fluxes when compared with observations from each EC system (during ideal measurement conditions). For the u_{*adj} bulk values, only non-katabatic period ($\Delta u_{log} < 0$) are assessed.

	$EC Q_H$	$C_{log} Q_H$				$EC Q_L$	$C_{log} Q_L$			
	Mean ($W m^{-2}$)	Mean ($W m^{-2}$)	r	RMSE ($W m^{-2}$)	MBE (%)	Mean ($W m^{-2}$)	Mean ($W m^{-2}$)	r	RMSE ($W m^{-2}$)	MBE (%)
NG14 OPEC	56	66	0.70	29	31	15	19	0.77	8	60
CG15-1 OPEC	52	55	0.73	23	19	20	24	0.57	13	35
CG15-1 CPEC	56	53	0.57	30	8	18	24	0.56	17	72
CG15-2 CPEC	55	45	0.58	29	6	28	17	0.55	24	-38
CG16-1 OPEC	47	51	0.72	21	30	15	19	0.76	8	44
CG16-1 CPEC	51	48	0.68	24	18	17	16	0.43	11	98
CG16-2 CPEC	28	25	0.79	16	-2	11	15	0.62	11	89
	$EC Q_H$	$C_{MO} Q_H$				$EC Q_L$	$C_{MO} Q_L$			
NG14 OPEC	56	61	0.67	29	18	15	17	0.73	8	43
CG15-1 OPEC	52	50	0.70	24	4	20	20	0.54	13	9
CG15-1 CPEC	56	48	0.53	32	-4	18	20	0.43	20	2
CG15-2 CPEC	55	40	0.51	33	-10	28	14	0.47	26	-47
CG16-1 OPEC	47	46	0.66	23	11	15	17	0.72	8	27
CG16-1 CPEC	51	42	0.60	28	-2	17	14	0.35	12	79
CG16-2 CPEC	28	23	0.76	17	-10	11	14	0.60	11	3
	$EC Q_H$	$C_{log} Q_H u_{*ec}$				$EC Q_L$	$C_{log} Q_L u_{*ec}$			
NG14 OPEC	56	45	0.58	31	-12	15	12	0.69	8	5
CG15-1 OPEC	52	49	0.63	27	8	20	21	0.71	11	27
CG15-1 CPEC	56	47	0.71	24	-4	18	15	0.68	17	-74
CG15-2 CPEC	55	49	0.67	26	11	28	20	0.69	16	-31
CG16-1 OPEC	47	45	0.68	24	11	15	15	0.76	7	25
CG16-1 CPEC	51	48	0.75	22	17	17	15	0.52	11	67
CG16-2 CPEC	28	31	0.89	11	9	11	16	0.69	10	49
	$EC Q_H$	$C_{log} Q_H u_{*adj}$				$EC Q_L$	$C_{log} Q_L u_{*adj}$			
NG14 OPEC	62	74	0.59	34	29	20	26	0.73	11	53
CG15-1 OPEC	55	67	0.69	31	35	25	31	0.56	17	51
CG15-1 CPEC	63	63	0.61	31	9	19	28	0.33	30	37
CG15-2 CPEC	62	60	0.64	28	1	25	26	0.68	17	13
CG16-1 OPEC	55	62	0.64	27	29	18	21	0.75	9	39
CG16-1 CPEC	62	61	0.69	24	10	20	22	0.64	11	58
CG16-2 CPEC	35	36	0.84	15	5	13	22	0.75	14	39

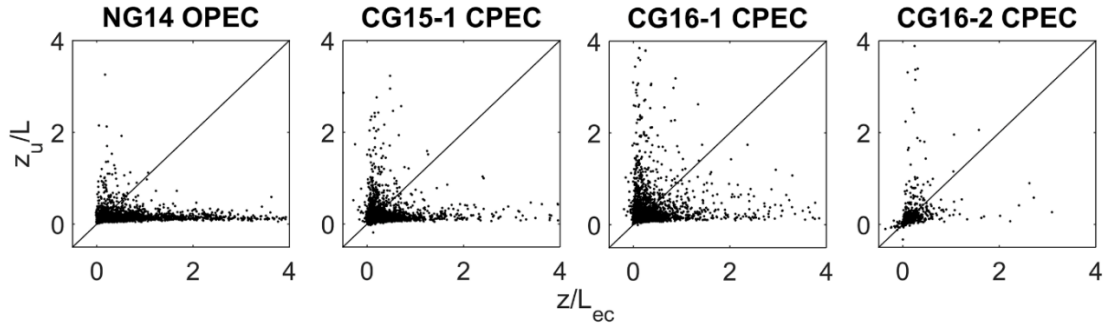


Figure 4.13. Comparison of the 30-minute EC-derived stability parameters ($\frac{z}{L_{ec}}$), and those estimated using the C_{MO} method ($\frac{z_u}{L}$).

parameterisation returned better performance than the C_{MO} method, with correlation values ranging from 0.57 to 0.79 for Q_H , and 0.43 to 0.77 for Q_L ($p < 0.01$). The seasonal mean C_{log} fluxes varied between small levels of over- and underestimation across the stations, but with substantial overestimation at NG14 (19%). The C_{MO} method also overestimated the mean turbulent fluxes at NG14. At all other stations, the C_{MO} values showed a tendency to underestimate the mean flux magnitude, and to have slightly weaker correlation with the EC observations, relative to C_{log} (r values of 0.51 to 0.76 for Q_H , and 0.35 to 0.73 for Q_L ; $p < 0.01$). For both methods, the strongest bulk performances were obtained at CG16-2. Using the EC-derived stability parameter ($\frac{z}{L_{ec}}$), overestimation in the bulk fluxes was noted to increase with stability. The parameter used to determine stability in the C_{MO} method, $\frac{z_u}{L}$ (following Munro, 1989; as described in Section 2.4.5), showed little agreement with $\frac{z}{L_{ec}}$ at all stations other than CG16-2 (Figure 4.13).

Examining the difference in 30-minute values of parameterised and observed Q_H ($\Delta Q_H = \text{bulk } Q_H - \text{EC } Q_H$), there was substantial variability in the performances of both bulk methods

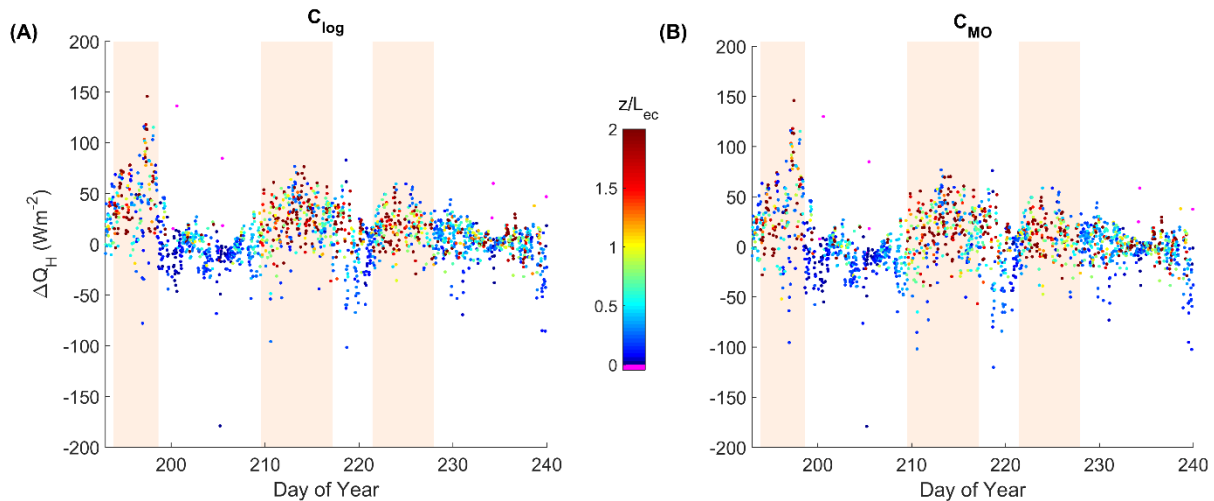


Figure 4.14. Differences in 30-minute values of parameterised and observed Q_H ($\Delta Q_H = \text{bulk } Q_H - \text{EC } Q_H$) for the (A) C_{log} and (B) C_{MO} bulk methods, as recorded at NG14. Similar behaviour was noted at each station in the study other than CG16-2. Periods broadly identified as having katabatic conditions are shaded orange.

(Figure 4.14). In addition to random scatter, intermittent periods of overestimation were noted at each station (most pronounced at NG14). These periods were found to be common to the values from both C_{log} and C_{MO} , and the overestimation to be of substantially greater magnitude than the differences between the two bulk methods. Periods of overestimation were found to correspond with periods of strong local stability ($\frac{z}{L_{ec}} > 1$), and to align with periods coarsely identified as having potentially katabatic wind conditions (air flow $> 3 \text{ ms}^{-1}$ in a persistent downslope direction for several hours or days). Similar behaviour was also noted in the Q_L fluxes.

Comparing variation in Δu with the performance of the tested bulk methods, a similar pattern emerged from each station (Figure 4.15A). Bulk fluxes were underestimated slightly (relative to EC observations) while upper level wind speed values remained substantially faster than the lower level values. As the wind maximum lowered, however, the bulk method began to overestimate the fluxes. This behaviour was visible in both turbulent fluxes, but most evident in

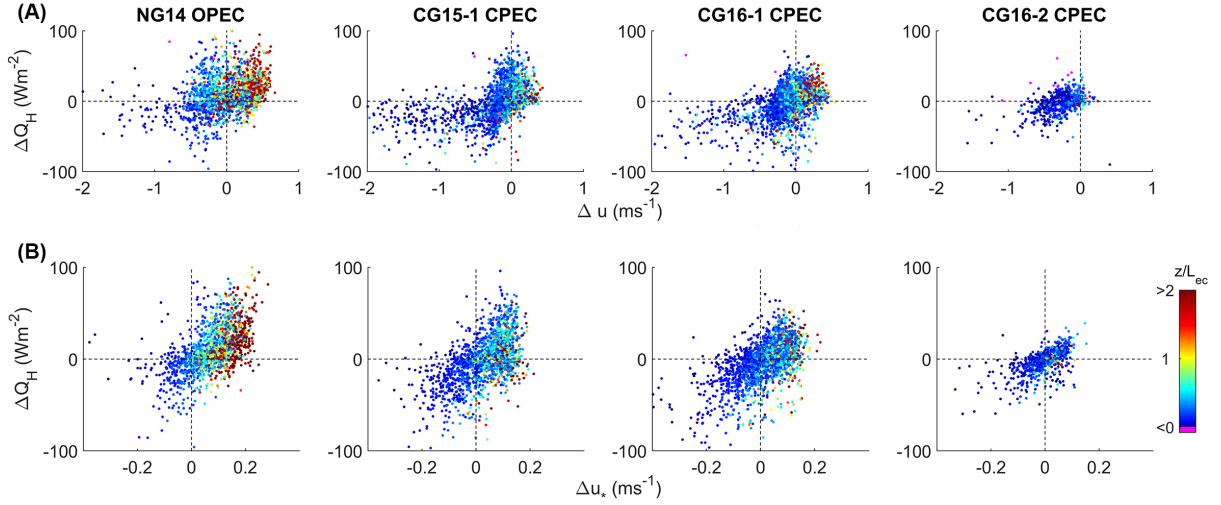


Figure 4.15. Variation in 30-minute values of (A) Δu , and (B) Δu_* with the parameterisation performance for $C_{log} Q_H$ ($\Delta Q_H = \text{bulk} - \text{obs. flux}$). Similar behaviour was noted at each station in the study, and for fluxes values from both the C_{log} and C_{MO} bulk methods.

the larger magnitude Q_H values. The differences in bulk and observed u_* (Δu_*) were also compared with parameterisation performance, as is shown for the sensible heat flux from C_{log} in Figure 4.15B. Periods of overestimation in u_* were found to be frequent and to correspond with periods of flux overestimation, while periods of flux underestimation corresponded with underestimated u_* . The observed u_{*ec} values were implemented to replace u_{*bulk} in the C_{log} bulk method (Equations 4.6 and 4.7), and used to calculate parameterised fluxes for each station (Figure 4.16A and Table 4.1). In general, utilising u_{*ec} values in the bulk method led to underestimation of the flux estimates, most pronounced at NG14 (seasonal mean values of 56 W m^{-2} and 44 W m^{-2} for observed and modelled Q_H , respectively). This underestimation when using u_{*ec} values was not observed at CG16-2, nor for non-katabatic periods at other locations (e.g. 62 W m^{-2} and 64 W m^{-2} for mean observed and modelled Q_H at CG16-1 when $\Delta u_{log} < 0$).

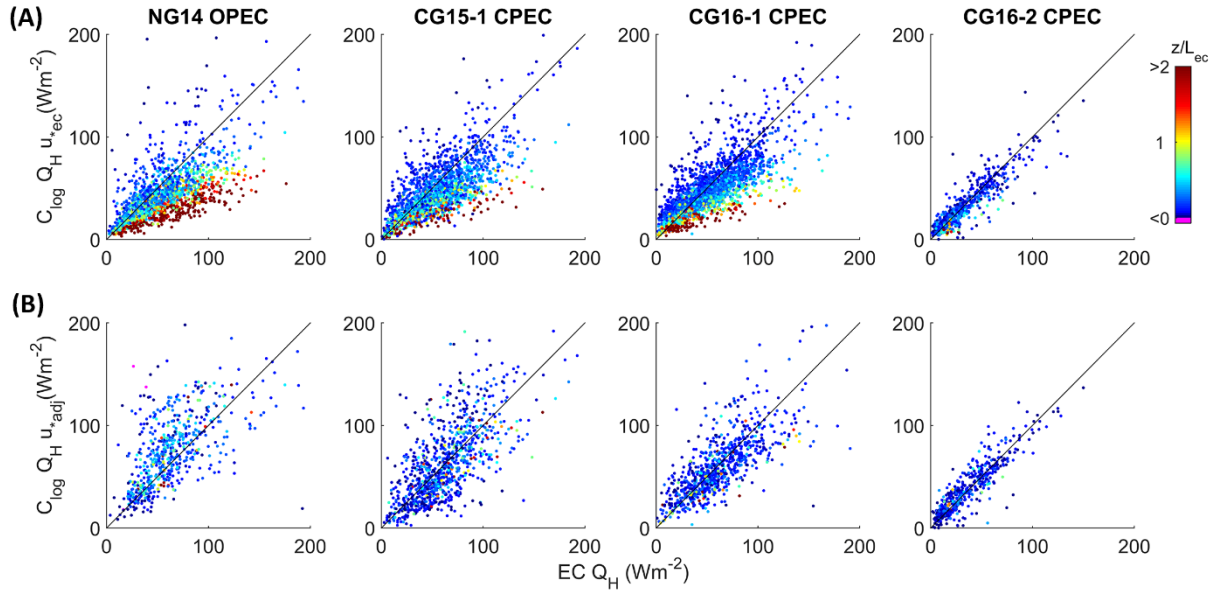


Figure 4.16. Performance of the C_{log} bulk method when implemented with (A) observed u_{*ec} , and (B) modelled u_{*adj} friction velocity values, compared with 30-minute EC observations of Q_H . Only non-katabatic periods ($\Delta u_{log} < 0$) are shown where u_{*adj} values are utilised.

The modelled u_{*adj} values were also implemented into Equations 4.6 and 4.7, and used to estimate the turbulent heat fluxes for non-katabatic conditions (Figure 4.16B and Table 4.1), returning good performance when compared with EC fluxes (e.g. $r = 0.59$ – 0.84 for Q_H values).

4.5 Discussion

4.5.1 Turbulent Flux Variability

At each station over the course of this study, the turbulent heat fluxes were observed to be an important component of glacier SEB, and a driver of surface ablation, highlighting the need for accurate observation or estimation of their values. As presented in Section 4.4.1, Q_H was noted to provide a lower contribution to Q_M at CG16-2 than at the other stations. Air temperatures were

substantially reduced at CG16-2 (mean T_z of 2.2°C), relative to the lower elevation stations (mean T_z of 6.6°C at CG15-1, CG15-2, CG16-1, and 8.9°C at NG14), resulting in smaller temperature gradients and a weaker sensible heat flux. The reduced correlation between Q_H and u noted at CG16-2 is also likely due to the lower air temperatures. For periods when the air temperature is close to that of the surface, the lack of temperature gradient means that an increase in wind speed will have little impact on the magnitude of the sensible heat flux.

On average, radiation was observed to be the primary contributor to melt energy, but there were individual days where turbulent heat flux dominated the SEB. For example, on DOY 240 and 241 at CG15-2, the turbulent fluxes provided 77.7% and 58.3% of the daily melt energy. Overcast conditions on these days resulted in substantially reduced net radiation fluxes (27.4% and 56% of mean daily Q_N). Despite this reduction, the observed daily melt (DOY 240: 0.048 m w.e.; DOY 241: 0.051 m w.e.) was equal to or greater than the mean daily value for the season (0.048 m w.e./day), with above average daily air temperatures (9.6°C) driving a large sensible heat flux. Similar conditions were observed on DOY 234 at CG16-2, and DOY 200 at NG14. For many of the days where Q_H was a relatively large contributor to Q_M , the rate of surface melt was reduced, however (as shown in Figure 4.4B). Increased cloud cover on these days reduced the input of solar radiation and the net available melt energy, while increasing the relative importance of Q_H . Only at NG14 do we see (moderate) positive correlation between Q_H/Q_M and Q_M . This is due to the strong correlation at NG14 (relative to the other locations) between S_N , the primary driver of melt, and Q_H and T_z ($r = 0.67$ and 0.71 , respectively).

For applications concerned with melt on daily timescales, such as runoff models, the variability observed in the turbulent heat fluxes, and their contribution to melt energy, emphasises the need to incorporate a parameterisation scheme that accounts for such temporal variability.

Spatially, the seasonal mean turbulent heat fluxes were shown to be relatively consistent over small distances (e.g. within Conrad's lower accumulation zone) and similar surface types, but to vary substantially between different zones of the glacier. Distributed models of SEB should account for spatial variability in turbulent flux generation to ensure accurate ablation estimates over the entire glacier.

4.5.2 Slope and Katabatic flow

The stations deployed in this study were positioned on a range of slope angles; the steepest at NG14 (13°) and the shallowest at CG16-2 (3°). Despite this being a relatively small range of angles, the effects of these slope differences are visible in the results presented in Section 4.4. The most evident example of this influence is in the wind values observed at each station. The strongest relationship between wind speed, direction, and air temperature (indicative of katabatic flow) was recorded at NG14, with the weakest relation at CG16-2. In the upper section of the relatively flat accumulation zone where CG16-2 was situated, it is likely that fully developed katabatic flow was rare or non-existent. At all other test sites, katabatic flow was frequent and persistent, as noted in other glacier studies (e.g. Parmhed *et al.*, 2004). Examining the Δu and Δu_{log} values, the occurrence of a LLWM near measurement height was most frequent at NG14. This agrees with previous observations in katabatic flows which note that the height of a wind maximum lowers as slope angle increases (e.g. Oerlemans and Grisogono, 2002). Suppression of temperature lapse rates during katabatic conditions was observed on Conrad Glacier, in agreement with findings from previous glacier studies (e.g. Greuell and Böhm, 1998; Shea and Moore, 2010; Petersen and Pellicciotti, 2011). If a glacier surface has a sufficient slope to drive frequent katabatic airflow,

application of a constant lapse rate (or one based on the background environmental rate) will not adequately capture the changes in the near-surface temperature field due to these conditions.

4.5.3 Bulk Performance and Wind Shear

It has been observed in this study that the performances of the tested bulk methods are sensitive to the occurrence and height of a LLWM. If the parameterisation of the fluxes is performed with or without a stability correction (C_{MO} or C_{log} , respectively), a very similar relation between performance and Δu is returned. This suggests that, over sloped glacier surfaces with frequent katabatic conditions, the influence of a LLWM dominates as a source of uncertainty in the bulk method, and is not accounted for by applying the tested stability corrections. Furthermore, the stability parameter from the C_{MO} bulk method, $\frac{zu}{L}$, was observed to underestimate stability (when compared with the observed stability parameter, $\frac{z}{L_{ec}}$) at all locations other than CG16-2. As previously mentioned, this stability scheme was developed over flat terrain, and appears to fail on the sloped surfaces of the test sites. CG16-2, with a substantially lower slope angle than the other locations and little katabatic activity, would have presented conditions most similar to those the scheme was developed for, resulting in the best agreement for the tested sites between the modelled and observed stability parameter. The evaluation of bulk performance presented in this study was repeated using a restricted dataset from periods when wind direction was within $\pm 5^\circ$ of the mean downslope wind, only. This was done to investigate if the observed variability in bulk performance could be due to changes in wind direction (and the associated changes to effective roughness length). Very similar behaviour to the original analysis was noted for the results using this wind

window, indicating that wind direction was not a primary cause of the variability in bulk performance observed here.

In the vicinity of a LLWM, wind shear and the mechanical production of turbulence will be reduced and approach zero (Denby and Greuell, 2000). An indication of this was observed at each station when u_{*ec} values recorded by the EC sensors were compared with Δu (Figure 4.9). Friction velocity values estimated from mean wind speed and an assumed logarithmic wind speed profile (u_{*bulk}) do not account for this reduction of wind shear in a LLWM regime, and will be overestimated as a result (Figure 4.10A). Implementing the observed u_{*ec} values into the bulk method resulted in underestimation of the turbulent heat fluxes, however. The u_{*ec} values represent an accurate determination of friction velocity at the height of the EC sensor. During the occurrence of a LLWM near measurement height, the friction velocity as measured by the EC sensor will approach zero at this level (Figure 4.9). This will necessitate a strong gradient in friction velocity between measurement height and the surface. The bulk method, however, assumes a constant value for friction velocity and turbulent flux for this layer. Implementing a u_{*ec} value close to zero into the bulk method will likely underrepresent the wind shear and mechanical turbulence generation occurring in the surface layer below the LLWM during these conditions. More fundamentally, the employed bulk methods were derived through integrating the expressions of the gradient transport closure theory (as introduced in Section 1.6.1), while treating friction velocity as a constant. It has been shown that friction velocity cannot be considered constant below a LLWM, and an alternative derivation of the bulk method is required for katabatic environments, where friction velocity is not assumed constant in the integration but treated as a function of height. Simply replacing u_{*bulk} with observed or corrected friction velocity values for a single height will not address this error in the existing bulk expressions.

The Δu_{log} metric proposed in this study was shown to be a useful, transferable indicator for katabatic, LLWM regimes, with positive Δu_{log} values corresponding with reduced wind shear, suppressed temperature lapse rates, and strongly-stable atmospheric conditions (as indicated by EC-derived $\frac{z}{L_{ec}}$). For negative Δu_{log} , when the wind maximum is assumed to be elevated, underestimation in u_* was observed, along with weakly stable or near-neutral local stability conditions. Underestimation of u_* has been noted in other glacier studies (e.g. Radić *et al.*, 2017), potentially demonstrating an enhanced wind shear region below the LLWM (Banta *et al.*, 2003) that cannot be captured by the bulk method. The vertical gradient in wind speed directly below a LLWM will likely be steeper than that of a logarithmic wind profile, resulting in greater wind shear. Scatter in the Δu_* values may represent variation in the surface roughness encountered by airflow moving towards the station, resulting in variation in wind shear. Seasonal mean values of the EC-derived momentum roughness lengths for each location were implemented in the u_{*bulk} calculations (Equations 4.2–4.3). However, extensive variability was noted in the filtered 30 minute z_{0v_ec} values (Section 3.4.1). Displaying a consistent, linear relationship with Δu_* across the sloped test sites, the Δu_{log} metric was shown to perform well in correcting friction velocity estimates, relative to EC-observed values. Implementing these corrected u_{*adj} values into the C_{log} method resulted in accurate flux parameterisation. As has been previously discussed, however, application of the u_{*adj} values in existing bulk methods would not be valid during shallow, katabatic conditions.

For katabatic flows, the height of the wind maximum has been observed in previous studies to vary linearly with the strength of the wind speed (e.g. Ohata and Higuchi, 1979). This would seem to suggest that the occurrence of LLWM near a typical AWS measurement height (e.g. 2 m)

would be paired with low wind speeds and, therefore, small turbulent fluxes, reducing the impact of wind shear error on the mean fluxes, and making the u_* correction less important. As the slope angle of a surface increases, however, the faster a wind maximum can be at low levels and the more frequent its occurrence (Denby and Greuell, 2000). In this study, a LLWM near measurement height was observed to occur frequently, and in the case of the steepest slope (NG14), to be the dominant regime and to occur at relatively fast wind speeds. Therefore, the wind shear error will influence a substantial portion of the bulk flux estimates over steeper slopes, and needs to be accounted for. The methods used to determine the wind profile in this chapter were based on the available wind data at two levels, and further analysis would benefit from specifically designed observations with wind measurements at several levels. The regular proximity of a LLWM to measurement height during the observations in this study also creates a question that could be explored in future work. EC observations from each station were obtained at a single measurement height (~2 m). For periods when a LLWM was located close to or potentially below the EC sensors, a second, lower-placed EC system would have been useful to evaluate how representative the upper measurements were of the surface fluxes during these conditions. Smeets *et al.* (2000) noted in their study on Pasterze Glacier, Austria, that as a LLWM is approached from below, the magnitude of the sensible heat flux reduced relative to a surface flux value. This was estimated using the bulk method, however, rather than direct EC observations. In our study, obtaining closure of the SEB through ablation modelling (Sections 4.3.3) was pursued, in part, to give confidence to the assumption that the observed fluxes were representative of the fluxes exchanged at the surface. However, for specific periods during LLWM conditions, implementing the additional step proposed above would improve confidence and understanding of surface turbulent flux in this regime.

4.6 Conclusions

A multi-year observation campaign was carried out on two glaciers in the Purcell Mountains of British Columbia, Canada. Continuous observations of the complete SEB, including the turbulent fluxes of sensible and latent heat, were obtained through a total of five station deployments at a series of locations on the glaciers. The turbulent fluxes, Q_H in particular, were observed to be important components of the SEB at each site, with a mean contribution to melt energy of 31% over the five stations. Substantial variation was observed in the daily magnitude of the turbulent fluxes over a season (providing up to 78% of melt energy on individual days), and in seasonal mean values between the ablation and accumulation zones.

When compared with EC-observed values, similar performance was achieved in the parameterisation of the turbulent heat fluxes with or without the use of a stability correction. The performances of the tested bulk aerodynamic methods were found to be sensitive to the development of katabatic conditions over the sloped surfaces of the test sites, and the height of the associated LLWM. The employed stability parameter, estimated from the Monin-Obukhov length, was ineffective in accounting for the variability in turbulent flux arising from these conditions. Friction velocity values were observed to reduce in the vicinity of a LLWM, a process not captured by the estimation of friction velocity from wind speed in the bulk method. With the steepest slope angle, the station on Nordic Glacier showed the most frequent occurrence of a LLWM near measurement height, and hence, a greater tendency for u_* and the bulk fluxes to be overestimated. Where the bulk method was implemented with observed friction velocity values from measurement height, the turbulent fluxes were underestimated, however. The shallow, katabatic surface layer below a LLWM cannot be considered a constant flux layer, due to the variable gradients in wind shear, and therefore, application of a bulk method which assumes a constant u_*

through this layer will be invalid in such conditions. A metric based on the departure of the wind profile from logarithmic, Δu_{log} , was found to be useful as an indicator for shallow, katabatic conditions, and for adjusting friction velocity estimates in non-katabatic conditions.

In summary, the observed importance of the turbulent heat fluxes to SEB, and the variation in their magnitude between different locations and over different timescales, underlines the need for their accurate estimation in glacier SEB and ablation applications. In katabatic environments with frequent development of a LLWM, commonly-applied stability parameters and functions have been shown to be unreliable in this study. In such conditions, precedence should be given to accounting for the associated variability in the wind shear profile when parameterising turbulence.

Chapter 5:

Conclusions and outlook

5.1 Summary of Findings

In the introduction to this thesis, a series of questions was posed regarding glacier surface energy balance, the role of turbulent heat flux, and the accuracy of its estimation. In the intervening chapters, these questions have been addressed, and a summary of the findings is presented below, grouped into the four main categories originally outlined.

5.1.1 SEB Observation and Ablation Modelling

A method to observe the complete surface energy balance of a mountain glacier has been employed at multiple locations in this study, involving direct observations of all relevant energy fluxes. Using a SEB model driven by these values, ablation estimates were produced that showed excellent agreement with observed ablation rates over seasonal, daily and sub-daily timescales at each location. The strength of this performance indicates that closure of the surface energy balance was achieved, and gives confidence in the observation methods, and in the techniques used to process the data and its uncertainties.

The radiation fluxes were observed to provide the largest contribution to melt energy (65–70%) for each site and season, followed by the turbulent fluxes. The rain heat flux, often assumed negligible for SEB studies on glaciers, was observed to be a substantial energy source at daily and

sub-daily timescales during heavy rainfall (up to 20% of daily melt energy), and should be considered for glaciers in regions that experience frequent extreme rain events, or those projected to do so in a warmer climate. The influence of the ground heat flux on SEB was found to be the smallest of all fluxes at the test sites, and can likely be considered negligible for similar temperate ice glaciers.

5.1.2 Importance of Turbulent Heat Flux and its Parameterisation for Glacier Surfaces

The turbulent heat fluxes, and in particular, the sensible heat flux, were observed to be important components of the SEB at each location, providing 31% of melt energy on average, and up to 78% of melt energy on individual days. Substantial differences were observed in the turbulent flux values between different regions of a glacier. In addition, there was extensive variability in the strength of the fluxes on daily and sub-daily timescales at each location, with an order of magnitude range in daily mean values at some sites. Considering the observed importance of the turbulent heat fluxes to surface ablation, it is vital that the magnitude and variation of the fluxes be accurately estimated in SEB applications.

Over the course of this study, a range of commonly used bulk parameterisation methods were evaluated in their estimation of the turbulent heat fluxes on glacier surfaces. Through comparisons with eddy covariance observations, these parameterisation methods were found to be sensitive to the choice of roughness length scheme and stability function used in their calculations. Varying these choices was found to have a large impact on the overall performance of the SEB ablation model into which the fluxes were implemented (up to $\pm 40\%$ of daily ablation).

5.1.3 Roughness Length Variability and Estimation

Measurements of the momentum and scalar roughness lengths for glacier surfaces were obtained at multiple locations in this study over three years. In general, z_{0v} values were found to vary substantially between glaciers, and across the surface of a glacier, casting doubt on the transferability and validity of assumed roughness values taken from different locations and studies, and on the application of a single roughness value over an entire glacier. Temporally, seasonal mean z_{0v} values for ice surfaces were noted to remain relatively consistent at a given location from one season to the next, suggesting that, where z_{0v} values have been obtained, they may be valid to implement over multiple melt seasons. Over snow, momentum roughness length was noted to change through a season as the surface melted, indicating the need for greater temporal resolution in roughness estimation on snow. z_{0v} was also noted to vary with wind direction due to the anisotropic nature of features on a melting glacier surface. The influence of this variation on the effective roughness length is limited, however, due to the persistence in wind direction often experienced on sloped glacier surfaces. Eddy covariance observations of the scalar roughness lengths differed substantially from the corresponding momentum values, showing considerable variation between location and season, and little agreement with fixed ratios commonly assumed with z_{0v} . Where z_{0v} values had been determined for a surface, the Andreas (1987) surface renewal model was shown to return relatively good performance in estimating the scalar roughness lengths.

Varying between observed and assumed roughness length values in the bulk method was found in this study to result in large differences in the magnitude of the generated fluxes (>50%), highlighting the need for the determination of site-specific values. To facilitate this for surfaces without *in situ* observations, two techniques were developed in this study for the remote estimation of z_{0v} from digital elevation models. Both methods returned good performance, identifying

changes between ice and snow cover, and returning z_{0v} values that broadly agreed with *in situ* observations (within \ll one order of magnitude). Over ice, the scale of the surface features having the primary influence on z_{0v} appears to be resolvable using a 1 x 1 m grid cell, and persistent enough for a DEM-based roughness estimate to be usable over an extended period of time. With smaller scale surface features, and more temporally variable roughness, the usefulness of these remote methods over melting snow surfaces may be more limited. In addition, the proposed remote methods were shown to be sensitive to DEM resolution, and would benefit from evaluation over a broader range of resolutions.

5.1.4 The Role of Stability and Slope

Despite substantial uncertainty in their validity over sloped surfaces and in katabatic conditions, there has been widespread use in glacier SEB studies of common stability corrections for the parameterisation of turbulent heat flux; corrections originally developed for use over flat terrain. The uncertainty in their validity has been compounded by a lack of observed turbulent flux data over glaciers with which to assess their performance. In this study, season-long eddy covariance observations were obtained over multiple locations and slope angles, and used to determine the effectiveness of the most commonly used stability parameters and functions, and the sensitivity of parameterisation performance to their selection. In general, similar levels of performance were obtained by either excluding a stability correction and assuming neutral atmospheric stability throughout (C_{log} method), or by applying a stability function based on the Monin-Obukhov length (C_{MO} method), while use of a correction based on the bulk Richardson number (C_{bR} method) led to substantial underestimation of the fluxes. For both the C_{log} and C_{MO} methods, differences in performance were noted between sites with different slope angles. In addition, matching variations

in performance over time were observed for both methods, which could not be accounted for by the estimated stability parameters.

The development of a low-level wind maximum near measurement height during katabatic conditions, as estimated from vertically offset wind speed observations, was found to correspond with observed variability in performance of turbulent flux parameterisation. Deviation of the wind shear profile in these conditions from that assumed in bulk parameterisations was found to be a primary cause of flux under- or overestimation. The assumption of constant friction velocity between the surface and standard measurement height does not hold for shallow, katabatic surface layers, invalidating the use of existing bulk methods that have been derived following this assumption. It is, therefore, suggested that variability in the near-surface friction velocity profile is a primary source of uncertainty in turbulence parameterisation, and that adjusting for this variability should take precedence over the application of existing stability functions which have been shown in this study to be unreliable in sloped, katabatic environments.

5.2 Key Contributions and Future Directions

The success of the extensive field campaign undertaken as part of this study has resulted in a comprehensive surface energy balance and meteorology dataset, encompassing observations from multiple melt seasons and glacial locations. A particularly useful and unique component of this dataset are the high temporal resolution, season-long observations of turbulence and turbulent heat flux from both open and closed path eddy covariance systems. The thorough approach taken to ensure the reliable, continuous, and accurate performance of the sensors in the field, along with the quality control, error analysis and processing performed on the retrieved data, allow for a high level of confidence to be placed on the observations. Obtaining the SEB dataset involved a

combination of common and rare techniques for observations on glacier surfaces, merged with a range of data processing methods. The description of these methods, as presented in this thesis, may help provide a framework for future SEB studies and observation campaigns to implement, and build upon.

Within the current study, this dataset has allowed for the evaluation of commonly used assumptions and parameterisations, which up to this point, had suffered from a lack of observed data on glacier surfaces. Current and future glacier research, along with melt and runoff applications, will benefit from having a more quantified evaluation of the performance and uncertainty of existing methods, helping to inform their choice of approach, and the confidence in their results.

Building on the evaluation of existing techniques for turbulent flux parameterisation, a number of new or updated methods have been presented in this study. As a key input into turbulent flux parameterisation, the remote methods developed in this study to estimate momentum roughness length may greatly facilitate future modelling of SEB over glaciers without site-specific roughness values. Further testing of these methods on a wider range of glacier surfaces, with simultaneous *in situ* measurements, would help confirm the robustness of this approach, and the minimum DEM resolution needed to reliably estimate roughness. Doing so would allow for the potential upscaling of these methods with high resolution satellite imagery, greatly expanding the number of glaciers for which roughness length estimates could be constrained. The effects of a low-level wind maximum on the wind shear profile is recognised in this study as being another key source of uncertainty in flux parameterisation on sloped glacier surfaces. A parameter, Δu_{log} , based on the departure of the wind profile from logarithmic and determinable from mean wind speed measurements at two levels, was found to be a useful indicator of shallow, katabatic winds,

and one that could be implemented where eddy covariance measurements are unavailable. A function based on Δu_{log} for adjusting bulk estimates of friction velocity in non-katabatic conditions was shown to be successful and transferable over the sloped test sites. Building on these methods, the development of an alternative bulk parameterisation for turbulent flux in katabatic conditions is a potential future direction of this work. The derivation of such a bulk method must allow for a variable friction velocity profile in katabatic surface layers. Its development and evaluation would benefit from further observations involving wind and turbulent flux measurements obtained at multiple heights through the boundary layer above a glacier surface.

In addition to the analysis presented in this thesis, the obtained dataset is currently being used in ongoing research on climate model downscaling and regional glacier mass balance (Tessema *et al.*, 2018), and will be a valuable resource to future planned studies on glacier surface energy balance and meteorology.

References

Anderson, B., Mackintosh, A., Stumm, D., and Fitzsimons, S.J. (2010). Climate sensitivity of a high-precipitation glacier in New Zealand. *J. Glaciol.* 56, 114–128. doi:

10.3189/002214310791190929

Andreas, E.L. (2002). Parameterizing Scalar Transfer over Snow and Ice: A Review. *J. Hydrometeorol.* 3, 417–432. doi: 10.1175/1525-7541(2002)003<0417:PSTOSA>2.0.CO;2

Andreas, E.L. (1987). A Theory for the Scalar Roughness and the Scalar Transfer Coefficients over Snow and Sea Ice. *Boundary-Layer Meteorol.* 38, 159–184. doi: 10.1007/BF00121562

Andreas, E.L., Persson, P.O.G., Jordan, R.E., Horst, T.W., Guest, P.S., Grachev, A.A., and Fairall, C.W. (2010). Parameterizing Turbulent Exchange over Sea Ice in Winter. *J. Hydrometeorol.* 11, 87–104. doi: 10.1175/2009JHM1102.1

Andreassen, L.M., Van Den Broeke, M.R., Giesen, R.H., and Oerlemans, J. (2008). A 5 year record of surface energy and mass balance from the ablation zone of Storbreen, Norway. *J. Glaciol.* 54, 245–258. doi: 10.3189/002214308784886199

Arnold, N.S., and Rees, G. (2003). Self-similarity in glacier surface characteristics. *J. Glaciol.* 49, 547–554. doi: 10.3189/172756503781830368

Arnold, N.S., Rees, W.G., Hodson, A.J., and Kohler, J. (2006). Topographic controls on the surface energy balance of a high Arctic valley glacier. *J. Geophys. Res.* 111, F02011.

doi:10.1029/2005JF000426

Aubinet, M. (2008). Eddy covariance CO₂ flux measurements in nocturnal conditions: an analysis of the problem. *Ecological Applications* 18, 1368–1378. doi: 10.1890/06-1336.1

Aubinet, M., Vesala, T., and Papale, D. (2012). *Eddy Covariance: A Practical Guide to Measurement and Data Analysis*. Dordrecht: Springer. p.442.

Banta, R.M., Pichugina, Y.L., and Newsom, R.K. (2003). Relationship between Low-Level Jet Properties and Turbulence Kinetic Energy in the Nocturnal Stable Boundary Layer. *J. Atmos. Sci.* 60, 2549–2555. doi: 10.1175/1520-0469(2003)060%3C2549:RBLJPA%3E2.0.CO;2

Barnett, T.P., Adam, J.C., and Lettenmaier, D.P. (2005). Potential impacts of a warming climate on water availability in snow-dominated regions. *Nature* 438, 303–309. doi:10.1038/nature04141

Beljaars, A.C.M., Holtlag, A.A.M (1991). Flux Parameterization over Land Surfaces for Atmospheric Models. *J. Applied Meteorol.*, 30, 327–341. doi: 10.1175/1520-0450(1991)030<0327:FPOLSF>2.0.CO;2

Benn, D.I., and Evans, D.J.A. (2010). *Glaciers & Glaciation*. UK: Hodder Education. doi: 10.1111/j.1502-3885.2011.00212.x

Berkowicz, R., and Prahm, L.P. (1982). Evaluation of the profile method for estimation of surface fluxes of momentum and heat. *Atmos. Environ.*, 16, 2809–2819. doi: 10.1016/0004-6981(82)90032-4

Bintanja, R., and Van den Broeke, M.R. (1995). The surface energy balance of Antarctic snow and blue ice. *J. Applied Meteorol.*, 34, 902–926. doi: 10.1175/1520-0450(1995)034<0902:TSEBOA>2.0.CO;2

Braithwaite, R. (1995). Aerodynamic stability and turbulent sensible-heat flux over a melting ice surface, the Greenland ice sheet. *J. Glaciol.* 41, 562–571. doi: 10.3189/S0022143000034882

Braun, M., and Hock, R. (2004). Spatially distributed surface energy balance and ablation modelling on the ice cap of King George Island (Antarctica). *Global and Planetary Change* 42, 45–58. doi: 10.1016/j.gloplacha.2003.11.010

Brock, B.W., Mihalcea, C., Kirkbride, M.P., Diolaiuti, G., Cutler, M.E.J., and Smiraglia, C. (2010). Meteorology and surface energy balance fluxes in the 2005–2007 ablation seasons at the Miage debris-covered glacier, Mont Blanc Massif, Italian Alps. *J. Geophys. Res.* 115, D09106. doi:10.1029/2009JD013224

Brock, B.W., Willis, I.C., and Sharp, M.J. (2006). Measurement and parameterization of aerodynamic roughness length variations at Haut Glacier d’Arolla, Switzerland. *J. Glaciol.* 52, 281–297. doi: 10.3189/172756506781828746

Brock, B., Willis, I., Sharp, M., and Arnold, N. (2000). Modelling seasonal and spatial variations in the surface energy balance of Haut Glacier d'Arolla, Switzerland. *Annals Glaciol.* 31, 53–62.

doi: 10.3189/172756400781820183

Burba, G. (2013). *Eddy Covariance Method for Scientific, Industrial, Agricultural, and Regulatory Applications*. Nebraska: LI-COR Biosciences.

Calanca, P. (2001). A note on the roughness length for temperature over melting snow and ice.

Q. J. R. Meteorol. Soc. 127, 255–260. doi: 10.1002/qj.49712757114

Campbell Scientific Inc. (2014). *SR50A Sonic Ranging Sensor Instruction Manual*. Edmonton:

Campbell Scientific (Canada) Corp. p.8

Campbell Scientific Inc. (2013). *IRGASON Integrated CO₂/H₂O Open-Path Gas Analyzer and 3D*

Sonic Anemometer Manual. Edmonton: Campbell Scientific (Canada) Corp. p.28

Carenzo, M., Pellicciotti, F., Rimkus, S., and Burlando, P. (2009). Assessing the transferability and robustness of an enhanced temperature-index glacier-melt model. *J. Glaciol.* 55, 258–274.

doi: 10.3189/002214309788608804

Clarke, G.K.C., Jarosch, A.H., Anslow, F.S., Radić, V., and Menounos, B. (2015). Projected deglaciation of western Canada in the twenty-first century, *Nat. Geosci.* 8, 372–377.

doi:10.1038/ngeo2407

Columbia Basin Trust (2017). The Basin. Available online at http://www.cbt.org/The_Basin/.

Conway, J.P., and Cullen, N.J. (2013). Constraining turbulent heat flux parameterization over a temperate maritime glacier in New Zealand. *Annal. Glaciol.* 54, 41–51. doi: 10.3189/2013AoG63A604

Cuffey, K.M., and Paterson, W.S.B. (2010). *The Physics of Glaciers. Fourth Edition.* Amsterdam etc.: Elsevier. p.158. ISBN: 978-0-12-369461-4

Cullen, N., and Conway, J. (2015). A 22 month record of surface meteorology and energy balance from the ablation zone of Brewster Glacier, New Zealand. *J. Glaciol.* 61, 931–946. doi: 10.3189/2015JoG15J004

Cullen, N.J., Mölg, T., Kaser, G., Steffen, K., and Hardy, D.R. (2007). Energy-balance model validation on the top of Kilimanjaro, Tanzania, using eddy covariance data. *Annal. Glaciol.* 46, 227–233. doi: 10.3189/172756407782871224

Dadic R., Mott, R., Lehning, M., Carenzo, M., Anderson, B., and Mackintosh, A. (2013). Sensitivity of turbulent fluxes to wind speed over snow surfaces in different climatic settings. *Adv. Water Res.* 55, 178–189. doi: 10.1016/j.advwatres.2012.06.010

De La Casinière, A. (1974). Heat Exchange over a Melting Snow Surface. *J. Glaciol.*, 13, 55–72. doi:10.3189/S0022143000023376

Denby, B. (1999). Second-Order Modelling of Turbulence in Katabatic Flows. *Boundary-Layer Meteorol.* 92, 67–100. doi: 10.1023/A:1001796906927

Denby, B., and Greuell, W. (2000). The use of bulk and profile methods for determining surface heat fluxes in the presence of glacier winds. *J. Glaciol.* 46, 445–452. doi: 10.3189/172756500781833124

Denby, B., and Smeets, C. (2000). Derivation of Turbulent Flux Profiles and Roughness Lengths from Katabatic Flow Dynamics. *J. Appl. Meteor.* 39, 1601–1612. doi: 10.1175/1520-0450(2000)039<1601:DOTFPA>2.0.CO;2

Devine, K.A., and Mekis, E. (2008). Field accuracy of Canadian rain measurements. *Atmosphere-Ocean* 46, 213-227. doi: 10.3137/ao.460202

Duchon, C., and Biddle, C.J. (2010). Undercatch of tipping-bucket gauges in high rain rate events. *Adv. Geosci.* 25, 11–15. doi: 10.5194/adgeo-25-11-2010

Dyer, A.J. (1974). A review of flux-profile relationships. *Boundary-Layer Meteorol.* 7, 363–372. doi: 10.1007/BF00240838

Engelhardt, M., Schuler, T., and Andreassen, L. (2013). Glacier mass balance of Norway 1961-2010 calculated by a temperature-index model. *Annals of Glaciol.* 54, 32–40. doi: 10.3189/2013AoG63A245

Farrell, A.P., Hinch, S.G., Cooke, S. J., Patterson, D. A., Crossin, G. T., Lapointe, M., and Mathes, M.T. (2008). Pacific Salmon in Hot Water: Applying Aerobic Scope Models and Biotelemetry to Predict the Success of Spawning Migrations. *Physiol. Biochem. Zoology* 81, 697–709. doi: 10.1086/592057

Fassnacht, S.R., Williams, M.W., and Corrao, M.V. (2009). Changes in the surface roughness of snow from millimetre to metre scales. *Ecological Complexity* 6, 221–229. doi: 10.1016/j.ecocom.2009.05.003

Fausto, R.S., van As, D., Box, J.E., Colgan, W., Langen, P.L., and Mottram, R.H. (2016). The implication of nonradiative energy fluxes dominating Greenland ice sheet exceptional ablation area surface melt in 2012. *Geophys. Res. Lett.* 43, 2649–2658. doi: 10.1002/2016GL067720

Finkelstein, P.L., and Sims, P.F. (2001). Sampling error in eddy correlation flux measurements. *J. Geophys. Res.* 106, 3503–3509. doi: 10.1029/2000JD900731

Fitzpatrick, N. (2007). Uncertainty in Stevenson Screen Temperature Measurements [master's thesis]. [Reading]: University of Reading. p.73

Fitzpatrick, N., Radić, V., and Menounos, B. (2017). Surface energy balance closure and turbulent flux parameterization on a mid-latitude mountain glacier, Purcell Mountains, Canada. *Front. Earth Sci.* 5:67. doi: 10.3389/feart.2017.00067

Foken, T. (2008). *Micro-meteorology*. Berlin: Springer. p.118–119

Garnier, B.J. and Ohmura, A. (1968). A Method of Calculating the Direct Shortwave Radiation Income of Slopes. *J. Appl. Meteor.* 7, 796–800. doi: 10.1175/1520-0450(1968)007<0796:AMOCTD>2.0.CO;2

Giesen, R.H., Andreassen, L.M., Oerlemans, J., and Van Den Broeke, M.R. (2014). Surface energy balance in the ablation zone of Langfjordjøkelen, an arctic, maritime glacier in northern Norway, *J. Glaciol.* 60, 57–70. doi: 10.3189/2014JoG13J063

Gillett, S., and Cullen, N.J. (2011). Atmospheric controls on summer ablation over Brewster Glacier, New Zealand. *International J. Climatol.* 31, 2033–2048. doi: 10.1002/joc.2216

Greuell, W., and Böhm, R. (1998). 2 m temperatures along melting mid-latitude glaciers, and implications for the sensitivity of the mass balance to variations in temperature. *J. Glaciol.* 44, 9–20. doi: 10.3189/S0022143000002306

Greuell, W., and Smeets, P. (2001). Variations with elevation in the surface energy balance on the Pasterze (Austria). *J. Geophys. Res.* 106, 31717–31727. doi: 10.1029/2001JD900127

Grisogono, B., and Oerlemans, J. (2001). Katabatic Flow: Analytic Solution for Gradually Varying Eddy Diffusivities. *J. Atmos. Sci.* 58, 3349–3354. doi: 10.1175/1520-0469(2001)058<3349:KFASFG>2.0.CO;2

Harrison, R.G. (2010). Natural ventilation effects on temperatures within Stevenson screens. *Q. J. R. Meteorol. Soc.* 136, 253–259. doi: :10.1002/qj.537

Hay, J.E., and Fitzharris, B.B. (1988). A comparison of energy balance and bulk aerodynamic approaches for estimating glacier melt. *J. Glaciol.* 34, 145–153. doi: 10.1017/S0022143000032172

Hock, R. (2005). Glacier melt: a review of processes and their modelling. *Progress in Physical Geography* 29, 362–391. doi: 10.1191/0309133305pp453ra

Hock, R., and Holmgren, B. (2005). A distributed surface energy-balance model for complex topography and its application to Storglaciären, Sweden. *J. Glaciol.* 51, 25–36. doi: 10.3189/172756505781829566

Hock, R., and Holmgren, B. (1996). Some aspects of energy balance and ablation of Storglaciären, northern Sweden. *Geogr. Ann.* 78, 121–131. doi: 10.2307/520974

Hock, R., and Schroff, K. (2004). “Difference between ventilated and unventilated temperature measurements over snow surfaces,” in *Automatic Weather Stations on Glaciers – Lessons to be learned Extended abstracts* (Utrecht: Institute for Marine and Atmospheric Research), 56–58.

Hoffman, M.J., Fountain, A.G., and Liston, G.E. (2008). Surface energy balance and melt thresholds over 11 years at Taylor Glacier, Antarctica. *J. Geophys. Res.* 113, F04014. doi:10.1029/2008JF001029.

Holtslag, A.A., and De Bruin, H.A. (1988). Applied Modeling of the Nighttime Surface Energy Balance over Land. *J. Appl. Meteor.* 27, 689–704. doi: 10.1175/1520-0450(1988)027<0689:AMOTNS>2.0.CO;2

Huss, M., Farinotti, D., Bauder, A., and Funk, M. (2008). Modelling runoff from highly glacierized alpine drainage basins in a changing climate. *Hydrol. Process.* 22, 3888–3902. doi: 10.1002/hyp.7055

Huss, M., and Hock, R. (2015). A new model for global glacier change and sea-level rise. *Front. Earth Sci.* 3:54. doi: 10.3389/feart.2015.00054

Ibrom, A., Dellwik, E., Flyvbjerg, H., Jensen, N.O., and Pilegaard, K. (2007). Strong low-pass filtering effects on water vapor flux measurements with closed-path eddy correlation systems. *Agricultural and Forest Meteorology* 147, 140–156. doi: 10.1016/j.agrformet.2007.07.007

IPCC (2013). “Summary for Policymakers,” in *Climate Change 2013: The Physical Science Basis. Contribution of Working Group I to the Fourth Assessment Report of the Intergovernmental Panel on Climate Change*, eds. S. Solomon, D. Qin, M. Manning, Z. Chen,

M. Marquis, K.B. Averyt, M.Tignor and H.L. Miller (Cambridge, and New York, NY: Cambridge University Press), 1–18.

Isenburg, M., Liu, Y., Shewchuk, J., Snoeyink, J., and Thirion, T. (2006). Generating Raster DEM from Mass Points via TIN Streaming. *GIScience'06 Conference Proceedings*, 186–198.

Jonsell, U., Hock, R., and Holmgren, B. (2003). Spatial and temporal variations in albedo on Storglaciären, Sweden. *J. Glaciol.* 49, 59–68. doi: 10.3189/172756503781830980

Jost, G., Moore, R.D., Menounos, B., and Wheate, R. (2012). Quantifying the contribution of glacier runoff to streamflow in the upper Columbia River Basin, Canada. *Hydrol. Earth Syst. Sci.* 16, 849–860. doi:10.5194/hess-16-849-2012

Kaimal, J.C., and Gaynor, J.E. (1991). Another look at sonic thermometry. *Boundary-Layer Meteorol.* 56, 401–410. doi:10.1007/BF00119215

Kipp & Zonen (2009). *CNR 4 Net Radiometer Instruction Manual*. Delft: Kipp & Zonen.

Kljun, N., Calanca, P., Rotach, M.W., and Schmid, H.P. (2015). A simple two-dimensional parameterization for Flux Footprint Prediction (FFP). *Geosci. Model Dev.* 8, 3695–3713. doi: 10.5194/gmd-8-3695-2015

Kljun, N., Rotach, M.W., and Schmid, H. P. (2002). A 3D Backward Lagrangian Footprint Model for a Wide Range of Boundary Layer Stratifications. *Boundary-Layer Meteorol.* 103, 205–226. doi: 10.1023/A:1014556300021

Kondo, J. and Yamazawa, H. (1986). Aerodynamic roughness over an inhomogeneous ground surface. *Boundary-Layer Meteorol.* 35, 331–348. doi: 10.1007/BF00118563

Konzelmann, T., and Braithwaite, R.J. (1995). Variations of ablation, albedo and energy balance at the margin of the Greenland ice sheet, Kronprins Christian Land, eastern north Greenland. *J. Glaciol.* 41, 174–182.

Lee, X., Massman, W., and Law, B. (2004). *Handbook of Micrometeorology: A Guide for Surface Flux Measurement and Analysis*. Dordrecht: Kluwer Academic Publishers. p.252.

Lettau, H. (1969). Note on Aerodynamic Roughness-Parameter Estimation on the Basis of Roughness-Element Description. *J. Appl. Meteorol.* 8, 828–832. doi: 10.1175/1520-0450(1969)008<0828:NOARPE>2.0.CO;2

Lewis, K.J., Fountain, A.G., and Dana, G.L. (1998). Surface energy balance and meltwater production for a Dry Valley glacier, Taylor Valley, Antarctica. *Annals of Glaciol.* 27, 603–609. doi: 10.3189/1998AoG27-1-603-609

LI-COR, Inc. (2016). EddyPro® Software (Version 6.2) [Computer software]. Lincoln, NE. Infrastructure for Measurements of the European Carbon Cycle consortium.

Li, A., Zhao, W., Mitchell, J.J., Glenn, N.F., Germino, M.J., Sankey, J.B., and Allen, R.G. (2017). Aerodynamic Roughness Length Estimation with Lidar and Imaging Spectroscopy in a Shrub-Dominated Dryland. *Photogram. Eng. Remote Sens.* 83, 415–427. doi: 10.14358/PERS.83.6.415

Li, Z., Lyu, S., Zhao, L., Wen, L., Ao, Y., and Wang, S. (2016). Turbulent transfer coefficient and roughness length in a high-altitude lake, Tibetan Plateau. *Theor. Appl. Climatol.* 124, 723–735. doi:10.1007/s00704-015-1440-z

Litt, M., Sicart, J.E., Helgason, W.D., and Wagnon, P. (2015). Turbulence Characteristics in the Atmospheric Surface Layer for Different Wind Regimes over the Tropical Zongo Glacier (Bolivia, 16°S). *Boundary-Layer Meteorol.* 154, 471–495. 10.1007/s10546-014-9975-6

Marzeion, B., Jarosch, A.H., and Hofer, M. (2012). Past and future sea-level change from the surface mass balance of glaciers. *The Cryosphere* 6, 1295–1322. doi: 10.5194/tc-6-1295-2012

Mauder, M., and Foken, T. (2004). Documentation and instruction manual of the eddy covariance software package TK2. *Universität Bayreuth, Abt. Mikrometeorologie, Arbeitsergebnisse* 26, 44 pp. (Internet: ISSN 1614-8926)

Mekonnen, G.B., Matula, S., and Doležal, F. (2015). Adjustment to rainfall measurement undercatch with a tipping-bucket rain gauge using ground-level manual gauges. *Meteorol. Atmos. Phys.* 127, 241–256. doi: 10.1007/s00703-014-0355-z

Mölg, T., Cullen, N.J., Hardy, D.R., Kaser, G., and Klok, L. (2008). Mass balance of a slope glacier on Kilimanjaro and its sensitivity to climate. *International J. Climatol.* 28, 881–892. doi: 10.1002/joc.1589

Mölg, T., and Hardy, D.R. (2004). Ablation and associated energy balance of a horizontal glacier surface on Kilimanjaro, *J. Geophys. Res.* 109, D16104. doi:10.1029/2003JD004338.

Moncrieff, J.B., Clement, R., Finnigan, J., and Meyers, T. (2004). “Averaging, detrending and filtering of eddy covariance time series,” in *Handbook of micrometeorology: a guide for surface flux measurements*, eds. X. Lee, W. Massman, and B. Law (Dordrecht: Kluwer Academic), 7–31.

Monin, A.S., and Obukhov, A.M. (1954). Basic laws of turbulent mixing in the surface layer of the atmosphere. *Tr. Akad. Nauk SSSR Geophys. Inst.* 24, 163–187.

Munro, D.S. (1989). Surface Roughness and Bulk Heat Transfer on a Glacier: Comparison with Eddy Correlation. *J. Glaciol.* 35, 343–348. doi: 10.1017/S0022143000009266

Nield, J.M., King, J., Wiggs, G.F.S., Leyland, J., Bryant, R.G., Chiverrell, R.C., *et al.* (2014). Estimating aerodynamic roughness over complex surface terrain. *J. Geophys. Res. Atmos.* 118, 12,948–12,961. doi: 10.1002/2013JD020632

Obleitner, F. (2004). “On the performance of un aspirated, plate-shielded thermometer screens,” in *Automatic Weather Stations on Glaciers – Lessons to be learned Extended abstracts* (Utrecht: Institute for Marine and Atmospheric Research), 76–82.

Oerlemans, J., and Grisogono, B. (2002). Glacier winds and parameterisation of the related surface heat fluxes. *Tellus* 54A, 440–452. doi: 10.1034/j.1600-0870.2002.201398

Ohata, J., and Higuchi, K. (1979). Gravity Wind on a Snow Patch. *J. Meteorol. Soc. Japan* 57, 254–263. doi: 10.2151/jmsj1965.57.3_254

Park, S.J., Park, S.U., and Ho, C.H. (2010). Roughness Length of Water Vapor over Land Surfaces and Its Influence on Latent Heat Flux. *Terr. Atmos. Ocean. Sci.* 21, 855–867. doi: 10.3319/TAO.2009.11.13.01(Hy)

Parmhed, O., Oerlemans, J., and Grisogono, B. (2004). Describing surface fluxes in katabatic flow on Breidamerkurjökull, Iceland. *Q. J. R. Meteorol. Soc.* 130, 1137–1151. doi: 10.1256/qj.03.52

- Paul-Limoges, E., Christen, A., Coops, N.C., Black, T.A., and Trofymow, J.A. (2013). Estimation of aerodynamic roughness of a harvested Douglas-fir forest using airborne LiDAR. *Remote Sens. Environ.* 136, 225–233. doi: 10.1016/j.rse.2013.05.007
- Petersen, L., and Pellicciotti, F. (2011). Spatial and temporal variability of air temperature on a melting glacier: Atmospheric controls, extrapolation methods and their effect on melt modeling, Juncal Norte Glacier, Chile. *J. Geophys. Res.* 116, D23109. doi: 10.1029/2011JD015842
- Petersen, L., Pellicciotti, F., Juszak, I., Carenzo, M., and Brock, B. (2013). Suitability of a constant air temperature lapse rate over an Alpine glacier: testing the Greuell and Böhm model as an alternative. *Annals of Glaciol.* 54, 120–130. doi: 10.3189/2013AoG63A477
- Plüss, C. and Ohmura, A. (1997). Longwave Radiation on Snow-Covered Mountainous Surfaces. *J. Appl. Meteor.* 36, 818–824. doi: 10.1175/1520-0450-36.6.818
- Pope, S.B. (2000). *Turbulent Flows*. Cambridge: Cambridge University Press.
doi:10.1017/CBO9780511840531
- Radić, V., and Hock, R. (2011). Regionally differentiated contribution of mountain glaciers and ice caps to future sea-level rise. *Nat. Geosci.* 4, 91–94. doi: 10.1038/ngeo1052

Radić, V., Menounos, B., Shea, J., Fitzpatrick, N., Tessema, M.A., and Dery, S.J. (2017).

Evaluation of different methods to model near-surface turbulent fluxes for an alpine glacier in the Cariboo Mountains, BC, Canada. *The Cryosphere* 11, 2897–2918. doi: 10.5194/tc-2017-80

Rasul, G. (2014). Food, water, and energy security in South Asia: A nexus perspective from the Hindu Kush Himalayan region. *Environ. Sci. Policy* 39, 35–48. doi:

10.1016/j.envsci.2014.01.010

Shea, J.M., and Moore, R.D. (2010). Prediction of spatially distributed regional-scale fields of air temperature and vapor pressure over mountain glaciers. *J. Geophys. Res.* 115, D23107. doi:

10.1029/2010JD014351

Sicart, J.E., Litt, M., Helgason, W., Tahar, V.B., and Chaperon, T. (2014). A study of the atmospheric surface layer and roughness lengths on the high-altitude tropical Zongo glacier, Bolivia. *J. Geophys. Res. Atmos.* 119, 3793–3808. doi: 10.1002/2013JD020615

Sicart, J.E., Wagon, P., and Ribstein, P. (2005). Atmospheric controls of the heat balance of Zongo Glacier (16°S, Bolivia), *J. Geophys. Res.* 110, D12106. doi: 10.1029/2004JD005732

Smeets, C.J.P.P., Duynkerke, P.G., and Vugts, H.F. (1999). Observed Wind Profiles and Turbulence Fluxes over an ice Surface with Changing Surface Roughness. *Boundary-Layer Meteorol.* 92, 99–121. doi: 10.1023/A:1001899015849

Smeets, C.J.P.P., Duynkerke, P.G., and Vugts, H.F. (1998). Turbulence Characteristics of the Stable Boundary Layer Over a Mid-Latitude Glacier. Part I: A Combination of Katabatic and Large-Scale Forcing. *Boundary-Layer Meteorol.* 87, 117–145. doi:10.1023/A:1000860406093

Smeets, C.J.P.P., Duynkerke, P.G., and Vugts, H.F. (2000). Turbulence Characteristics of the Stable Boundary Layer over a Mid-Latitude Glacier. Part II: Pure Katabatic Forcing Conditions. *Boundary-Layer Meteorol.* 97, 73–107. doi: 10.1023/A:1002738407295

Smeets, C.J.P.P., and van den Broeke, M.R. (2008). The Parameterisation of Scalar Transfer over Rough Ice. *Boundary-Layer Meteorol.* 128, 339–355. doi: 10.1007/s10546-008-9292-z

Smith, M.W. (2014). Roughness in the Earth Sciences. *Earth-Sci. Reviews* 136, 202–225. doi: 10.1016/j.earscirev.2014.05.016

Smith, M.W., Quincey, D.J., Dixon, T., Bingham, R.G., Carrivick, J.L., Irvine-Fynn, T.D.L., and Rippin, D.M. (2016). Aerodynamic roughness of glacial ice surfaces derived from high-resolution topographic data. *J. Geophys. Res. Earth Surf.* 121. doi: 10.1002/2015JF003759

Stahl, K., Moore, R.D., Shea, J.M., Hutchinson, D., and Cannon, A.J. (2008). Coupled modelling of glacier and streamflow response to future climate scenarios. *Water Resour. Res.*, 44, W02422. doi: 10.1029/2007WR005956.

Stull, R.B. (1988). *An Introduction to Boundary Layer Meteorology*. Dordrecht: Kluwer Academic Publishers.

Tessema, M., Radić, V., Menounos, B., and Fitzpatrick, N. (2018). Evaluation of dynamically downscaled near-surface mass and energy fluxes for three mountain glaciers, British Columbia, Canada. Manuscript submitted for publication.

Van As, D. (2011). Warming, glacier melt and surface energy budget from weather station observations in the Melville Bay region of northwest Greenland. *J. Glaciol.* 57, 208–220. doi: 10.3189/002214311796405898

Van den Broeke, M., Reijmer, C., van As, D., van de Wal, R., and Oerlemans, J. (2005). Seasonal cycles of Antarctic surface energy balance from automatic weather stations. *Annals Glaciol.* 41, 131–139. doi: 10.3189/172756405781813168

Van den Broeke, M., van As, D., Reijmer, C., and van de Wal, R. (2004). Assessing and improving the quality of unattended radiation observations in Antarctica. *J. Atmos. Oceanic Tech.* 21, 1417–1431. doi: 10.1175/1520-0426(2004)021<1417:AAITQO>2.0.CO;2

Van den Broeke, M., Reijmer, C., van As, D., van de Wal, R., and Oerlemans, J. (2005). Seasonal cycles of Antarctic surface energy balance from automatic weather stations. *Annals Glaciol.* 41, 131–139. doi: 10.3189/172756405781813168

Van der Avoird, E., and Duynkerke, P.G. (1999). Turbulence in a Katabatic Flow. *Boundary-Layer Meteorol.* 92, 37–63. doi: 10.1023/A:1001744822857

Večenaj, Ž., and De Wekker, S.F.J. (2015). Determination of non-stationarity in the surface layer during the T-REX experiment. *Q. J. R. Meteorol. Soc.* 141, 1560–1571. doi: 10.1002/qj.2458

Webb, E.K. (1970). Profile relationships: The log-linear range, and extension to strong stability. *Q. J. R. Meteorol. Soc.* 96, 67–90. doi: 10.1002/qj.49709640708

Webb, E.K., Pearman, G.I., and Leuning R. (1980). Correction of flux measurements for density effects due to heat and water vapour transfer. *Q. J. R. Meteorol. Soc.* 106, 85–100. doi: 10.1002/qj.49710644707

Wilczak, J.M., Oncley, S.P., and Stage, S.A. (2001). Sonic Anemometer Tilt Correction Algorithms. *Boundary-Layer Meteorol.* 99, 127–150. doi: 10.1023/A:1018966204465

Wieringa, J. (1993). Representative roughness parameters for homogeneous terrain. *Boundary-Layer Meteorol.* 63, 323–363. doi: 10.1007/BF00705357

World Meteorological Organisation (WMO) (1983). *Guide to Meteorological Instruments and Methods of Observation - WMO No.8*. Geneva: World Meteorological Organisation. p.4.3

Appendix A

Table A. 1. Momentum roughness length values (in mm) for each station footprint estimated using the block method (z_{0v_bloc}) from the LiDAR-derived DEMs. The roughness values for the prevailing downslope southerly wind direction, and the cross-glacier easterly and westerly directions are shown here. The uncertainty values from error propagation are also shown.

	NG14		CG15-1		CG15-2		CG16-1		CG16-2	
South	April	Sept	April	Sept	April	Sept	April	Sept	April	Sept
2014	-	6.3±0.9	-	2.5±0.1	-	2.5±0.5	-	1.6±0.4	-	0.5±0.2
2015	2±0.2	5±0.1	0.3±0.2	-	0.5±0.2	-	0.3±0.1	-	0.3±0.1	0.4±0.2
2016	2.5±0.1	4±0.4	0.6±0.3	4±0.4	0.8±0.2	3.2±0.5	0.3±0.1	1.6±0.5	0.4±0.1	0.4±0.1
West										
2014	-	7.9±0.9	-	4±0.1	-	3.2±0.5	-	2±0.4	-	0.8±0.2
2015	1.3±0.2	5±0.1	1±0.2	-	1.3±0.2	-	0.5±0.1	-	1±0.1	1±0.2
2016	2±0.1	5±0.4	1.6±0.3	5±0.4	1.6±0.2	4±0.5	0.5±0.1	2±0.5	1±0.1	0.8±0.1
East										
2014	-	12.6±0.9	-	2±0.1	-	2±0.5	-	2±0.4	-	0.3±0.2
2015	6.3±0.2	10±0.1	0.5±0.2	-	0.3±0.2	-	0.3±0.1	-	0.1±0.1	0.2±0.2
2016	6.3±0.1	10±0.4	0.6±0.3	2.5±0.4	0.4±0.2	2±0.5	0.3±0.1	1.6±0.5	0.2±0.1	0.2±0.1

Table A. 2. Momentum roughness length values (in mm) for each station estimated using the profile method (z_{0v_prof}) from the LiDAR-derived DEMs. The roughness values for the prevailing downslope southerly wind direction, and the cross-glacier easterly and westerly directions are shown here. $\pm\sigma$ of the roughness values for the 101 x 101 m upwind patch is also presented.

	NG14		CG15-1		CG15-2		CG16-1		CG16-2	
South	April	Sept	April	Sept	April	Sept	April	Sept	April	Sept
2014	-	6.9±0.3	-	2.6±0.2	-	2.0±0.3	-	2.1±0.2	-	0.4±0.02
2015	4.6±0.4	4.2±0.4	0.2±0.04	-	0.5±0.02	-	0.9±0.03	-	0.1±0.01	0.2±0.04
2016	3.6±0.2	5.6±0.1	0.6±0.1	5.6±0.5	1.7±0.1	7.1±0.6	0.7±0.03	2.6±0.2	0.1±0.02	0.6±0.04
West										
2014	-	25.2±4.3	-	24.1±5.3	-	5.1±0.3	-	5.8±0.54	-	0.7±0.04
2015	4.5±0.4	23.2±5.5	0.3±0.02	-	0.5±0.04	-	0.6±0.1	-	0.1±0.003	0.2±0.02
2016	4.5±0.6	11.6±4.8	0.6±0.17	8.3±1.2	1.8±0.18	9.9±0.53	0.6±0.03	6.2±0.22	0.2±0.02	0.5±0.03
East										
2014	-	3.7±0.4	-	42.7±8.5	-	4±0.3	-	3.5±0.6	-	0.7±0.03
2015	3.5±0.1	6.5±1.1	0.2±0.01	-	0.3±0.06	-	0.6±0.02	-	0.1±0.01	0.2±0.01
2016	5.6±0.9	4.4±0.4	0.4±0.02	20.5±1.4	0.8±0.03	4.4±0.3	0.8±0.06	10.7±1.2	0.1±0.01	0.5±0.03

Appendix B

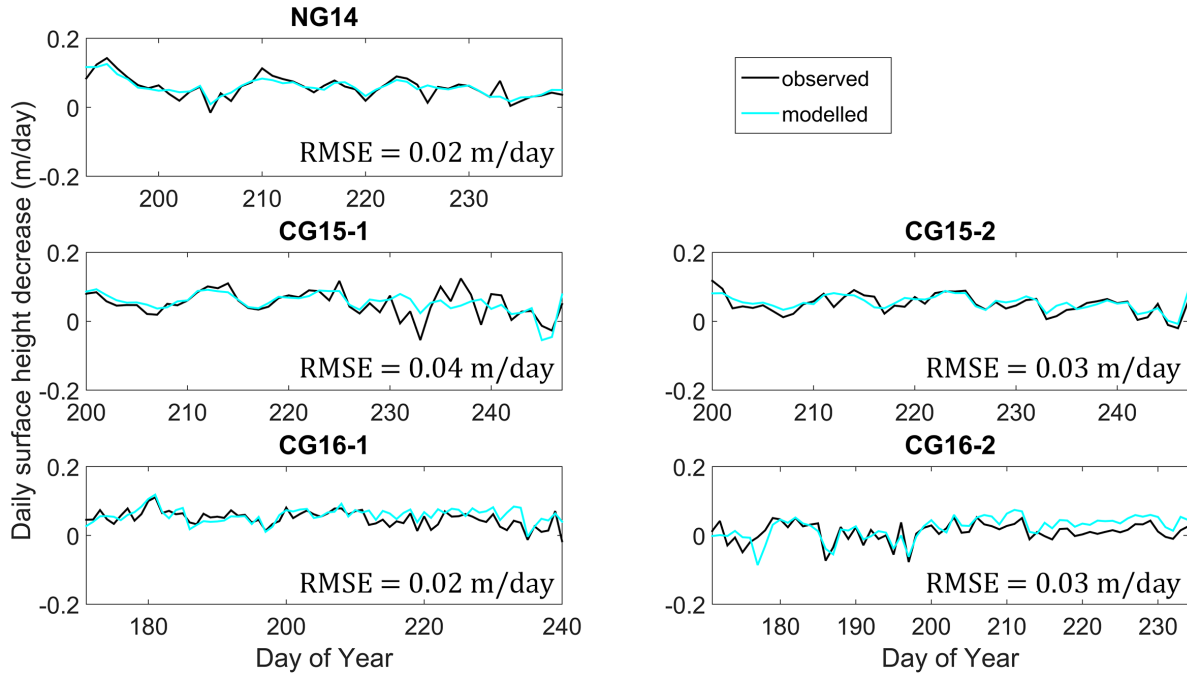


Figure B.1. Observed (black) and SEB-modelled (blue) daily surface height decrease over a melt season for each station deployed in the field campaign.

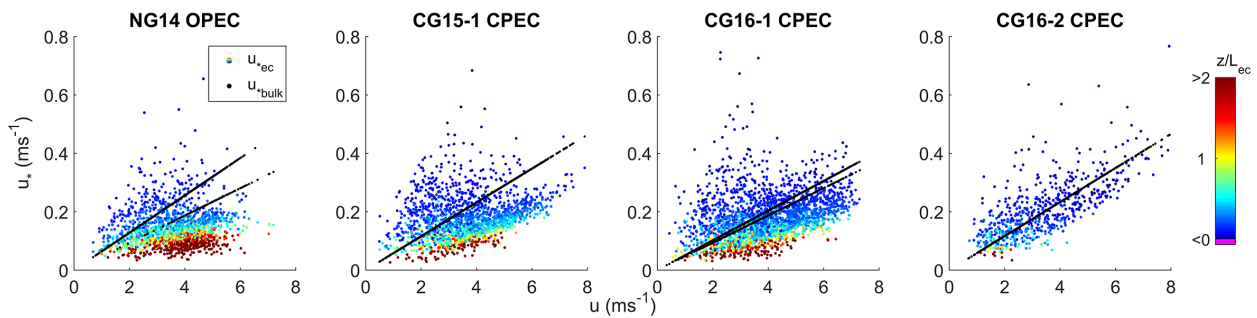


Figure B.2. 30-minute wind speed values plotted against EC-observed (u_{ec}) and C_{log} -modelled (u_{bulk}) friction velocity. The slope of the u_{bulk} values is determined by the implemented momentum roughness length value; where two slopes exist, separate z_{0v} values have been used for ice and snow.